



---

Theses and Dissertations

---

2017-12-01

## Design and Analysis of Compressed Air Power Harvesting Systems

Zachary James Sadler  
*Brigham Young University*

Follow this and additional works at: <https://scholarsarchive.byu.edu/etd>



Part of the [Mechanical Engineering Commons](#)

---

### BYU ScholarsArchive Citation

Sadler, Zachary James, "Design and Analysis of Compressed Air Power Harvesting Systems" (2017).  
*Theses and Dissertations*. 7180.  
<https://scholarsarchive.byu.edu/etd/7180>

This Thesis is brought to you for free and open access by BYU ScholarsArchive. It has been accepted for inclusion in Theses and Dissertations by an authorized administrator of BYU ScholarsArchive. For more information, please contact [scholarsarchive@byu.edu](mailto:scholarsarchive@byu.edu), [ellen\\_amatangelo@byu.edu](mailto:ellen_amatangelo@byu.edu).

# Design and Analysis of Compressed Air Power Harvesting Systems

Zachary James Sadler

A thesis submitted to the faculty of  
Brigham Young University  
in partial fulfillment of the requirements for the degree of  
Master of Science

Matthew R. Jones, Chair  
Brian D. Iverson  
Troy R. Munro

Department of Mechanical Engineering  
Brigham Young University

Copyright © 2017 Zachary James Sadler

All Rights Reserved

## ABSTRACT

### Design and Analysis of Compressed Air Power Harvesting Systems

Zachary James Sadler  
Department of Mechanical Engineering, BYU  
Master of Science

Procedure for site discovery, system design, and optimization of power harvesting systems is developed with an emphasis on application to air compressors. Limitations for the usage of infrared pyrometers is evaluated. A system of governing equations for thermoelectric generators is developed. A solution method for solving the system of equations is created in order to predict power output from the device. Payback analysis is proposed for determining economic viability. A genetic algorithm is used to optimize the power harvesting system payback with changing quantities and varieties of thermoelectric generators, as well as the back work put into cooling the thermoelectric generators.

Experimental data is taken for laboratory simulation of a power harvesting system under varying resistive load and thermal conductances in order to confirm the working model. A power harvester is designed for and installed on a consumer grade portable air compressor. Experimental data is compared against the model's prediction. As a case study, a system is designed for a water-cooled power harvesting system.

Thermoelectric generator power harvesters are found to be economically infeasible for typical installations at current energy prices. Changes in parameters which would increase economic feasibility of the power harvesting system are discussed.

Keywords: heat transfer, power harvesting, thermoelectric generators, optimization, genetic algorithm

## ACKNOWLEDGMENTS

I started working with Dr. Matthew Jones after taking his undergraduate thermodynamics course when he invited me to work on a project in his lab. I had a lot to learn as a Junior undergraduate student, and I appreciate the mentoring he has given me since then in helping to hone my problem solving skills. I also appreciate the confidence he has constantly placed in me and my ability to fulfill my research objectives. This project is the culmination of our work since that time. I am grateful for the opportunity I have had to expand my horizons and explore this complicated, open-ended problem.

Even more so, I am grateful for the love and support of my wife, Rose. Her patience in listening to me talk about problems and struggles with research as well as her encouragement assisted me more than she will ever realize. It is her positive encouragement and understanding in the face of difficulties that made this project possible.



## TABLE OF CONTENTS

<b>LIST OF TABLES</b> . . . . .	<b>vii</b>
<b>LIST OF FIGURES</b> . . . . .	<b>viii</b>
<b>NOMENCLATURE</b> . . . . .	<b>x</b>
<b>Chapter 1 Introduction</b> . . . . .	<b>1</b>
1.1 Background Thermodynamics . . . . .	2
1.2 Air Compression Systems . . . . .	3
1.3 Power Harvesting . . . . .	4
1.4 Principles of Thermoelectric Generators . . . . .	6
1.5 Power Harvesting Systems . . . . .	8
1.6 Surveying Locations for Temperature . . . . .	8
1.7 Research Objectives . . . . .	9
<b>Chapter 2 Temperature Surveying with Pyrometry</b> . . . . .	<b>10</b>
2.1 Principles of Infrared Temperature Measurements . . . . .	10
2.1.1 One Color Pyrometers . . . . .	12
2.1.2 Two Color Pyrometers . . . . .	14
2.2 Significance . . . . .	19
<b>Chapter 3 Mathematical Modeling</b> . . . . .	<b>24</b>
3.1 Thermal Pathways . . . . .	24
3.2 Thermal Pathway Modeling . . . . .	26
3.2.1 External Heat Transfer Modeling . . . . .	26
3.2.2 Internal Heat Transfer Modeling . . . . .	26
3.3 Conductance Modeling . . . . .	35
3.3.1 Hot Side Conductance ( $U_H$ ) . . . . .	35
3.3.2 Cold Side Conductance ( $U_L$ ) . . . . .	36
3.3.3 Contact Resistance . . . . .	39
3.3.4 Bypass Conductance ( $U_{bp}$ ) . . . . .	39
<b>Chapter 4 Economic Analysis</b> . . . . .	<b>45</b>
4.1 Initial Investment . . . . .	45
4.2 Back Work and Net Work . . . . .	46
4.3 Net Inflow . . . . .	46
4.4 Simple Payback Analysis . . . . .	47
4.5 Discounted Payback Period . . . . .	48
<b>Chapter 5 Optimization Approach</b> . . . . .	<b>50</b>
5.1 Power Output Solution . . . . .	50
5.2 System Optimization . . . . .	51

5.2.1	Backwork . . . . .	51
5.2.2	TEG Arrangement . . . . .	52
5.2.3	TEG Varieties and Cost . . . . .	56
5.2.4	Further Optimization Parameters . . . . .	57
5.3	Genetic Algorithm . . . . .	57
5.4	Optimization Overview . . . . .	59
<b>Chapter 6</b>	<b>Experimental Setup . . . . .</b>	<b>60</b>
6.1	Air Compressor Simulation Setup . . . . .	60
6.1.1	Thermal Measurements . . . . .	61
6.1.2	Air Speed Measurement . . . . .	63
6.1.3	Electrical Measurements . . . . .	66
6.2	Matched Load Experiment . . . . .	68
6.3	Thermal Pathways Experiment . . . . .	69
6.4	Installation on an Air Compressor . . . . .	69
<b>Chapter 7</b>	<b>Model Application and Results . . . . .</b>	<b>74</b>
7.1	Propagation of Uncertainty . . . . .	74
7.1.1	Model Uncertainty . . . . .	74
7.1.2	Experimental Uncertainty . . . . .	76
7.2	Thermoelectric Generator Varieties . . . . .	76
7.3	Bypass Conductance . . . . .	77
7.4	Model Validation . . . . .	78
7.4.1	Air Compressor Installation . . . . .	80
7.5	Air-cooled Case Study . . . . .	83
7.5.1	Economic Analysis . . . . .	83
7.5.2	Payback Period versus Source Temperature . . . . .	85
7.5.3	Payback Period versus Electric Cost . . . . .	86
7.6	Water Cooled Case Study . . . . .	88
7.6.1	Model Adaptation . . . . .	88
7.6.2	Evaluation . . . . .	92
7.7	Discussion . . . . .	92
<b>Chapter 8</b>	<b>Conclusions and Recommendations . . . . .</b>	<b>95</b>
8.1	Summary . . . . .	95
8.2	Limitations . . . . .	98
8.3	Recommendations . . . . .	99
<b>REFERENCES</b>	<b>. . . . .</b>	<b>101</b>
<b>Appendix A</b>	<b>Optimization Routine Code . . . . .</b>	<b>104</b>
A.1	Parameters File Code . . . . .	104
A.2	Economic Model Optimization . . . . .	107
A.2.1	Genetic Algorithm Optimization Code . . . . .	107
A.2.2	Economic Model Function Code . . . . .	112

A.3	Thermoelectric Generator Equation Solver . . . . .	117
A.3.1	Solver . . . . .	117
A.3.2	Function . . . . .	119
A.4	Heat Sink Solver Code . . . . .	121
A.4.1	Fan Correlation . . . . .	121
A.4.2	Heat Sink Conductance Solver . . . . .	122
A.5	Water Cool Case Study Code . . . . .	123
<b>Appendix B</b>	<b>Thermocouple Calibration Procedure . . . . .</b>	<b>125</b>
<b>Appendix C</b>	<b>Overall Seebeck Coefficient Measurement Procedure . . . . .</b>	<b>126</b>
<b>Appendix D</b>	<b>Air Compressor Experiment Design Documents . . . . .</b>	<b>128</b>
<b>Appendix E</b>	<b>Thermodynamic Properties of Water . . . . .</b>	<b>133</b>
<b>Appendix F</b>	<b>Validation of Power Output of TEGs in Series . . . . .</b>	<b>135</b>
<b>Appendix G</b>	<b>Heat Sink Derivation . . . . .</b>	<b>137</b>
<b>Appendix H</b>	<b>View Factor Program Pseudocode . . . . .</b>	<b>140</b>

## LIST OF TABLES

5.1 Individual power produced by TEGs as a fraction of the first TEG and the total power produced by a series of TEGs as a fraction of the first TEG . . . . .	55
7.1 TEG varieties with respective properties . . . . .	77
7.2 Parameters used for bypass conductance estimates . . . . .	78
7.3 Calculated estimates of bypass conductance parameters . . . . .	78
7.4 Measured parameters from air compressor simulation setup . . . . .	79
7.5 Parameters for heat sink in air compressor simulation setup . . . . .	79
7.6 Air properties used in air compressor simulation setup . . . . .	80
7.7 Fin material properties used in air compressor simulation . . . . .	80
7.8 TEG power model and measured results for air compressor power harvesting system . . . . .	83
7.9 Economic analysis parameters with intervals in months for air compressor simulation . . . . .	84
7.10 Comparison of $\Delta T$ values around and slightly greater than those found on an Air Compressor and their respective payback periods . . . . .	86
7.11 Comparison payback periods as a function of \$/kWh for prices ranging from average electric prices in the United States to slightly more . . . . .	87
7.12 Additional parameters for water cool case study . . . . .	92
7.13 Water cooled case study results with changing base cost . . . . .	93
E.1 Thermodynamic properties of water . . . . .	133
F.1 Data from TEGs in series with respect to heat sink for varying conditions . . . . .	135

## LIST OF FIGURES

1.1	Final temperature of compressed air as a function of the final pressure for a single stage compressor . . . . .	4
1.2	Sankey diagram of waste heat and the work of the system . . . . .	5
2.1	Diagram of radiative interactions between IR pyrometer, surface and the surroundings . . . . .	11
2.2	Error associated with a 1 color pyrometer . . . . .	15
2.3	Error associated with a 2 color pyrometer . . . . .	18
2.4	Image of an isothermal pipe showing variance in the temperature reading due to inconsistent surface conditions . . . . .	20
2.5	Normal spectral emissivity for varying wavelength and a variety of materials . . . . .	21
2.6	Chart illustrating the atmospheric participation in the form of relative transmission for a variety of wavelengths . . . . .	22
3.1	Thermal resistance diagram for a thermoelectric generator power harvesting system with resistances shown in conductances instead of resistances . . . . .	25
3.2	Thermal resistance diagram for a thermoelectric generator power harvesting system considering bypass heat transfer ( $U_{bp}$ ) with resistances shown in conductances instead of resistances . . . . .	25
3.3	Internal diagram for Peltier and Thomson heat transfer within the wires of a p-type and n-type pair . . . . .	27
3.4	Internal diagram for a thermoelectric circuit pair with an n-type and p-type semiconductor thermally in parallel and electrically in series with two boundary surfaces labeled with a dashed line . . . . .	29
3.5	Diagram illustrating dimensions of definitions of hot side conductance parameters . . . . .	36
3.6	Screen capture from Monte Carlo ray tracing simulation program of models used to estimate view factor with 1000 rays drawn . . . . .	43
3.7	Screen capture from Monte Carlo ray tracing simulation program used to estimate view factor with results . . . . .	43
5.1	Diagrams for thermoelectric generators in series and in parallel with respect to air flow . . . . .	52
5.2	Array of TEGs in combination of parallel and series implementation . . . . .	56
6.1	Standard and infrared images of air compressor with heat shield removed . . . . .	61
6.2	Diagram of experiment stack and temperature measurement locations . . . . .	62
6.3	Experimental setup with rectangular fin array, blower fan, and anemometer . . . . .	64
6.4	3D model of fan duct used to change area of fan opening and install anemometer . . . . .	64
6.5	Anemometer installed in 3D printed duct attachment for blower fan speed measurement . . . . .	65
6.6	Fan correlation function created using a 4th order polynomial regression on empirical data in terms of back work ( $p_{back}$ ) . . . . .	66
6.7	Wiring diagram for instrumentation measuring electrical power . . . . .	67
6.8	Resistive wire potentiometer with current shunt . . . . .	68

6.9	Power harvester installed on air compressor . . . . .	71
6.10	Isometric CAD drawing of power harvester design for air compressor experiment setup . . . . .	72
6.11	Infrared images of heat loss from of aluminum tubing leaving compressor for insulated vs. uninsulated installations . . . . .	72
7.1	TEG varieties considered for power harvester optimization . . . . .	77
7.2	Heat sink drawing with generic dimensions . . . . .	79
7.3	Comparison of gross power produced by TEG as predicted by model and measured with empirical data for varying the resistive load . . . . .	81
7.4	Comparison of TEG power produced by TEG as predicted by model and measured for varying fan power (of which $U_L$ is dependent) . . . . .	81
7.5	Comparison of TEG surface temperatures as predicted by model and measured with empirical data for varying backwork (of which air $U_L$ is dependent) . . . . .	82
7.6	Standard and infrared images of air compressor power harvester unit . . . . .	83
7.7	Plot of cumulative inflow as a function of months since installation . . . . .	84
7.8	Payback period as a function of the source temperature seen by the TEG . . . . .	86
7.9	Payback period as a function of the cost of electricity per kWh . . . . .	87
7.10	Cumulative inflow as a function of months of installation for a water-cooled TEG power harvesting system . . . . .	93
C.1	Wiring diagram for overall seebeck coefficient measurement . . . . .	127
D.1	Air Compressor TEG Installation Drawing: Exploded Assembly . . . . .	129
D.2	Air Compressor TEG Installation Drawing: Base Bottom Drawing . . . . .	130
D.3	Air Compressor TEG Installation Drawing: Base Top Drawing . . . . .	131
D.4	Air Compressor TEG Installation Drawing: Top Bar Drawing . . . . .	132
F.1	Standard and infrared images of a hot plate to show non-isothermal behavior . . . . .	136

## NOMENCLATURE

$A$	Area
$A_c$	Cross Sectional Area
$C$	Cost or Generic Constant of Integration/Differential Equation
$c$	Specific Heat
$F_{1 \rightarrow 2}$	View Factor from Surface 1 to Surface 2
$G$	Irradiation
$g$	Gravitational Constant (9.81 m/s <sup>2</sup> )
$h$	Convection Coefficient
$I$	Electrical Current or Radiative Intensity
$i$	Discount Rate
$k$	Thermal Conductivity
$L$	Length
$N$	Integer Quantity
$Nu$	Nusselt Number
$n$	Period
$P$	Perimeter
$p$	Work or Power Output
$Pr$	Prandtl Number
$q$	Heat Rate
$\dot{q}$	Volumetric Heat Generation
$R$	Electrical Resistance
$Ra$	Rayleigh Number
$Re$	Reynold's Number
$R_t$	Thermal Resistance
$R_{int}$	Internal Electrical TEG Resistance
$R_{load}$	External Electrical Load on TEG
$S$	Entropy
$T$	Temperature
$U$	Thermal Conductance
$u$	Air Stream Velocity
$V$	Voltage
$\mathcal{V}$	Volume
$\dot{\mathcal{V}}$	Volumetric Flow Rate
$Z$	Thermoelectric Figure of Merit

### Greek Letters

$\alpha$	Seebeck Coefficient
$\beta_\lambda$	Absorption Coefficient for Participating Media
$\Gamma$	Payback Period
$\varepsilon$	Second Law/Exergetic Efficiency Efficiency
$\varepsilon_r$	Emissivity Ratio
$\varepsilon_\lambda$	Spectral Emissivity
$\eta_c$	Carnot Efficiency

$\eta_{th}$	Thermal Efficiency
$\eta_f$	Single Fin Efficiency
$\eta_o$	Overall Fin Array Efficiency
$\theta$	$T - T_a$
$\lambda$	Wavelength
$\nu$	Kinematic Viscosity
$\pi$	Peltier Coefficient
$\rho$	Density or Reflectivity
$\rho_e$	Electrical Resistivity
$\sigma$	Standard Deviation or Stefan-Boltzmann Constant ( $5.67 \cdot 10^{-8} \text{ W/m}^2\text{-K}^2$ )
$\tau$	Thomson Coefficient
$\Omega$	Solid Angle or Ohms (when used as a unit)

### Subscripts, Superscripts, and Other Indicators

$[ ]_a$	indicates [ ] is ambient property
$[ ]_b$	indicates [ ] pertains to a blackbody
$[ ]_H$	indicates [ ] is property on the hot side of the TEG
$[ ]_L$	indicates [ ] is property on the cold side of the TEG
$[ ]_n$	indicates [ ] is property n-type thermoelectric material
$[ ]_o$	indicates [ ] is overall property of the TEG
$[ ]_p$	indicates [ ] is property p-type thermoelectric material
$[ ]_s$	indicates [ ] is source property
$[ ]_\lambda$	indicates [ ] is a spectral property
$\overline{[ ]}$	indicates that [ ] is an average property



## CHAPTER 1. INTRODUCTION

Power is a critical resource in keeping the world functioning. Electrical power is needed to complete virtually every process used on a day to day basis. With an ever increasing population as well as continuing industrial development, worldwide energy consumption is growing 1-3% each year [1]. The U.S. Energy Information Administration estimates as much as 72% of electrical power in the world is generated by fossil fuels [1]. Power generation based on use of fossil fuels has benefited from centuries of development. The existing technology and infrastructure for generation and distribution of power from fossil fuels results in low cost power that is essential for economic growth and prosperity. However, it is now widely recognized that the limited availability of fossil fuels and the environmental damage associated with mining or drilling for and combustion of fossil fuels makes the current approach to power generation unsustainable.

These downsides of fossil fuels have led to a push in recent years to develop other technologies that are capable of sustainably meeting the world's need for power. The National Academy of Engineering identified development of sustainable power generation as the foremost challenge facing engineering in the new millennium [2]. There are two methods for reducing the world's dependence on fossil fuels: creating new sources of power to replace fossil fuels and reducing power consumption. Aside from not using energy in the first place, reducing energy consumption primarily involves increasing the efficiency of processes so that they use less energy to accomplish their designed functions. In every process, energy not used for the intended purpose is converted to waste heat and lost.

The objective of this research is to evaluate the use of TEG based power harvesting systems in air compression systems. Air compression systems were selected because they are widely used [3] and because they have low energy conversion efficiencies [4]. Power harvesting systems have the ability to recover some of this waste heat and turn it into useful power. Research

and development into this area is critical to reducing dependence on fossil fuels and ensuring a sustainable future.

## 1.1 Background Thermodynamics

This section describes thermodynamic analysis that motivates this research. The reader is also directed to a standard thermodynamics textbook for more information (such as *Thermodynamics* by Cengel and Boles [5]). Readers with a background in thermodynamics will find this section a review.

All processes occurring in day to day life involve energy conversion. They convert energy from one form (electrical, thermal, or chemical) to another form (mechanical energy). The first law of thermodynamics specifies that energy cannot be created or destroyed. Energy input or energy transferred to a system during a process is either stored in some form in the system or transferred from the system to its surroundings. The first law of thermodynamics is complemented by the second law of thermodynamics which introduces the concept of entropy. Entropy is a measure of disorder of the universe. According to the second law, natural processes spontaneously flow from ordered states to less ordered states. In other words, entropy is generated during all processes, and this is the basis for a second law analysis. A second law analysis predicts that the temperature of a warm cup of water will decrease and never increase when it is left on a table. A second law analysis also predicts that a process designed to convert electrical energy into mechanical energy will have an energy conversion efficiency that is less than 100% [5]. Since energy is conserved, the electrical energy not converted to mechanical energy is converted to thermal energy, which is then transferred to the surroundings as disordered waste heat.

While generation of some waste heat is unavoidable, the amount of waste heat transferred to the surroundings can be minimized. Systems designed to reclaim and use thermal energy may be classified as heat recovery systems or as power harvesting systems. Heat recovery systems extract thermal energy from sources of waste heat and use the recovered thermal energy for space or water heating. Power harvesters extract thermal energy from sources of waste heat and use the recovered thermal energy to drive a heat engine and produce electrical power. Power harvesting systems minimize the amount of waste heat by converting a fraction of this thermal energy into

useful electrical energy. Including a power harvesting system in the design of a process (such as an air compressor) can improve the energy conversion efficiency of the overall system [5].

## 1.2 Air Compression Systems

This section describes the potential of implementing power harvesting systems in air compression systems.

Air compressors are used widely in industrial shops as well as home applications for cleaning as well as a source of power for pneumatic tools. Compressed air is so prevalent that it is often referred to as the 4th utility (with water, electricity, and natural gas as the other utilities) [3]. While home applications rarely use over 200 psi (1,379 kPa), some industrial shop applications operate at well over 500 psi (3,447 kPa) [4]. In industrial facilities, air compression systems can account for as much as 30% of the facility's energy costs [6]. The total installed power of air compression systems in the United States is approximately 13 GW [7]. Since the energy conversion efficiency of air compression systems is 7 - 20%, these systems generate 10 -12 GW of waste heat. Converting only 1% of this waste heat to electrical power would eliminate the need for 100 - 120 MW of fossil fuel power generation.

When the pressure of the air within the air compressor is increased, the air temperature increases. This process can be approximated using a polytropic process as seen in Equation 1.1.

$$\frac{T_2}{T_1} = \frac{P_2}{P_1}^{\frac{n-1}{n}} \quad (1.1)$$

As the air temperature increases, the compressor must work harder to compress the air. In some situations, to overcome this detriment, two stage compressors are implemented to keep the temperatures lower. These compressors use an intercooler between two compression stages to cool the air. In this case, waste heat is evacuated from the intercooler. In either case, the compressed air leaves the air compressor much hotter than when it entered—advecting a significant amount of thermal energy. The temperatures increase with increasing final pressures. The plot of Equation 1.1 as a function of final pressure can be seen in Figure 1.1. This plot illustrates how the final temperature increases significantly as the final pressure increases.

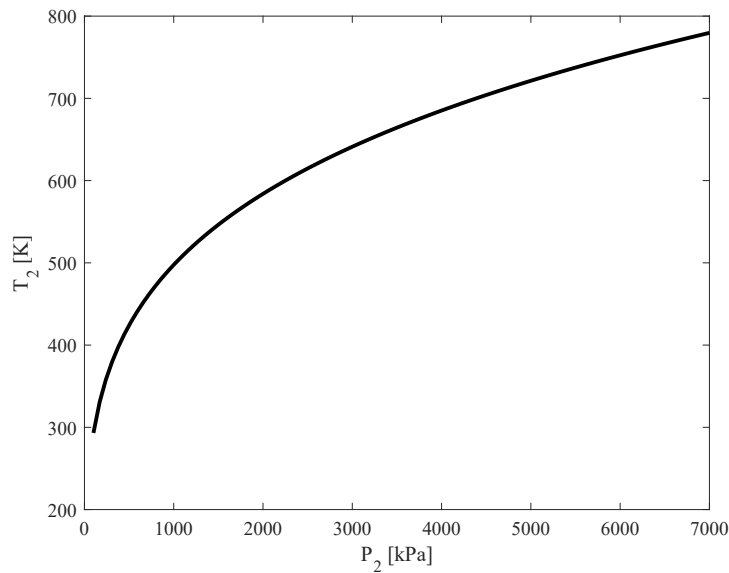


Figure 1.1: Final temperature of compressed air as a function of the final pressure for a single stage compressor

The high temperature of the air stream heats up the pipes leading from the air compressor and other portions of the unit. These surfaces will also become heated as the compressed air moves through the system. The surface's proximity to the relatively low temperature ambient air surrounding the compressor suggests that implementing power harvesting systems in an air compressor is a good idea.

### 1.3 Power Harvesting

This section will discuss the benefits of recovering waste heat as well as the properties behind recovering waste heat. A byproduct of most processes is conversion of power to heat. This heat is referred to as waste heat because it goes generally unused. It can be beneficial to recover some of this waste heat in the form of useful power as it improves the overall efficiency of the system. Figure 1.2 shows a Sankey diagram of a simplified air compressor system. As previously discussed, the objective of an air compressor is to produce high pressure air. Viewed as an energy conversion device, an air compressor converts the input energy into flow energy,  $PV$ . However, compressors convert only a small fraction of the input energy into flow energy, and most of the

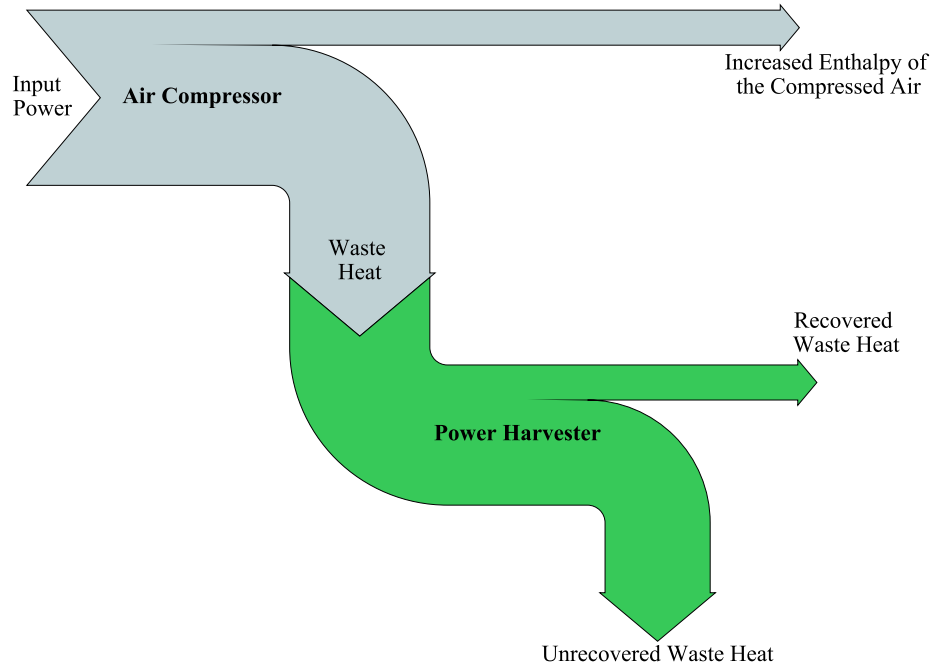


Figure 1.2: Sankey diagram of waste heat and the work of the system

input energy is lost to the surroundings as waste heat. From this perspective, air compressors are highly inefficient [8].

The energy conversion efficiency of an air compression system may be defined as the ratio of the flow energy of the air exiting the compressor to the input energy:

$$\eta = \frac{PV}{P_{elec}} \quad (1.2)$$

The energy conversion efficiency differs from the isentropic efficiency and the isothermal efficiency of a compressor. These efficiencies compare the actual power required by a compressor to the power that would be required if the compressor followed a hypothetical ideal isentropic or isothermal process [5].

Air compressors typically have energy conversion efficiencies less than 20% [6], so 80% or more of the electrical energy supplied to a typical air compression system ends up as low grade thermal energy in the air stream. Since the exergy of air stream is low, only a small fraction of the waste heat may be converted into electrical power [5]. However, the widespread use of air

compression systems means that the cumulative effect of implementing power harvesters in air compression systems could be significant.

#### 1.4 Principles of Thermoelectric Generators

This section will discuss the properties and phenomena related to thermoelectric materials which are pertinent to this work. For further information on thermoelectric generators and materials, the reader is directed to any number of works on the subject such as *CRC Handbook of Thermoelectrics* [9] or *Thermal Design* [10].

Thermoelectric generators rely on thermoelectric materials to directly turn thermal energy into electrical energy. They usually compose sets of 2 types of thermoelectric materials: p-type and n-type. In the p-type thermoelectric material, electrons diffuse towards the hot side of the thermoelectric element while the opposite is true for the n-type thermoelectric material. These thermoelectric couples, when in the presence of a temperature differential, generate electrical current. This process also works in the reverse—that is when a current is supplied, a temperature differential is created. These are called thermoelectric coolers or Peltier coolers.

The physical behavior of thermoelectric generators is governed by three principles: the Seebeck effect, the Thomson effect and the Peltier effect [10]. The Seebeck effect is the phenomena when a temperature gradient is maintained at the junctions of two dissimilar metals, a voltage is produced. This effect is characterized by the Seebeck coefficient,  $\alpha$ , which has the units of V/K or mV/K—which represents a voltage differential per temperature differential.

$$V = \alpha_o \Delta T \quad (1.3)$$

where  $\alpha_o$  is the net overall seebeck coefficient:

$$\alpha_o = \alpha_p - \alpha_n$$

The Peltier effect is heating or cooling when a current is passed through two dissimilar metals. It is the opposite of the Seebeck effect and the process by which Peltier coolers are possible. It is characterized by the Peltier coefficient,  $\pi$  (Equation 1.4) as well as the current flowing through

the system,  $I$ .

$$q_{peltier} = \pi_o I \quad (1.4)$$

The Thomson effect is the phenomena where heat is either added or removed along a material's length as a function of an induced temperature gradient as well as the imposed current [10]. It is characterized by the Thomson coefficient,  $\tau$  (Equation 1.5).

$$q_{thomson} = \tau I \Delta T \quad (1.5)$$

Additionally, Joule heating occurs within the TEG due to the presence of current flowing through a wire. This is governed by Ohm's Law:

$$q_{joule} = I^2 R \quad (1.6)$$

These phenomena act simultaneously on a thermoelectric generator (or cooler) while it is in operation (e.g. Seebeck effect produces current which causes the Peltier effect to produce heat). The effectiveness of a TEG is sometimes rated using the thermoelectric figure of merit. This figure of merit (Equation 1.7) is a function of the Seebeck coefficient,  $\alpha$ , electrical resistivity,  $\rho_e$ , and thermal conductivity,  $k$ .

$$Z = \frac{\alpha^2}{\rho_e k} \quad (1.7)$$

While the TEG figure of merit is not used for the analysis in this work, it is beneficial to visualize parameters that can improve TEG function. Devices with a higher thermoelectric figure of merit tend to be more desirable as they can produce more power for a given temperature differential. Therefore, TEGs with higher Seebeck coefficients and lower electrical resistivity and thermal conductivity are desirable for effective power harvesting systems.

## 1.5 Power Harvesting Systems

In order for a power harvesting system to be effective, it needs to be placed in a location where there is a significant amount of exergy. Exergy is the measure of energy that can be used to produce work and is a function of potential energy, kinetic energy, entropy, and enthalpy. In a stationary system, a majority of this available energy is in the form of enthalpy. Enthalpy is a function of temperature ( $h = C_p\Delta T$ ) for an ideal gas. Because of the need for a system to reject energy to its surroundings, the concept of exergy takes into account the energy of a system relative to a dead state. The power harvesting system should be installed in the location of greatest temperature difference between the surface and the surrounding, if possible, to maximize power harvesting. The temperatures of potential sites must be surveyed in order to determine this ideal location.

## 1.6 Surveying Locations for Temperature

There are a variety of methods to measure the temperature of a surface. Contact and non-contact thermometers each have advantages and disadvantages for their use. Thermometers that require the probe be in contact with the sample are referred to as contact thermometers. Contact thermometers require that the probe come to thermal equilibrium with the sample, which can increase the time needed for a final reading.

Non-contact thermometers, or infrared (IR) pyrometers, are vital to several fields (such as smelting), where the temperature to be measured is much hotter than the melting point of a metal contact thermometer. In these situations where contact temperature measurements are inadequate, non-contact infrared pyrometry offers the ability to easily measure temperature quickly and efficiently. Infrared pyrometers also tend to produce readings quicker than contact thermometers. These benefits, combined with their inherent convenience, make them a prime candidate for surveying possible sites for power harvesting.

Surveying sites for power harvesting is a special use case of IR pyrometers. Sampling many sites increases the probability that the optimum placement of the power harvesting device will be found. Even with the many benefits of IR pyrometry, there are a few areas which can introduce inaccuracies into the temperature measurement. This thesis will discuss these areas, as well as how to minimize them.



## 1.7 Research Objectives

This thesis sets forth the following objectives which were achieved over the course of this research. This thesis aims to:

1. Demonstrate how infrared pyrometers may be used to identify promising locations for power harvesting,
2. Model the power output from the designed thermoelectric power harvesting system,
3. Create an idealized experiment to validate the model of the optimized power harvesting system,
4. Design an experimental thermoelectric generator based power harvesting system for an air compressor,
5. Evaluate the feasibility of the power harvesting system using engineering economic analysis.

## CHAPTER 2. TEMPERATURE SURVEYING WITH PYROMETRY

Non-contact thermometers, or infrared (IR) pyrometers, are vital to several fields (such as smelting) where the temperature to be measured is much hotter than the melting point of thermometers. In these situations, non-contact infrared pyrometry offers the ability to remotely measure surface temperatures quickly and efficiently. Infrared pyrometers also produce readings quicker than contact thermometers as contact temperature measurements require setup and installation in order to get good contact with the surface. Infrared cameras offer the functionality of taking several temperature readings and portraying a thermal image of the field of view—conveniently illustrating the surface temperature profile of the target. These benefits, combined with their inherent convenience, make them a prime candidate as a tool for surveying possible sites for power harvesting.

The ability to quickly determine the temperature of various surfaces and identify optimal locations for installing power harvesters is another application in which use of IR pyrometry is advantageous. Sampling many sites ensures that the power harvesting device will be placed in the optimal location. While qualitative information regarding surface temperatures is easily obtained using IR pyrometry, obtaining accurate quantitative temperature measurements requires careful interpretation of the data. Being aware of the limitations of IR pyrometers is crucial to proper use of these devices in surveying locations for power harvesting. This chapter will discuss these limitations, as well as how to minimize these limitations.

### 2.1 Principles of Infrared Temperature Measurements

Infrared pyrometry is a form of non-contact thermometry that can be used to measure the surface temperature of an object. Infrared pyrometers measure the voltage produced by a photovoltaic device that is exposed to IR radiation. This voltage is proportional to the spectral irradiation incident on the detector,  $V_s \propto G_\lambda$ . As illustrated in 2.1, the spectral irradiation is a function of the radiation emitted by the target, the radiation emitted by the surrounding surfaces that is reflected

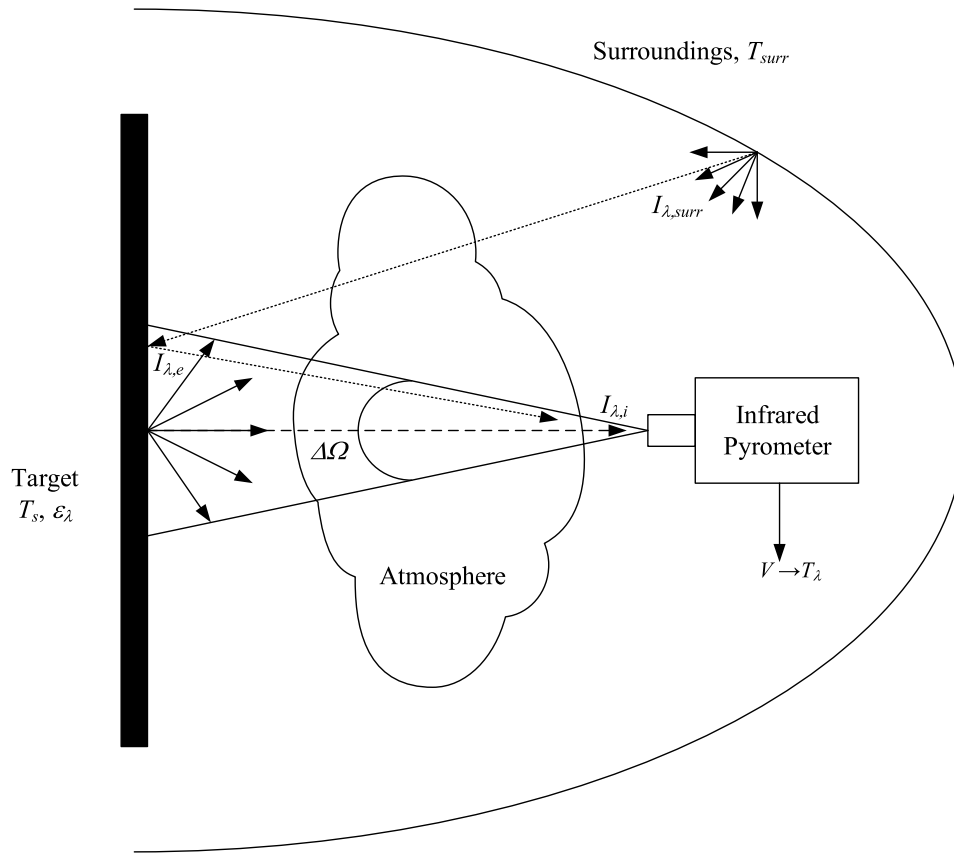


Figure 2.1: Diagram of radiative interactions between IR pyrometer, surface and the surroundings

from the target, and the absorption and scattering of radiation by the atmosphere. Therefore, IR pyrometers requires a model relating the measured voltage to the temperature of the target surface.

Infrared pyrometers are classified by the number of wavelengths used. The sensor in a one color pyrometer is sensitive to the spectral irradiation in a narrow spectral band around a single wavelength. Sensors in two color pyrometers are sensitive to the spectral irradiation incident in narrow bands surrounding two wavelengths. Multi-spectral methods have also been investigated [11–13]. The following sections develop models that relate the surface temperature of the target to the voltage measured by one color and two color pyrometers.

### 2.1.1 One Color Pyrometers

One color infrared pyrometers measure the intensity incident on the detector from a surface where the pyrometer is aimed. Because the spectral irradiation is proportional to the voltage generated by the sensor, the voltage can be related to the irradiation by a calibration factor,  $f_{cal}G_\lambda = V$ .

The spectral irradiation is defined as

$$G_\lambda = \int_{2\pi} I_{\lambda,i} \cos \theta \, d\Omega \quad (2.1)$$

Because the sensor is exposed to irradiation over a hemisphere, baffles or other means are used to narrow the field of view of the sensor. Additionally, the irradiation from the surface is normal to the sensor. This makes the intensity incident upon the sensor

$$I_{\lambda,i} = \begin{cases} I_{\lambda,i} & \Omega = \Delta\Omega_{d \rightarrow s} \\ 0 & \Omega \neq \Delta\Omega_{d \rightarrow s} \end{cases} \quad (2.2)$$

where  $\Delta\Omega_{d \rightarrow s}$  is the solid angle subtended by the surface when viewed from the detector.

The irradiation from the surface may be due to radiative emission from the surface, reflection of radiation emitted from the surroundings off of the surface, and emission by high temperature gases between the target, and the detector as well as from the surroundings (see Figure 2.1). Neglecting scattering into the line of sight connecting the target and the detector, the intensity at any point along the line of sight from the surface to the detector will be

$$I_\lambda(L_d) = (I_{\lambda,e} + \rho_\lambda I_{\lambda,surr})e^{-\beta_\lambda L_d} \quad (2.3)$$

where  $L_d$  is the distance from the surface to the detector and  $\beta_\lambda$  is the absorption coefficient [14]. Making the assumption that the atmosphere is nonparticipating ( $\beta_\lambda = 0$ ) and that the temperature of the surroundings is such that  $I_{\lambda,surr} = 0$  yields

$$I_{\lambda,i} = I_{\lambda,e} \quad (2.4)$$

The definition of spectral, normal emissivity is:

$$\varepsilon_{\lambda,n} = \frac{I_{\lambda,e}}{I_{b,\lambda}(T_s)} \quad (2.5)$$

Substituting Equation 2.4 into Equation 2.5 and rearranging yields

$$I_{\lambda,i} = \varepsilon_{\lambda,n} I_{b,\lambda}(T_s) \quad (2.6)$$

Using Equation 2.1, the irradiation seen by the detector (assuming  $\Delta\Omega_{d \rightarrow s}$  is small) is

$$G_\lambda = I_{b,\lambda}(T_\lambda) \Delta\Omega_{d \rightarrow s} \quad (2.7)$$

Recall that sensor voltage and irradiation are related by a calibration constant. Equation 2.7 can be used to calculate the temperature based on the measured irradiation measured by the sensor. Those wishing to calibrate a pyrometer must measure the temperature of a black body and calculate the calibration constant for the sensor.

In order to calculate the possible error associated with the pyrometer, irradiation from a black body and the actual irradiation must be equated. Using the equation for spectral, black body intensity [15] and applying Wein's approximation ( $\exp[c_2/\lambda T \gg 1]$ ),  $I_{b,\lambda}(T)$  becomes

$$\begin{aligned} I_{b,\lambda}(T_s) &= \frac{c_1}{\pi \lambda^5 \exp\left(\frac{c_2}{\lambda T_s} - 1\right)} \\ &\approx \frac{c_1}{\pi \lambda^5 \exp\left(\frac{c_2}{\lambda T_s}\right)} \end{aligned} \quad (2.8)$$

This equation represents the intensity from the surface if it were a black body.

When Equation 2.8 is used for incident intensity instead of black body intensity, the actual surface temperature ( $T_s$ ) is replaced with an apparent temperature ( $T_a$ ):

$$I_{\lambda,i}(T_{a,1C}) \approx \frac{c_1}{\pi \lambda^5 \exp\left(\frac{c_2}{\lambda T_{a,1C}}\right)} \quad (2.9)$$

This equation represents the intensity incident on the detector in terms of the apparent temperature of the surface.

Substituting Equations 2.8 and 2.9 into Equation 2.6 and algebraic manipulation yields Equation 2.10.

$$\frac{1}{T_s} = \frac{1}{T_{a,1C}} + \frac{\lambda}{c_2} \ln(\epsilon_{\lambda,n}) \quad (2.10)$$

where  $T_{a,1C}$  is the apparent temperature from a one color pyrometer (which is the temperature reported when  $\epsilon_{\lambda}$  is assumed to be 1) and  $T_s$  is the actual surface temperature. Equation 2.10 shows the relationship between the measured temperature and the actual temperature of the surface. It is useful to solve Equation 2.10 for the ratio of apparent temperature and the actual surface temperature:

$$\frac{T_{a,1C}}{T_s} = \frac{1}{1 - \frac{\lambda T_s}{c_2} \ln(\epsilon_{\lambda,n})} \quad (2.11)$$

Unless the object emits radiation as a black body (i.e. where the spectral, hemispherical emissivity ( $\epsilon_{\lambda}$ ) of an object is 1) the measured intensity will be less than the ideal intensity (temperature ratio in Equation 2.2 less than 1). This means that the temperature measured (without correction) will always be lower than the actual surface temperature.

When the ratio  $T_{a,1C}/T_s$  is close to 1, the pyrometer is measuring the temperature relatively accurately—that is, the measured temperature is very close to the actual temperature. A plot of Equation 2.11 can be seen in Figure 2.2 with varying wavelength, surface temperature, and emissivity. Based on this plot, the error is minimized as the spectral emissivity approaches one. The apparent temperature will be the same as the actual surface temperature if the spectral emissivity at the sampled wavelength is 1, regardless of the spectral emissivity at other wavelengths. All other situations will yield an apparent temperature that is lower than the actual surface temperature.

### 2.1.2 Two Color Pyrometers

Instead of measuring the voltage at a single wavelength, two color pyrometers measure the voltage at two wavelengths and compare the ratio of voltages. This ratio of voltages readily

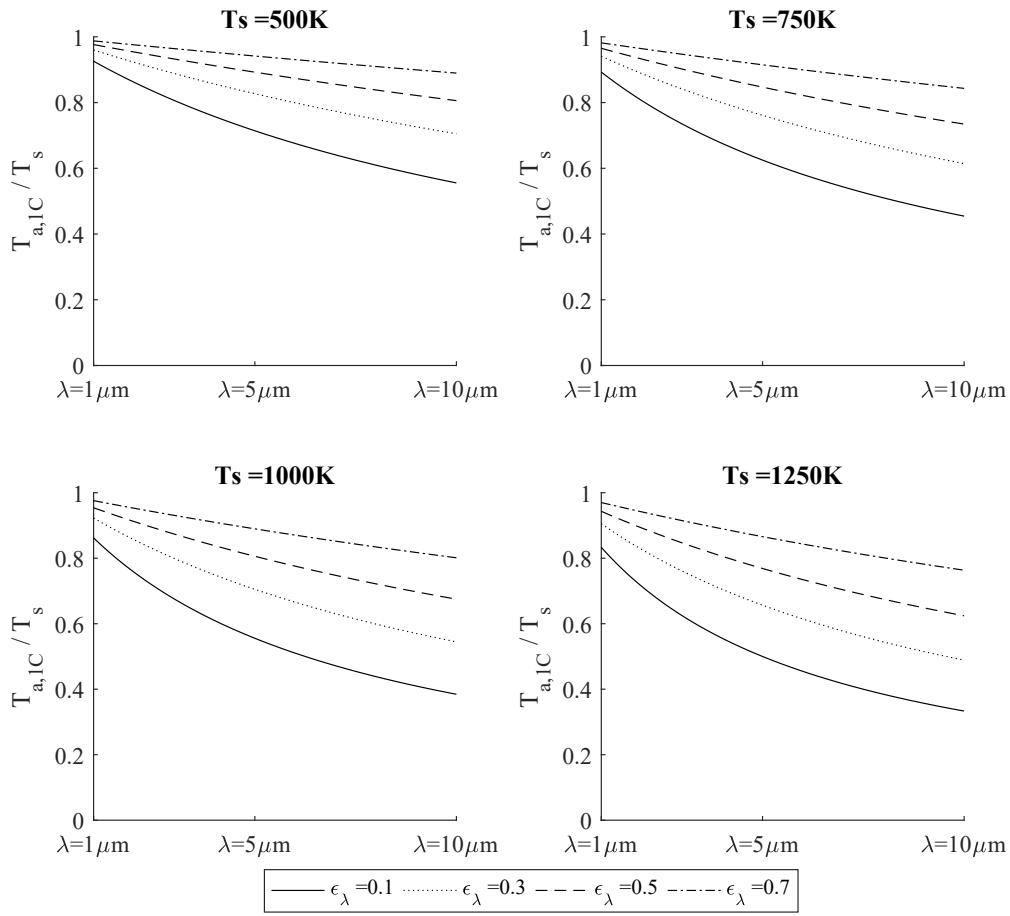


Figure 2.2: Error associated with a 1 color pyrometer

converts to the spectral irradiation ratio:

$$R(T_s) = \frac{G_{\lambda+\Delta\lambda}}{G_{\lambda}} \quad (2.12)$$

As with the one color case, irradiation on the sensor is (Equation 2.7),

$$G_{\lambda} = \epsilon_{\lambda} I_{b,\lambda}(T_s) \Delta\Omega_{d \rightarrow s} \quad (2.13)$$

Using the ratio in Equation 2.12 can minimize the effects of the varying emissivity as seen with the one color case. It is likely that the irradiation at a wavelength will be similar to the irradiation at another wavelength separated by a small  $\Delta\lambda$ —even if the emissivity is unknown.

Again, the equation for a black body using Wein's approximation becomes:

$$I_{b,\lambda}(T_s) \approx \frac{c_1}{\pi \lambda^5 \exp\left(\frac{c_2}{\lambda T_s}\right)} \quad (2.14)$$

Combining Equations 2.12, 2.13 and 2.14 with algebraic manipulation yields the equation:

$$\begin{aligned} \varepsilon_r R &= \left(\frac{\lambda}{\lambda + \Delta\lambda}\right)^5 \exp\left[\frac{c_2}{\lambda T_s} \left(\frac{\Delta\lambda}{\lambda + \Delta\lambda}\right)\right] \\ &= \left(\frac{\lambda^2}{\lambda_e \Delta\lambda}\right)^5 \exp\left[\frac{c_2}{\lambda_e T_s}\right] \end{aligned} \quad (2.15)$$

where,

$$\varepsilon_r = \frac{\varepsilon_\lambda}{\varepsilon_{\lambda + \Delta\lambda}} \quad (2.16)$$

$$\lambda_e = \frac{\lambda(\lambda + \Delta\lambda)}{\Delta\lambda} \quad (2.17)$$

Further manipulation of Equation 2.15 yields,

$$\begin{aligned} \exp\left(\frac{c_2}{\lambda_e T_s}\right) &= \varepsilon_r R \left(\frac{\lambda_e \Delta\lambda}{\lambda^2}\right)^5 \\ \frac{c_2}{\lambda_e T_s} &= \ln(\varepsilon_r) + \ln(R) + 5 \ln\left(\frac{\lambda_e \Delta\lambda}{\lambda^2}\right) \end{aligned} \quad (2.18)$$

The ratio of spectral emissivities is unknown, so a value must be assumed to obtain a value for surface temperature. As was mentioned earlier, the spectral emissivity values of the surface are likely to be similar when separated by a small wavelength. Therefore, the surface is assumed to be gray, or  $\varepsilon_r = 1$ . This yields an Equation 2.18 for the apparent temperature:

$$\frac{c_2}{\lambda_e T_{a,2C}} = \ln(R) + 5 \ln\left(\frac{\lambda_e \Delta\lambda}{\lambda^2}\right) \quad (2.19)$$

Substituting Equation 2.19 into 2.18 yields:



$$\begin{aligned}\frac{c_2}{\lambda_e T_s} &= \frac{c_2}{\lambda_e T_{a,2C}} + \ln(\epsilon_r) \\ \frac{1}{T_s} &= \frac{1}{T_{a,2C}} + \frac{\lambda_e}{c_2} \ln(\epsilon_r)\end{aligned}\quad (2.20)$$

Equation 2.20 is of the same form as Equation 2.10. With the same algebra as used in the case of the one color pyrometer (Section 2.1.1), a ratio of apparent to surface temperatures can be found. Additionally, substituting the definition of  $\lambda_e$  (Equation 2.17) allows for plotting on the same axis as in Figure 2.2.

$$\begin{aligned}\frac{T_{a,2C}}{T_s} &= \frac{1}{1 - \frac{\lambda_e T_s}{c_2} \ln(\epsilon_r)} \\ &= \frac{1}{1 - \frac{T_s}{c_2} \left( \frac{\lambda(\lambda + \Delta\lambda)}{\Delta\lambda} \right) \ln(\epsilon_r)}\end{aligned}\quad (2.21)$$

Equation 2.21 can be seen plotted in Figure 2.3 with varying parameters of surface temperature ( $T_s$ ) and the difference between wavelength sample ( $\Delta\lambda$ ).

In the same manner as the one color pyrometer, when  $T_{a,2C}/T_s$  is close to one, the pyrometer is measuring the temperature accurately. In this case, the apparent temperature will be the same as the actual surface temperature if the ratio of spectral emissivities at the sampled wavelengths is 1. All other situations will yield an apparent temperature that is different than the actual surface temperature.

Even though the expression for the ratio of  $T_{a,2C}$  to  $T_s$  is mathematically similar to the ratio of  $T_{a,1C}$  to  $T_s$ , there are critical differences between them. For a one color pyrometer, the ratio of apparent to surface temperature must be less than one because spectral emissivities must always be less than one. For a two color pyrometer, the emissivity ratio can be more than one. In this case, the ratio of apparent to surface temperature for two color pyrometers to surface temperature can be greater than one. This means that the reading from the pyrometer can overestimate the temperature of the surface under certain circumstances. These situations can be seen in red on Figure 2.3. The temperature ratio's deviation from one is about the same amount for the same amount of deviation from an emissivity ratio. In other words, an  $\epsilon_r$  of 0.9 and 1.1 both yield about the same amount of

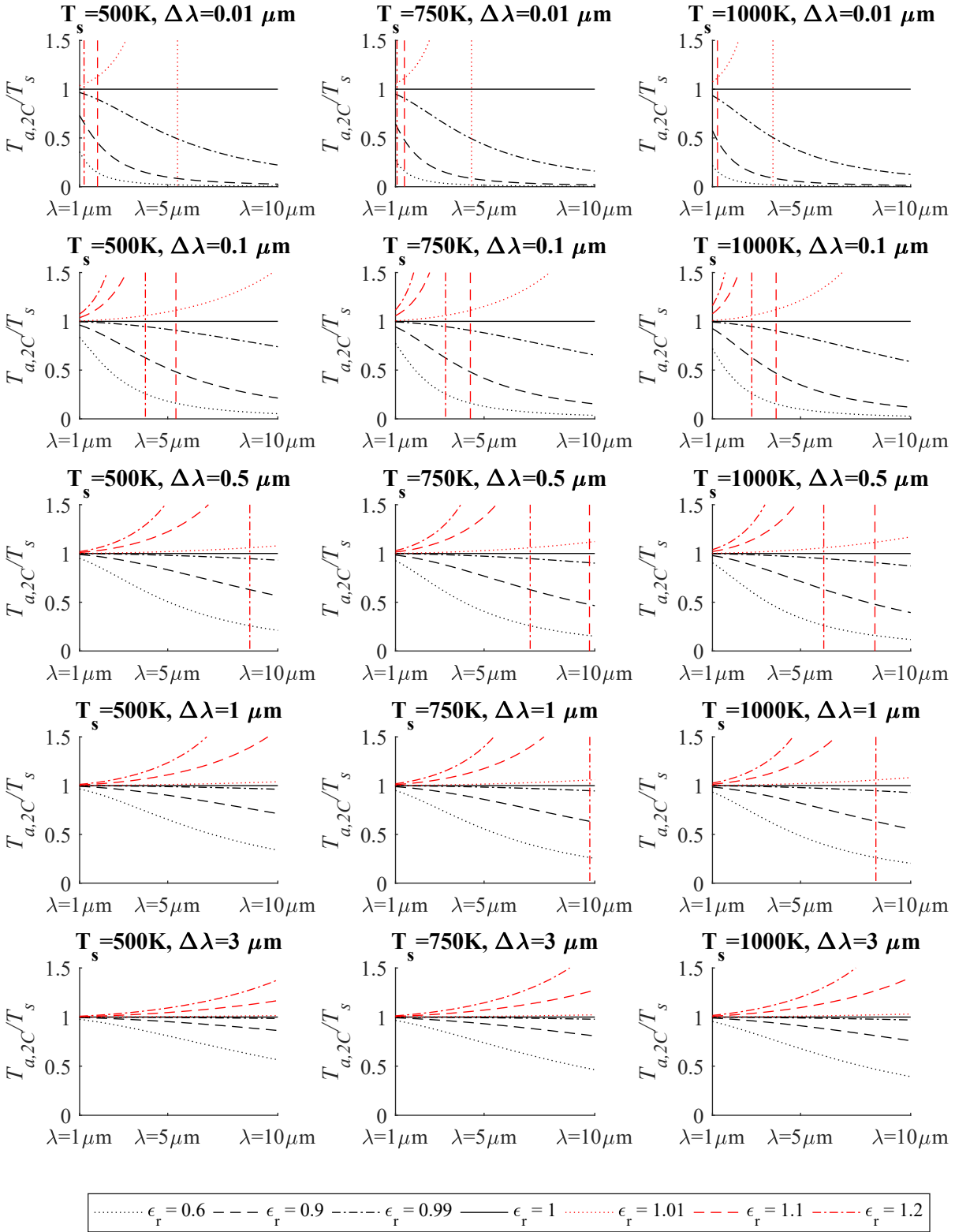


Figure 2.3: Error associated with a 2 color pyrometer

error, just in different directions. An emissivity ratio of 1.1 will yield a higher apparent temperature while 0.9 will yield one that is lower. One downside of having an emissivity ratio greater than 1 is in some situations, the apparent temperature ratio increases drastically towards an asymptote. This is not a large issue because the situations where this occurs already have large errors for many cases (e.g.  $\Delta\lambda < 0.5$ ). These asymptotes can be seen as vertical lines (in red) in Figure 2.3.

## 2.2 Significance

In order to use a one color pyrometer accurately, the obtained apparent temperature must be corrected using a value for spectral emissivity. Estimating spectral emissivity is incredibly difficult as it depends heavily on surface characteristics. For example, highly polished, pure Aluminum can have an emissivity of less than 0.1. When the surface heavily oxidizes, its emissivity can vary widely with temperature and be as large as 0.63 [14]. Depending on temperature and surface conditions (i.e. level of oxidation, cleanliness, etc.) the emissivity can vary further. This variance in emissivity can cause inaccurate temperature measurements as seen in Figure 2.4. This figure shows a pipe surface that is assumed to be close to isothermal. The surface temperature variances should be smooth and minimal. This pipe is made from aluminum and has portions of residual thermal paste, dirt, and some corrosion. The apparent temperature across the surface of this pipe as read by a one color pyrometer varies by as much as 40°C in a short distance. Without an experimental setup, it is very difficult to determine the emissivity of a surface with a reasonable degree of accuracy. Furthermore, the emissivity that is calculated in an experiment setup would only be valid for a certain specimen under controlled circumstances—a far from practical proposition for real world scenarios. Based on Figure 2.2, the ratio of apparent temperature versus actual temperature gets smaller with decreasing spectral emissivity. This ratio varies significantly depending on the selected emissivity. However, improper spectral emissivity selection (e.g. using a spectral emissivity of 0.3 when the actual spectral emissivity is 0.5) can yield temperature errors of 10% or more relative to the actual surface temperature.

Two color pyrometers can help to mitigate this error. Similar to the one color pyrometer, the user must input a parameter to properly measure the temperature of the surface. In this case, it is not the spectral emissivity but the ratio of emissivities seen at the respective frequencies. This ratio, if chosen carefully, is likely to be close to 1. Caution should be taken to avoid areas where

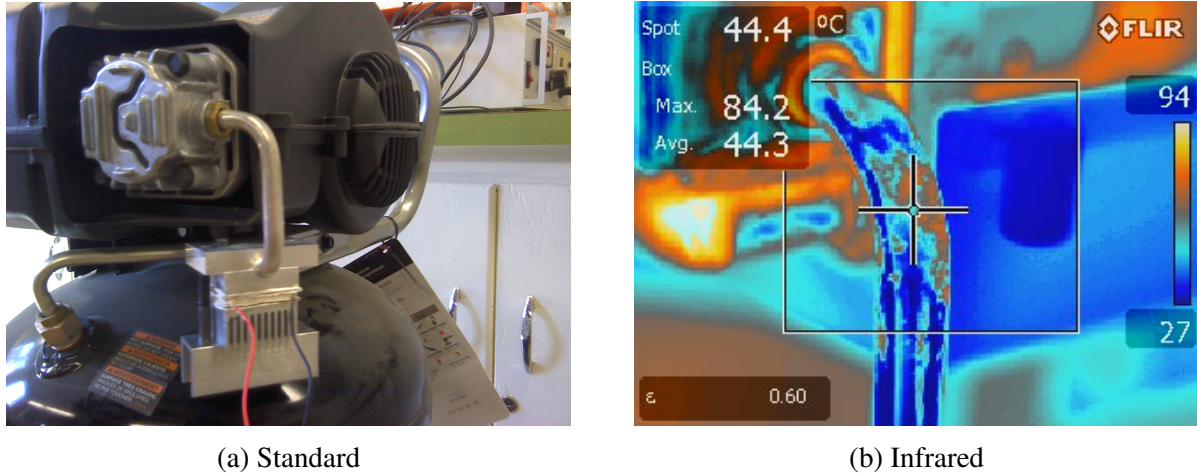


Figure 2.4: Standard image (a) and infrared image (b) of an isothermal pipe showing variance in the temperature reading due to inconsistent surface conditions

a discontinuity is found (such as asymptotes in Figure 2.3) in the two color temperature ratio function.

To further illustrate this principle, the case of a gray surface where the spectral emissivity is the same regardless of wavelength will be explored. If the temperature of a gray surface were to be measured with a one color pyrometer, the user must estimate the emissivity of the surface. Their estimation is subject to the error previously discussed as far as surface characteristics. Using the two color pyrometer in this case would eliminate the need for the estimation because it is known that the emissivity ratio for a gray surface for any two wavelengths is 1.

For a real surface, the emissivity ratio is not guaranteed to be 1. When selected carefully, it is possible to find a region where the spectral emissivity values are similar, yielding a value very close to 1—irrespective of what the actual values of  $\epsilon_\lambda$  are. The emissivity of a surface is less likely to vary as much when they are separated by a small  $\Delta\lambda$ . As seen in Figure 2.3, choosing too small of a  $\Delta\lambda$  value causes a large discrepancy between the apparent and actual surface temperatures, while increasing the  $\Delta\lambda$  of the readings decreases the discrepancy between the two temperatures. Finding two wavelengths that are separated by a large  $\Delta\lambda$  that have the same spectral emissivity can be difficult for some materials.

Another trend that can be seen with both one and two color pyrometers is that higher surface temperatures increases the discrepancy between the apparent temperature and the actual surface temperature. Furthermore, as previously mentioned, shorter wavelengths have less associated error

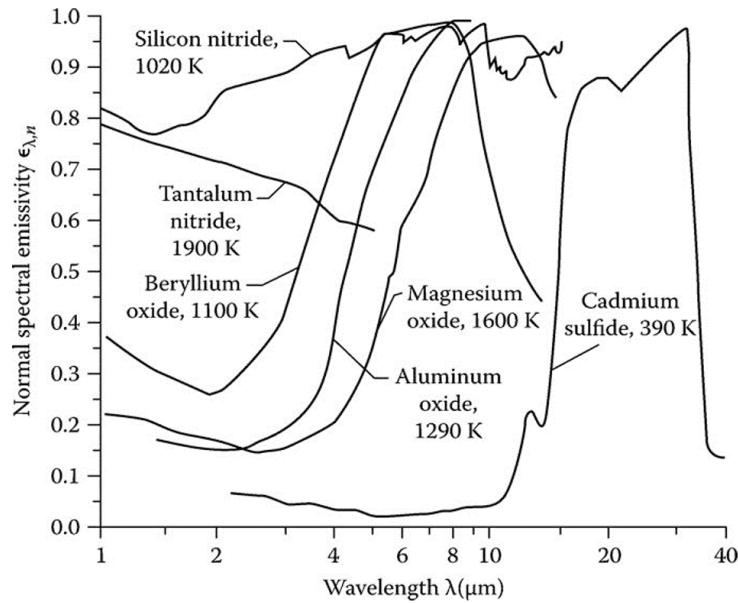


Figure 2.5: Normal spectral emissivity for varying wavelength and a variety of materials [16]

than those of longer wavelengths. That is, the apparent temperature to surface temperature ratio approaches one as the wavelength decreases. Therefore, choosing a wavelength that is smaller can help to minimize the error associated with using these devices.

An additional characteristic that must be considered is the atmospheric participation. In the model derivation in the previous sections, it was assumed that surroundings were non participating media. This is a good assumption as long as the spectral absorptivity of the surrounding air is small. The atmosphere has several spectral bands that are considered “atmospheric windows” where the atmosphere can be considered non-participating [14]. An image of the relative transmission of the atmosphere as a function of wavelength can be seen in Figure 2.6. Between the wavelengths of 8-14  $\mu\text{m}$  is a large window. If the surroundings are around 300-400 K, based on Wein’s law, it is known that the emission by the surroundings is significant between the wavelengths of 8-14  $\mu\text{m}$ . Because of the emissions from the surrounding at those wavelengths, selecting wavelengths of between 3-5  $\mu\text{m}$  may be more favorable, provided the emissivity of the surface has favorable values in these areas.

In practice, a well calibrated infrared pyrometer can only account for some of these errors. In the context of surveying possible sites for power harvesting, it is impossible to know or predict the surface and radiative characteristics of all possible surfaces. A good calibration for one surface

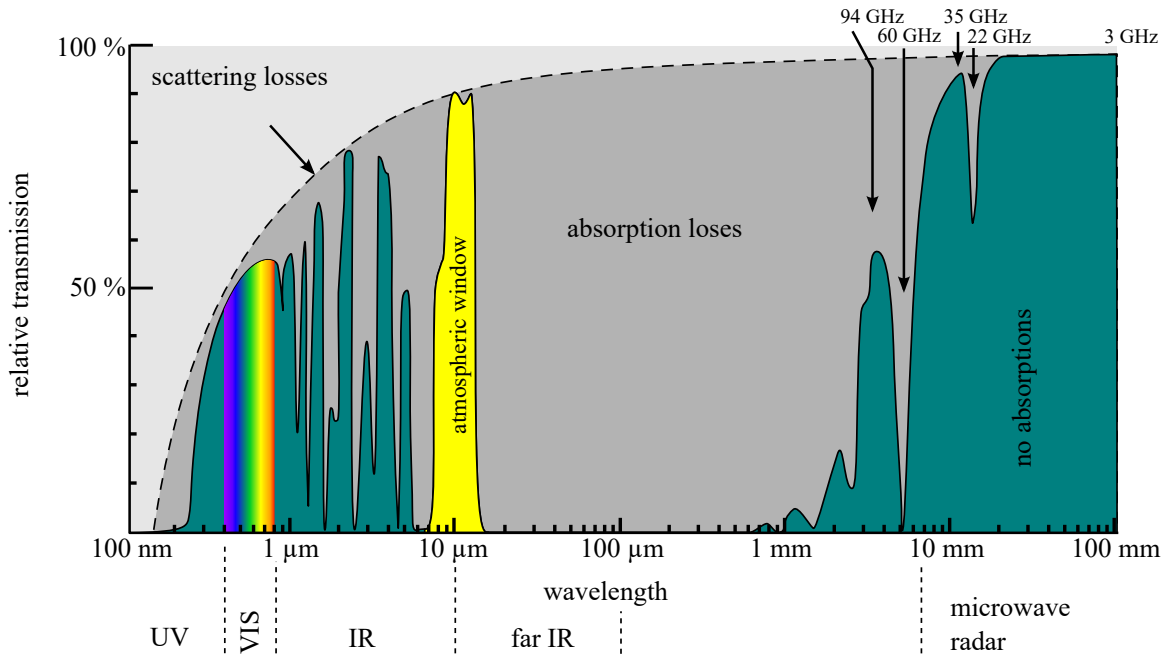


Figure 2.6: Chart illustrating the atmospheric participation in the form of relative transmission for a variety of wavelengths [17]

very likely may not work in another circumstance. In order to maximize accuracy obtained using infrared pyrometers, the following parameters should be carefully considered:

1. Use a two color pyrometer to minimize the impact of varying spectral emissivities
2. Choose a wavelength separation ( $\Delta\lambda$ ) that is not too close together
3. Choose pairs of frequencies to sample where the emissivities are similar while also being far apart so the emissivity ratio can be close to 1
4. Select a shorter wavelengths to help to minimize error
5. Select an wavelength where the atmospheric transmittance is high

Infrared pyrometers are a convenient tool for surveying a wide variety of surfaces in a short amount of time. Because of the nature of their function, inferences about surface characteristics can lead to error in temperature measurements. Realizing the limitations presented here can help guide engineers to not accept infrared readings at face value and use alternative measurement tools to validate the temperature of surfaces before further analysis. Thermocouples and resistance

temperature detector (RTDs), while less convenient and slower to setup, are more accurate in determining surface temperature. Using the IR pyrometer to determine ideal locations and performing a follow up measurement with a contact temperature probe will yield better, more consistent results for further analysis.

## CHAPTER 3. MATHEMATICAL MODELING

After taking a temperature measurement, the next step is determining the potential power output from a TEG based power harvester using the temperature data. This chapter illustrates the rationale and analytical approach behind the mathematical model that was created to characterize and predict the power output from a generic thermoelectric generator power harvester in the presence of a temperature difference.

### 3.1 Thermal Pathways

Thermal energy naturally flows from a high temperature source ( $T_s$ ) to a lower temperature environment sink ( $T_a$ ) (generally modeled as the low temperature thermal reservoir). A simplified model considers a single path from the source temperature to the ambient temperature through the thermoelectric generator, as seen in Figure 3.1. A more realistic diagram considers that the thermal energy can also bypass the thermoelectric generator. The thermal diagram for this situation can be seen in Figure 3.2. This situation considers that the temperature on the hot side of the thermoelectric generator ( $T_H$ ) will be decreased due to heat transfer to the surroundings as well as to the cold side of the TEG that occurs around the TEG. Ideally, the bypass heat transfer around the TEG will be minimized by making the bypass conductance ( $U_{bp}$ ) as small as possible so that it closely approximates the resistance diagram as seen in Figure 3.1.

The parameter,  $U$ , represents the thermal conductance to heat transfer. Thermal conductance is the inverse of thermal resistance to heat transfer, or  $U = 1/R_t$ <sup>1</sup>. The conductance through the system can be due to any form of heat transfer: conduction, convection, or radiation.

---

<sup>1</sup>Because thermal resistance to heat transfer is rarely used in the context of this work, it will be denoted by  $R_t$  so that  $R$  is reserved for electrical resistance



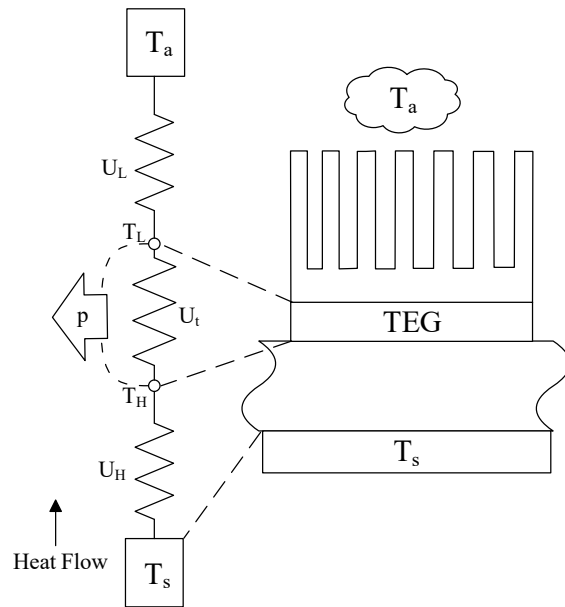


Figure 3.1: Thermal resistance diagram for a thermoelectric generator power harvesting system with resistances shown in conductances instead of resistances

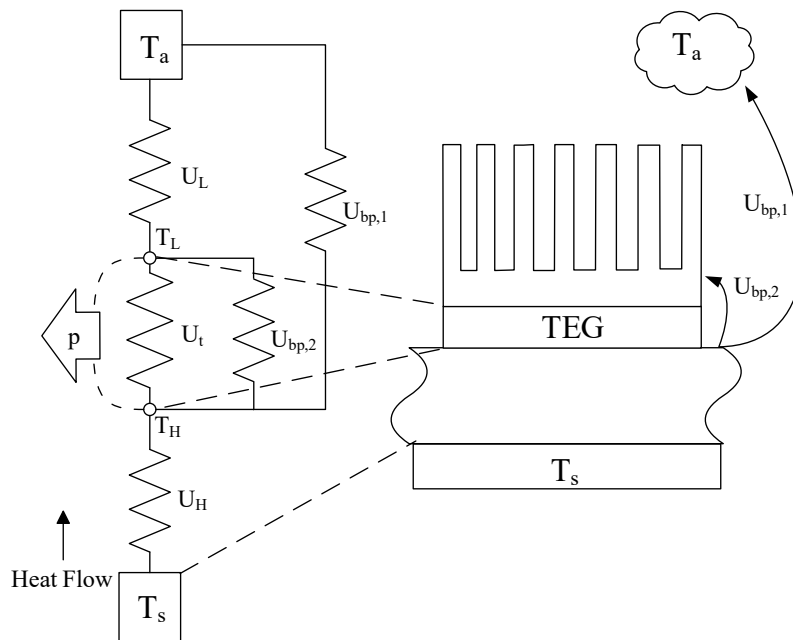


Figure 3.2: Thermal resistance diagram for a thermoelectric generator power harvesting system considering bypass heat transfer ( $U_{bp}$ ) with resistances shown in conductances instead of resistances

## 3.2 Thermal Pathway Modeling

In order to model the power output from the thermoelectric generator, internal electrical properties and heat generation as well as external heat transfer must be considered. Within the thermoelectric generator, internal effects such as Seebeck, Thomson, and Peltier effects occur, which affect the thermal and electrical balance within the TEG. This section will outline the approach of modeling the power output from the TEG while taking into account these internal effects.

### 3.2.1 External Heat Transfer Modeling

This section will outline the external thermal pathways and electrical effects around the TEG power harvesting system. The heat flowing through the thermoelectric generator can be characterized using the thermal diagram shown in Figure 3.2 and using Fourier's law. The external heat flow relationships for the cool side and the hot side can be seen in Equations 3.1 and 3.2, respectively. Notice how the heat through the hot side of the TEG (Equation 3.2) is diminished by the heat which bypasses the TEG.

$$q_L = U_L(T_L - T_a) \quad (3.1)$$

$$q_H = U_H(T_s - T_H) - U_{bp,1}(T_H - T_a) - U_{bp,2}(T_H - T_L) \quad (3.2)$$

Additionally, the electrical power created by the TEG can be characterized externally by the current produced and the load seen by the TEG (using Joule's Law, Equation 3.3).

$$p = I^2 R_{load} \quad (3.3)$$

### 3.2.2 Internal Heat Transfer Modeling

Internal heat transfer modeling requires consideration of the various physical effects which occur within the TEG (Peltier effect, Thomson effect, Seebeck effect and Joule heating). These effects manifest themselves in the form of thermal generation. This section will outline a series of equations which characterize these relationships.

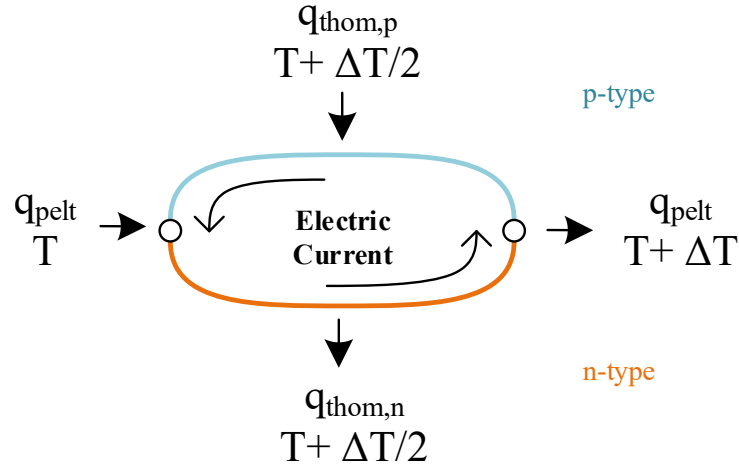


Figure 3.3: Internal diagram for Peltier and Thomson heat transfer within the wires of a p-type and n-type pair

Thomson and Peltier effects can be estimated by using the Seebeck coefficient. The Seebeck coefficient can be thought of as a voltage created per degree Kelvin. The Seebeck coefficient can be estimated as:

$$\alpha = \frac{\Delta V}{\Delta T} = \frac{dV}{dT} \quad (3.4)$$

Additionally, current through the TEG is partly a function of the Peltier and Thomson effects within the TEG. Equations 1.4 and 1.5 are used to characterize these effects. Because the Peltier and Thomson effects are approximately reversible processes [10], conservation of energy dictates electrical power produced by the circuit created of an n-type and p-type thermoelectric materials (seen in Figure 3.3) must equal the heat exchanged with the wires and the surrounding environment.

$$\begin{aligned}
 p &= \sum q \\
 I\Delta V &= q_{pelt,T+\Delta T} - q_{pelt,T} + q_{thom,n} - q_{thom,p} \\
 &= I\pi_o(T + \Delta T) - I\pi_o(T) + \tau_n I\Delta T - \tau_p I\Delta T
 \end{aligned} \quad (3.5)$$

Rearranging Equation 3.4 for  $\Delta V$ , substitution and dividing by  $I$  yields:

$$\begin{aligned}\frac{dV}{dT}\Delta T &= \pi_o(T + \Delta T) - \pi_o(T) + \tau_n\Delta T - \tau_p\Delta T \\ \frac{dV}{dT} &= \frac{d\pi_o}{dT} + \tau_n - \tau_p\end{aligned}\quad (3.6)$$

Because the Peltier and Thomson effects are approximately reversible, analyzing the system (Figure 3.3) using the second law of thermodynamics must be,

$$\sum_j \frac{q_j}{T_j} = 0 \quad (3.7)$$

Performing the second law analysis on the circuit in Figure 3.3 yields:

$$\begin{aligned}0 &= \frac{-q_{pelt,T+\Delta T}}{T + \Delta T} + \frac{q_{pelt,T}}{T} - \frac{q_{thom,n}}{T + \Delta T/2} + \frac{q_{thom,p}}{T + \Delta T/2} \\ &= \frac{-I\pi_o(T + \Delta T)}{T + \Delta T} + \frac{I\pi_o(T)}{T} - \frac{\tau_n\Delta T}{T + \Delta T/2} + \frac{\tau_p\Delta T}{T + \Delta T/2} \\ &= \frac{1}{\Delta T} \left( \frac{-\pi_o(T + \Delta T)}{T + \Delta T} + \frac{\pi_o(T)}{T} \right) - \left( \frac{\tau_n - \tau_p}{T + \Delta T/2} \right) \\ &= \frac{1}{\Delta T} \left( \frac{\pi_o(T + \Delta T)}{T + \Delta T} - \frac{\pi_o(T)}{T} \right) - \left( \frac{\tau_p - \tau_n}{T + \Delta T/2} \right)\end{aligned}\quad (3.8)$$

Assuming that  $\Delta T$  is small, and taking the limit of Equation 3.8 as  $\Delta T$  approaches 0:

$$\lim_{\Delta T \rightarrow 0} \left[ \frac{1}{\Delta T} \left( \frac{\pi_o(T + \Delta T)}{T + \Delta T} - \frac{\pi_o(T)}{T} \right) - \left( \frac{\tau_p - \tau_n}{T + \Delta T/2} \right) \right] = 0$$

$$\begin{aligned}\frac{d\left(\frac{\pi_o}{T}\right)}{dT} + \frac{\tau_n - \tau_p}{T} &= 0 \\ \frac{T \frac{d\pi_o}{dT} - \pi_o}{T^2} + \frac{\tau_n - \tau_p}{T} &= 0 \\ \frac{T \frac{d\pi_o}{dT} - \pi_o}{T} + \tau_n - \tau_p &= 0 \\ \frac{d\pi_o}{dT} + \tau_n - \tau_p &= \frac{\pi_o}{T}\end{aligned}\quad (3.9)$$

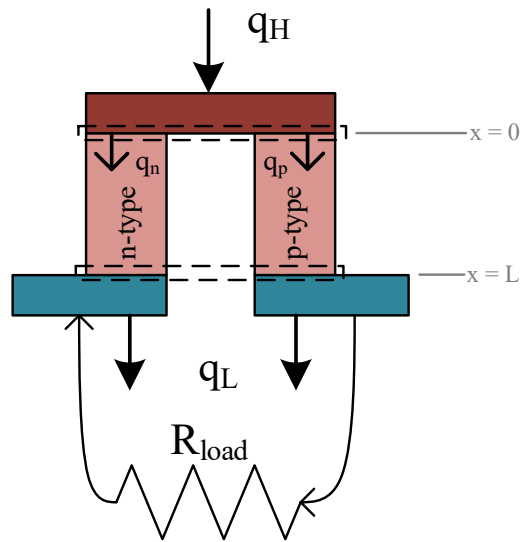


Figure 3.4: Internal diagram for a thermoelectric circuit pair with an n-type and p-type semiconductor thermally in parallel and electrically in series with two boundary surfaces labeled with a dashed line

Combining Equation 3.6 and 3.9

$$\begin{aligned}
 \frac{dV}{dT} &= \left( \frac{\pi_o}{T} + \tau_p - \tau_n \right) - \tau_p + \tau_n \\
 \frac{dV}{dT} &= \frac{\pi_o}{T} \\
 \alpha_o &= \frac{\pi_o}{T} \\
 \pi_o &= \alpha_o T
 \end{aligned} \tag{3.10}$$

Using this analysis, the Thomson effects are shown to be insignificant as they cancel out of the equation. Furthermore, solving for the Peltier coefficient yields an Equation (3.10) which relates the Peltier coefficient for a boundary to the Seebeck coefficients and the temperature of the boundary. Figure 3.4 defines two boundaries where these Peltier effects occur.

Performing an energy balance on the surface on the hot side of the TEG pair (see dashed boundary surface in Figure 3.4) is a balance between the heat entering the pair through the surface and what is leaving through each of the corresponding legs (i.e. p- and n-type legs).

$$q_H = q_{p,H} + q_{n,H} \quad (3.11)$$

The heat leaving the hot surface through the p-type and n-type legs are a combination of Peltier effects at the boundary as well as heat conducted from the surface:

$$q_{p,H} = q_{p,pelt} + q_{p,cond} \quad (3.12)$$

$$q_{n,H} = q_{n,pelt} + q_{n,cond} \quad (3.13)$$

Peltier effects were previously derived and can be obtained from using Equation 3.10 in Equation 1.4.

$$q_{peltier} = \alpha_o T_H I \quad (3.14)$$

Conducted heat transfer through the legs will be obtained using Fourier's law of heat conduction:

$$q_{p,H} = \alpha_p T_H I + \left( -k_p A_p \frac{dT}{dx} \Big|_{x=0} \right) \quad (3.15)$$

$$q_{n,H} = \alpha_n T_H I + \left( -k_n A_n \frac{dT}{dx} \Big|_{x=0} \right) \quad (3.16)$$

where  $k_p$  and  $k_n$  are the thermal conductivities of the p-type and n-type legs respectively while  $A_p$  and  $A_n$  are their respective cross-sectional areas. In order to find  $dT/dx$ , an energy balance on a differential element is needed.

$$\dot{E}_{in} - \dot{E}_{out} + \dot{E}_{gen} = \dot{E}_{st} \quad (3.17)$$

$$q_x - q_{x+\Delta x} + I^2 R = 0 \quad (3.18)$$

The electrical resistance of the TEG can be calculated using the concept of resistivity, or electrical resistance per unit length. That is,

$$R = \frac{\rho_e \Delta x}{A} \quad (3.19)$$

Substitution and further evaluation yields:

$$\begin{aligned} q_x - q_{x+\Delta x} &= -I^2 \left( \frac{\rho_e \Delta x}{A} \right) \\ \lim_{\Delta x \rightarrow 0} \left[ - \left( \frac{q_{x+\Delta x} - q_x}{\Delta x} \right) \right] &= - \frac{I^2 \rho_e}{A} \\ - \frac{dq_x}{dx} &= - \frac{I^2 \rho_e}{A} \\ - \frac{d}{dx} \left( -kA \frac{dT}{dx} \right) &= - \frac{I^2 \rho_e}{A} \\ \frac{d^2 T}{dx^2} &= - \frac{I^2 \rho_e}{kA^2} \end{aligned} \quad (3.20)$$

Integration yields,

$$\frac{dT}{dx} = \frac{-I^2 \rho_e}{kA^2} x + C \quad (3.21)$$

Separating and integrating Equation 3.21 from  $0 \rightarrow L$  and solving for the unknown constant of integration:

$$\begin{aligned} \int_{T_H}^{T_L} dT &= \int_0^L \left( \frac{-I^2 \rho_e}{kA^2} x + C \right) dx \\ &= \left( - \frac{I^2 \rho_e}{kA^2} x^2 + Cx \right) \Big|_0^L \\ T_L - T_H &= - \frac{I^2 \rho_e}{kA^2} L^2 + CL \\ C &= \frac{1}{2} \frac{I^2 \rho_e}{A^2 k} L - \frac{T_H - T_L}{L} \end{aligned} \quad (3.22)$$

Substituting the constant of integration (Equation 3.22) into Equation 3.21 yields an equation for  $dT/dx$ .

$$\frac{dT}{dx} = \frac{-I^2 \rho_e}{kA^2} x + \frac{1}{2} \frac{I^2 \rho_e}{A^2 k} L - \frac{T_H - T_L}{L} \quad (3.23)$$

Equation 3.23 can be used in Equations 3.15 and 3.16 when evaluated at  $x = 0$ .

$$\left. \frac{dT}{dx} \right|_{x=0} = \frac{1}{2} \frac{I^2 \rho_e}{A^2 k} L - \frac{T_H - T_L}{L} \quad (3.24)$$

Therefore (substituting into Equations 3.15 and 3.16),

$$q_{p,H} = \alpha_{o,p} T_H I - k_p A_p \left( \frac{1}{2} \frac{I^2 \rho_{e,p} L_p}{A_p^2 k_p} - \frac{T_H - T_L}{L_p} \right) \quad (3.25)$$

$$q_{n,H} = \alpha_{o,n} T_H I - k_n A_n \left( \frac{1}{2} \frac{I^2 \rho_{e,n} L_n}{A_n^2 k_n} - \frac{T_H - T_L}{L_n} \right) \quad (3.26)$$

Combining using the heat rates through the legs of the TEG yields an equation for  $q_H$ :

$$q_H = (\alpha_p + \alpha_n) T_H I - \frac{1}{2} I^2 \left( \frac{\rho_{e,p} L_p}{A_p} + \frac{\rho_{e,n} L_n}{A_n} \right) + \left( \frac{k_p A_p}{L_p} + \frac{k_n A_n}{L_n} \right) (T_H - T_L) \quad (3.27)$$

With the current form of the equation, the material properties ( $k$ ,  $\rho_e$ , etc.) are for individual materials in the thermoelectric generator. Simplifications can be made by substituting the overall TEG properties for internal thermoelectric material properties [10]. These overall properties are easier to measure in an experimental setting without knowing what the TEG is composed of internally. For the Seebeck coefficients, the effects for p- and n-type are opposite signs. For the overall effect, they will be added:

$$\alpha_o = \alpha_p + \alpha_n \quad (3.28)$$



For the internal electrical resistance of the TEG, the p- and n-type legs are electrically in series. Because they are in series, they can be added as well:

$$R_{int} = \frac{\rho_{e,p}L_p}{A_p} + \frac{\rho_{e,n}L_n}{A_n} \quad (3.29)$$

For the internal thermal conductance, the thermal resistances must be considered. In parallel, combining thermal resistances yields:

$$\begin{aligned} R_{t,t} &= \left[ \frac{1}{R_{t,p}} + \frac{1}{R_{t,n}} \right]^{-1} \\ &= \left[ \frac{k_p A_p}{L_p} + \frac{k_n A_n}{L_n} \right]^{-1} \end{aligned} \quad (3.30)$$

Therefore,

$$\begin{aligned} U_t &= \frac{1}{R_{t,t}} \\ &= \frac{k_p A_p}{L_p} + \frac{k_n A_n}{L_n} \end{aligned} \quad (3.31)$$

Substituting Equations 3.28, 3.29 and 3.31 yields an equation for the heat rate from the hot side of the TEG in terms of the internal characteristics.

$$q_H = U_t(T_H - T_L) + I\alpha_o T_H - \frac{1}{2}I^2 R_{int} \quad (3.32)$$

This same process can be followed for the cool side of the thermoelectric generator:

$$q_L = q_{p,L} + q_{n,L} \quad (3.33)$$

$$q_{p,L} = q_{p,pelt} + q_{p,cond} \quad (3.34)$$

$$q_{n,L} = q_{n,pelt} + q_{n,cond} \quad (3.35)$$

$$q_{p,L} = \alpha_p T_L I + \left( -k_p A_p \frac{dT}{dx} \Big|_{x=L} \right) \quad (3.36)$$

$$q_{n,L} = \alpha_n T_L I + \left( -k_n A_n \frac{dT}{dx} \Big|_{x=L} \right) \quad (3.37)$$

$$\frac{dT}{dx} \Big|_{x=L} = -\frac{1}{2} \frac{I^2 \rho}{A^2 k} L - \frac{T_H - T_L}{L} \quad (3.38)$$

$$q_{p,L} = \alpha_{o,p} T_L I + k_p A_p \left( \frac{1}{2} \frac{I^2 \rho_p L_p}{A_p^2 k_p} + \frac{T_H - T_L}{L_p} \right) \quad (3.39)$$

$$q_{n,L} = \alpha_{o,n} T_L I + k_n A_n \left( \frac{1}{2} \frac{I^2 \rho_n L_n}{A_n^2 k_n} + \frac{T_H - T_L}{L_n} \right) \quad (3.40)$$

$$q_L = U_t (T_H - T_L) + I \alpha_o T_L + \frac{1}{2} I^2 R_{int} \quad (3.41)$$

Equations 3.32 and 3.41 are partial characterizations of the heat flows within the power harvesting system.

It should be noted that Equations 3.32 and 3.41 are the same as those proposed by Lee [10] and very similar to those proposed by Taylor [18]. These equations are different than the equations proposed by Bergman [15]. When solved, Bergman's equations show that the ideal load for maximum power generation is twice the internal resistance of the thermoelectric generator. It is universally accepted that the greatest power generation occurs when the internal resistance of the TEG is matched with the load through which the electrical power is dissipated [9, 10, 15].

With Equations 3.32 and 3.41, another equation for net work from the TEG with internal considerations can be created. This equation is created by taking an energy balance for the entire system. In other words, the net power out of the system must be equal to the difference of heat entering ( $q_H$ ) and leaving ( $q_L$ ) the system. In this equation (Equation 3.42), the internal heat

transfer conductance across the TEG cancels out.

$$\begin{aligned} p &= q_H - q_L \\ &= I\alpha_o(T_H - T_L) - I^2R_{int} \end{aligned} \quad (3.42)$$

To summarize, the power model developed in this section is a system of six equations:

$$q_L = U_L(T_L - T_a) \quad (3.1)$$

$$q_H = U_H(T_s - T_H) - U_{bp,1}(T_H - T_a) - U_{bp,2}(T_H - T_L) \quad (3.2)$$

$$p = I^2R_{load} \quad (3.3)$$

$$q_H = U_i(T_H - T_L) + I\alpha_oT_H - \frac{1}{2}I^2R_{int} \quad (3.32)$$

$$q_L = U_i(T_H - T_L) + I\alpha_oT_L + \frac{1}{2}I^2R_{int} \quad (3.41)$$

$$p = I\alpha_o(T_H - T_L) - I^2R_{int} \quad (3.42)$$

These equations must be solved to yield TEG power ( $p$ ), TEG electrical current ( $I$ ), system heat rates ( $q_L$  and  $q_H$ ), and TEG surface temperatures ( $T_L$  and  $T_H$ ).

### 3.3 Conductance Modeling

The previously developed system of equations contain conductances which characterize the heat flow within the power harvesting system. In order to accurately characterize the power harvesting system, the thermal conductances of the power harvesting system must determined. Changes in the conductances have the potential to change the power output of the power harvester. Even though these conductances will be different for every power harvester design, this section will develop the conductance models which will be used for this work.

#### 3.3.1 Hot Side Conductance ( $U_H$ )

In order to simply model the hot side conductance of the TEG, it will be represented as a plane wall. This is simply the conductance between the hot side of the TEG and the temperature

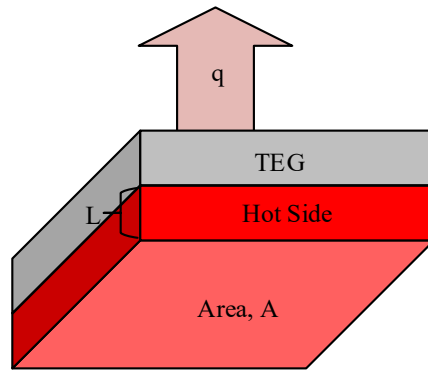


Figure 3.5: Diagram illustrating dimensions of definitions of hot side conductance parameters

of the source. The conductance is represented by Equation 3.43:

$$U_H = \frac{kA}{L} \quad (3.43)$$

The hot side conductance for the power harvesting system will be very high—especially when compared to the conductances elsewhere in the problem. This is due to the high thermal conductivity of the metal upon which the TEG is placed. The area represented in this equation is the surface area of one side of the TEG. These parameters can be seen in Figure 3.5

### 3.3.2 Cold Side Conductance ( $U_L$ )

In order to remove heat from the upper surface of the thermoelectric generator and reject it to the surroundings, an extended surface (e.g. heat sink) is sometimes used to improve the conductance in this area. Many heat sinks use an axial fan which blows impinging air downward onto the heat sink. Correlations for these heat sinks can be difficult to obtain, but work has been done in the area by Kim [19] and Wirtz [20] for very specific and specialized cases.

For ease in analysis, as well as being able to vary parameters to vary conductance, an array of rectangular fins is used. The derivation of the heat sink equation can be seen in Appendix G for

reference. Assuming an adiabatic tip condition<sup>2</sup>, the equation for heat rate through a single fin is:

$$q_f = \theta_b \sqrt{hPkA_c} \tanh(mb) \quad (3.44)$$

Defining fin efficiency as the ratio of the heat rate released from the fin to the heat rate released if the entire fin were at the maximum (base) temperature, or [15]:

$$\eta_f = \frac{\tanh(mb)}{mb} \quad (3.45)$$

The overall efficiency of a heat sink array is [15]

$$\eta_o = \frac{q_{array}}{q_{max}} \quad (3.46)$$

The total heat transfer through the fin will be

$$q_{total} = \eta_o h A_t \theta_b \quad (3.47)$$

where  $A_t$  is the total heat transfer area of the fin and  $n$  is the number of fins.  $A_t$  is further defined as,

$$A_t = n(A_f + A_w) \quad (3.48)$$

This area ( $A_t$ ) includes the fins as well as the exposed areas of the base. The total heat rate,  $q_{total}$ , is the sum of the heat transfer from the fins and the exposed base:

$$\begin{aligned} q_{total} &= n(q_f + q_b) \\ &= n(\eta_f h A_f \theta_b + h A_b \theta_b) \end{aligned} \quad (3.49)$$

---

<sup>2</sup>Selected because tips of the fins are a rounded profile. A metal plate is pressed against the tip. The round profile minimizes conduction to the plate and convection to the air in this configuration. This setup can be seen in Chapter 6.

Substituting the expression for the area of the base,  $A_b = \frac{A_t}{n} - A_f$ , yields,

$$\begin{aligned}
 q_{total} &= h\theta_b(n\eta_f A_f + A_t - nA_f) \\
 &= A_t h\theta_b \left( n\eta_f \frac{A_f}{A_t} + 1 - n\frac{A_f}{A_t} \right) \\
 &= A_t h\theta_b \left( 1 - n\frac{A_f}{A_t} (1 - \eta_f) \right)
 \end{aligned} \tag{3.50}$$

Therefore, using Equation 3.47, the overall heat sink array efficiency is

$$\eta_o = 1 - n\frac{A_f}{A_t} (1 - \eta_f) \tag{3.51}$$

Additionally, the overall thermal resistance is:

$$R_{t,o} = \frac{1}{\eta_o h A_t} \tag{3.52}$$

To find the conductance, Equation 3.52 is simply inverted:

$$U_{t,o} = \frac{1}{R_{t,o}} \tag{3.53}$$

The average convection coefficient,  $\bar{h}$ , is dependent on the properties of the fluid moving through the heat sink. Using the properties of the air and heat sink at a film temperature  $\left(T_f = \frac{T_w + T_a}{2}\right)$ , the average convection coefficient along the length of the heat sink can be approximated using the flat plate correlation for laminar flow [15]. This equation is:

$$\bar{h}_L = \frac{k_{air}}{L} 0.664 Re_L^{\frac{1}{2}} Pr^{\frac{1}{3}} \tag{3.54}$$

where,

$$Re_L = \frac{u_{air} L}{\nu_{air}}$$

This sequence can be used to find the thermal conductance  $U_L$  of the heat sink. These equations, in code, can be found in Appendix A.4.

### 3.3.3 Contact Resistance

In a composite system, the interface between objects can cause a temperature drop across the boundary instead of just through the object. Contact resistance can be significant at times. The resistance of an interface must be determined experimentally and is compiled in tables in the form of a thermal resistance over a unit area ( $m^2K/W$ ). These values are for specific sets of circumstances, such as materials, interface pressure, interfacial fluids, surface roughnesses. In general, contact resistance can be reduced (as well as temperature drop across the interface) by increasing the interface pressure and making the materials smoother at the interface. By default, the interfacial fluid is air which has a low thermal conductivity. Replacing the interfacial fluid with a fluid with a higher thermal conductivity such as zinc oxide, grease, or an ideal gas can reduce the contact resistance.

This research will assume the contact resistance between TEG and the surfaces it touches is negligible when compared to other assumptions which have been made in this work.

### 3.3.4 Bypass Conductance ( $U_{bp}$ )

This section will outline estimations of the bypass conductance. While this can vary widely depending on individual cases, the main goal is to estimate the order of magnitude of the bypass conductance and determine the significance. Bypass heat transfer occurs as one of two modes: convection or radiation.

Generic radiative heat transfer between two surfaces can be defined as:

$$\begin{aligned}
 q_{rad, bp} &= U_{bp, rad}(T_1 - T_2) \\
 &= \left( \frac{1}{\frac{1-\varepsilon_1}{\varepsilon_1 A_1} + \frac{1}{A_1 F_{12}} + \frac{1-\varepsilon_2}{\varepsilon_2 A_2}} \right) \sigma (T_1^4 - T_2^4) \\
 &= \left[ \left( \frac{1}{\frac{1-\varepsilon_1}{\varepsilon_1 A_1} + \frac{1}{A_1 F_{12}} + \frac{1-\varepsilon_2}{\varepsilon_2 A_2}} \right) \sigma (T_1 + T_2) (T_1^2 + T_2^2) \right] (T_1 - T_2)
 \end{aligned}$$

Where  $F_{1 \rightarrow 2}$  is the radiative shape factor from surface 1 to surface 2. Therefore,

$$U_{bp,rad} = \left( \frac{1}{\frac{1-\varepsilon_1}{\varepsilon_1 A_1} + \frac{1}{A_1 F_{12}} + \frac{1-\varepsilon_2}{\varepsilon_2 A_2}} \right) \sigma (T_1 + T_2) (T_1^2 + T_2^2) \quad (3.55)$$

Similarly, for generic convective heat transfer,

$$q_{bp,conv} = U_{bp,conv} (T_1 - T_2) \quad (3.56)$$

$$U_{bp,conv} = hA \quad (3.57)$$

The convection coefficient,  $h$ , must be determined based on the physical characteristics of the system. For this purpose, *Fundamentals of Heat and Mass Transfer* by Bergman [15] is used to obtain convection correlations.

The overall bypass conductance can be found by adding the conductances of both modes of heat transfer:

$$U_{bp} = U_{bp,rad} + U_{bp,conv} \quad (3.58)$$

### Hot Side - Ambient Bypass Conductance ( $U_{bp,1}$ )

From the hot side to the ambient, the bypass heat transfer occurs as a horizontal, flat plate with free convection (hot surface up) combined with radiative heat transfer.

In order to determine the convection coefficient for free convection, the Raleigh number must be calculated. This is defined as:

$$Ra_L = \frac{g\beta(T_s - T_\infty)L^3}{\nu\alpha} \quad (3.59)$$

For horizontal free convection,  $L = L_c$  where:

$$L_c \equiv \frac{A_{surface}}{P_{surface}} \quad (3.60)$$



The Nusselt number correlation for hot side up (and also  $\dot{h}$ ) is:

$$\overline{Nu}_L = 0.54Ra_L^{1/4} \quad (3.61)$$

$$\bar{h} = \frac{k}{L_c} 0.54Ra_L^{1/4} \quad (3.62)$$

For hot side down, the correlation is similar:

$$\overline{Nu}_L = 0.52Ra_L^{1/5} \quad (3.63)$$

$$\bar{h} = \frac{k}{L_c} 0.52Ra_L^{1/5} \quad (3.64)$$

The hot side down is necessary for installation in other orientations. Equation 3.57 can be used along with the convection coefficients to find the bypass conductance related to convection.

For the radiative bypass heat transfer, the hot surface is a real surface while the surroundings are considered a black body ( $\epsilon_{surr} = 1$ ). This makes the bypass conductance for the radiation, in this case:

$$U_{bp,rad,1} = \left( \frac{1}{\frac{1-\epsilon_H}{\epsilon_H A_H} + \frac{1}{A_H F_{H \rightarrow surr}}} \right) \sigma (T_H + T_{surr}) (T_H^2 + T_{surr}^2) \quad (3.65)$$

$$(3.66)$$

The view factor from the hot side to the surroundings is found using  $F_{H \rightarrow surr} = 1 - F_{H \rightarrow L}$  as any radiation not reaching the cold side of the system must be reaching the surroundings. Substitution yields the expression for  $U_{bp,rad,1}$ ,

$$U_{bp,rad,1} = \left( \frac{1}{\frac{1-\epsilon_H}{\epsilon_H A_H} + \frac{1}{A_H (1-F_{H \rightarrow L})}} \right) \sigma (T_H + T_{surr}) (T_H^2 + T_{surr}^2) \quad (3.67)$$

The view factor,  $F_{H \rightarrow L}$ , is developed in the following section as apart of  $U_{bp,2}$ .

### Hot Side - Cold Side Bypass Conductance ( $U_{bp,2}$ )

The radiative heat transfer portion of the  $U_{bp,2}$  is similar to that of  $U_{bp,1}$ , except from the hot side to the cold side of the system.

$$U_{bp,rad,2} = \left( \frac{1}{\frac{1-\varepsilon_H}{\varepsilon_H A_H} + \frac{1}{A_H F_{H \rightarrow L}} + \frac{1-\varepsilon_L}{\varepsilon_L A_L}} \right) \sigma (T_H + T_L) (T_H^2 + T_L^2) \quad (3.68)$$

The view factor (from hot side to cold side) can be calculated by using a Monte Carlo ray tracing simulation for the specific situation. An example of this can be seen in Figure 3.6. This figure is from a program written by the author using C++ and OpenGL. A pseudocode approach for this program can be seen in Appendix H. If the red plate in Figure 3.6 becomes very small, the view factor ( $F_{H \rightarrow L}$ ) goes to 0.5. As the area decreases, the bypass resistance becomes very small. That is,

$$\lim_{F_{H \rightarrow L} \rightarrow 0.5, A_H \rightarrow 0} \left[ \left( \frac{1}{\frac{1-\varepsilon_H}{\varepsilon_H A_H} + \frac{1}{A_H F_{H \rightarrow L}} + \frac{1-\varepsilon_L}{\varepsilon_L A_L}} \right) \sigma (T_H + T_L) (T_H^2 + T_L^2) \right] = 0 \quad (3.69)$$

This means that the bypass radiative resistance can be minimized by reducing the area of the base.

Convective heat transfer is characterized as hot air rising and blowing over the cold side of the TEG. As the heat sink represents the cold side of the TEG, the relevant 4 sides of a cuboidal shape will be approximated as 4 vertical plates. The Rayleigh number is the same as in Equation 3.59. The correlation for this conductance is [15]:

$$\overline{Nu}_L = 0.68 + \frac{0.67 Ra_L^{1/4}}{\left[ 1 + \left( \frac{0.492}{Pr} \right)^{9/16} \right]^{4/9}} \quad (3.70)$$

$$\bar{h} = \frac{k}{L} \left[ 0.68 + \frac{0.67 Ra_L^{1/4}}{\left[ 1 + \left( \frac{0.492}{Pr} \right)^{9/16} \right]^{4/9}} \right] \quad (3.71)$$

Same as previous, Equation 3.57 can be used along with the convection coefficients to find the bypass conductance related to convection.

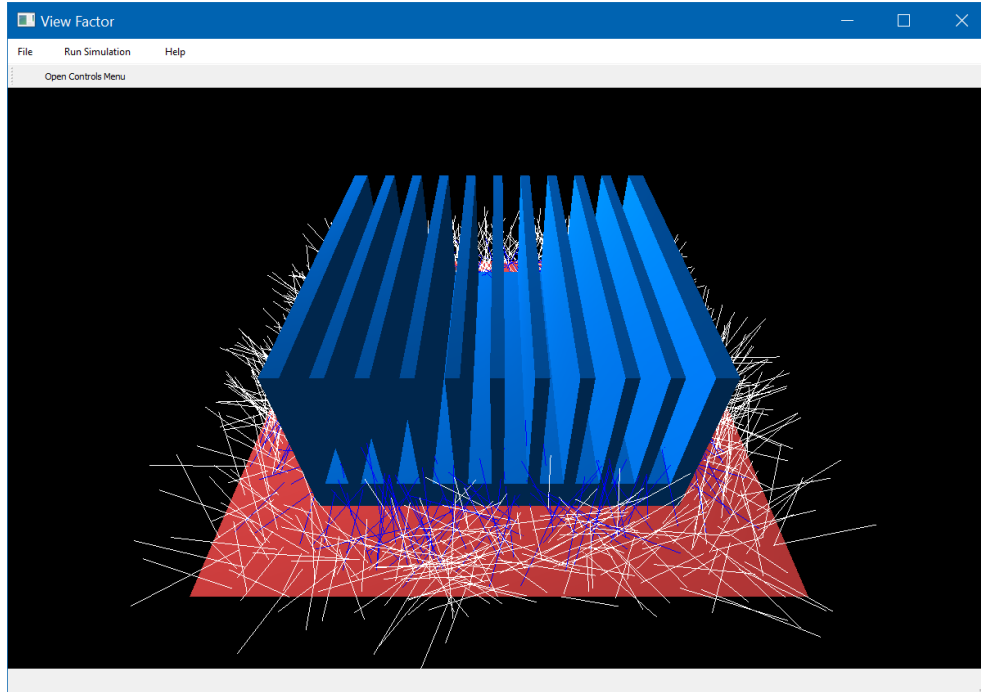


Figure 3.6: Screen capture from Monte Carlo ray tracing simulation program of models used to estimate view factor with 1000 rays drawn

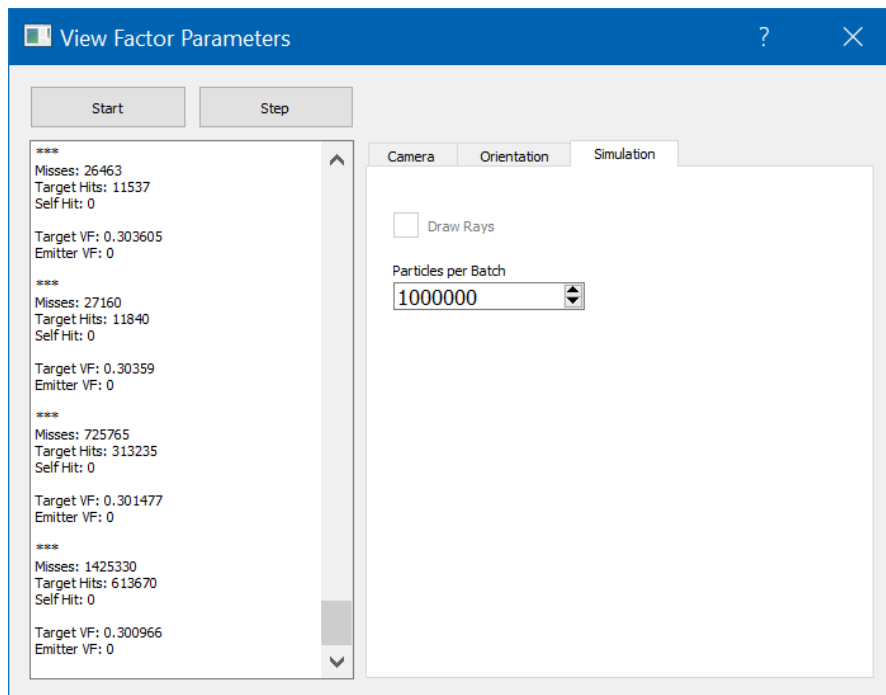


Figure 3.7: Screen capture from Monte Carlo ray tracing simulation program used to estimate view factor with results

This chapter created equations which govern the power output, current, TEG surface temperatures and heat rate through a power harvester system. This was done so in terms of conductances, temperatures, and TEG properties. While conductance values can change in various circumstances, the conductances for this work were developed in a general sense. This process can be adapted for specific circumstances if they vary from those in this work.

## CHAPTER 4. ECONOMIC ANALYSIS

It has been shown that power harvesting devices, such as thermoelectric generators, have the potential to create usable electricity from otherwise unused waste heat. While these systems are a good idea in theory, in real practice, economics will determine the viability of the system. If a system is too expensive or produces too little power, a system may not be worthwhile to install. In addition to paying for itself, the system must be able to pay for itself at a faster rate than the what could be earned elsewhere (i.e. the financial market). This section covers the basic economic principles in deciding the economic feasibility of a thermoelectric generator power harvesting system.

### 4.1 Initial Investment

For this work, initial investment will be defined as the total cost of implementing a power harvesting system. That is,

$$C_{initial} = C_{base} + N_{TEG}C_{TEG}(N_{TEG}) \quad (4.1)$$

In Equation 4.1,  $C_{base}$  is the flat cost of all supporting parts of the power harvesting system (i.e. non-TEG parts) as well as the installation cost. The cost of the individual TEGs is accounted for the second half of the equation as this scales with the quantity of TEGs required ( $N_{TEG}$ ). The unit cost of the thermoelectric generator can be variable depending on the number of TEGs that are purchased. This makes the cost of the TEG,  $C_{TEG}$ , a function the quantity of TEGs installed in the system.

## 4.2 Back Work and Net Work

In order to produce electricity, a thermoelectric generator must maintain a temperature differential across the device. This is because heat only flows when there is a temperature difference. Often, maintaining this temperature difference across the TEG requires a fan, pump or other device to remove the heat from the system. These devices improve the heat rate through the entire system, but require input power. In this case, power input is used to get increased power out of the system. This input power is referred to as back work,  $p_{back}$ . Because this power is put into the system in order to get power out, it must be subtracted from the gross power produced by the TEG to get net power. The net work ( $p_{net}$ ) from the system can be characterized by the difference in gross work and back work from the system:

$$P_{net} = P_{gross} - P_{back} \quad (4.2)$$

This equation will be used later in the economic analysis to determine net work from the TEG.

## 4.3 Net Inflow

When the thermoelectric generator produces power in the form of electricity, the net power has value. This value comes from the fact that the electric company sells electrical power at dollars per kilowatt-hour. In order to convert net power from the TEG to monetary units, the net power is multiplied by the unit price for the electricity. This is used as a basis for the revenue in the economic analysis. Net inflow is therefore the monetary savings after other costs such as maintenance. This is represented in Equation 4.3 and in a unit analysis in Equation 4.4.

$$C_{net} = p_{net} \cdot C_{elec} - C_{maint} \quad (4.3)$$

$$\left[ \frac{\$}{\text{period}} \right] = [\text{Watt}] \cdot \left[ \frac{\$}{\text{Watt-period}} \right] - \left[ \frac{\$}{\text{period}} \right] \quad (4.4)$$

where,  $C_{net}$  is the net inflow per period,  $C_{elec}$  is the cost of electricity per kWh, and  $C_{maint}$  is the maintenance cost.

#### 4.4 Simple Payback Analysis

For a quick analysis, a simple payback analysis can be used. A simple payback analysis simply divides the initial investment (installation costs) by the net inflow per period. This yields the payback period which can be seen in Equation 4.5:

$$\Gamma_{simple} = \frac{C_{initial} [\text{\$}]}{C_{net} [\text{\$/period}]} \quad (4.5)$$

where,  $\Gamma_{simple}$  is the simple payback period. This period can be in any reasonable unit of time (e.g. months or years).

This equation assumes that each month, the net inflow is the same. This may not be realistic if the maintenance costs are spread out further than the base period (e.g. the payback period is calculated monthly but maintenance is done yearly). If this is the case, the process must be done in an iterative, cumulative fashion. Net inflows must be tabulated by period and added to a cumulative net inflow. When the cumulative net inflow becomes positive, the system has been “paid off”. With the tabulated results the payback period can be calculated using the last period which had a negative cumulative inflow and the absolute value of the cumulative inflow for that period divided by the total cash inflow. More simply, this can be seen in Equation 4.6.

$$\Gamma_{simple} = x_s + \frac{|y_s|}{z_s} \quad (4.6)$$

where,

$x_s$  = last period with negative cumulative inflow (period  $n$ )

$y_s$  = cumulative inflow at end of period  $n$

$z_s$  = net inflow during period  $n+1$

Equation 4.6 will yield a value for the payback period which is between period  $n$  and  $n+1$ . This analysis can be seen in Section 7.5.1.

While the simple payback method is easy to calculate due to its linearity, it has a distinct disadvantage because it does not account for the time value of money (TVM). The principles of

TVM account for the possible interest gained in other investments as well as the inflation rate of the economy. Because of this, the simple payback period analysis alone is not suitable for robust engineering calculations and decision making. The simple payback period must be adjusted to obtain the the discounted payback period.

#### 4.5 Discounted Payback Period

A discounted payback analysis overcomes the major shortcoming of the simple payback period by accounting for economic growth. This leads to a more accurate result over long time periods.

The discounted analysis is similar to the simple payback analysis. The only change is instead of using “raw” inflow, the inflow is adjusted using a discount rate ( $i$ ) and the number of periods in the future ( $n$ ). This is referred to as the discounted inflow. This can be seen in Equation 4.7 or 4.8. The discount rate,  $i$ , is often determined based on the rate of return on other investments, such as the stock and bond markets.

$$C_{net,disc} = \frac{C_{net,simple}}{(1+i)^n} \quad (4.7)$$

$$= \frac{P_{net} \cdot C_{elec} - C_{maint}}{(1+i)^n} \quad (4.8)$$

Because the discounted net inflow varies with respect to each individual period, the same iterative, cumulative approach as was used in the simple payback analysis must be used. Instead of net inflow being calculated and used directly, it is converted to discounted net inflow. This is then added to the discounted cumulative net inflow until a positive number is reached (or a long amount of time has passed in order to guard against scenarios where payback is impossible).

The final discounted payback period methodology is the same as the final simple payback period methodology but the discounted inflow is used. This can be seen in Equation 4.9.

$$\Gamma_{disc} = x_d + \frac{|y_d|}{z_d} \quad (4.9)$$



where,

$x_d$  = last period with negative cumulative discounted inflow (period  $n$ )

$y_d$  = discounted cumulative inflow at end of period  $n$

$z_d$  = discounted net inflow during period  $n+1$

Again, this analysis can be seen in Section 7.5.1.

The economic model which was developed in this chapter can be used to determine how long a system's return on investment will be. A system that takes too long to return a profit will not be beneficial to install. Therefore, this must be considered in addition to the power model which was developed in the previous chapter.

## CHAPTER 5. OPTIMIZATION APPROACH

This chapter deals primarily with the technique employed in implementing the mathematical model developed in chapter 3 and the economic model developed in chapter 4. Specifically, this chapter discusses the solution method for the equations which govern the behavior of the thermoelectric generator and the system level optimization using a genetic algorithm. Using the optimization approach, the best possible design can more easily be discovered.

### 5.1 Power Output Solution

In order to optimize the system with respect to the payback period, the power output must be calculated for the scenario in question. Section 3.2 proposed six coupled equations: 3.1, 3.2, 3.3, 3.32, 3.41, and 3.42. These equations are restated below for convenience.

$$q_L = U_L(T_L - T_a) \quad (3.1)$$

$$q_H = U_H(T_s - T_H) - U_{bp,1}(T_H - T_a) - U_{bp,2}(T_H - T_L) \quad (3.2)$$

$$p = I^2 R_{load} \quad (3.3)$$

$$q_H = U_t(T_H - T_L) + I\alpha_o T_H - \frac{1}{2}I^2 R_{int} \quad (3.32)$$

$$q_L = U_t(T_H - T_L) + I\alpha_o T_L + \frac{1}{2}I^2 R_{int} \quad (3.41)$$

$$p = I\alpha_o(T_H - T_L) - I^2 R_{int} \quad (3.42)$$

In these equations, several things are known based on the installation:  $T_a$ ,  $T_s$ ,  $R_{load}$ . Thermal pathway conductances ( $U_L$  and  $U_H$ ) can be estimated based on analysis in Section 3.3. The cold side conductance,  $U_L$ , is a function of the backwork power which is related to the air speed through a correlation that has been developed. The properties of the TEG are also known from the specification sheet or can be measured or calculated:  $R_{int}$ ,  $U_t$ ,  $\alpha_o$  (see Appendix C). The unknowns

are  $q_L$ ,  $q_H$ ,  $T_L$ ,  $T_H$ ,  $p$ , and  $I$ . Because there are 6 unknown variables, the above 6 equations are adequate for a solution.

These equations can be solved using any equation solver that is capable of solving nonlinear equations. For this purpose, the author has selected MATLAB's *fsolve*. The six equations were entered into a MATLAB function in residual form so that when a solution was found, the residual is very close to 0. This function can be seen in Appendix A.3 (Code A.5).

The solution to this subroutine returns all unknown variables but, most importantly, yields the power output from the thermoelectric generator,  $p$ , which is necessary for further analysis.

## 5.2 System Optimization

In order to determine the economic feasibility of a specific power harvesting scenario, the previous equations can be simultaneously solved and the payback period calculated. In this problem, there are several parameters which must be experimented with in order to find an ideal setup. This section will introduce these parameters and how they will be handled.

### 5.2.1 Backwork

For a certain amount of back work, the solution to the TEG model will return the amount of power created by the thermoelectric generator. Subtracting the back work from the power yields the net power produced. When the initial investment is known, this information (combined with the cost of electricity) can be used to calculate the payback period of the device.

However, it is difficult to choose the correct amount of back work needed. As the amount of back work increases, the fan speed also increases. A higher fan speed will cool the cold side of the TEG more, creating a larger temperature differential across the TEG, and therefore produce more gross power from the TEG. This increase in power comes at the expense of increased back work. The back work can be selected by the user based on how much wattage is supplied to the fan or pump. Because of the interaction between gross work from the TEG and back work, the ideal balance of back work must be selected so that the net power is maximized.

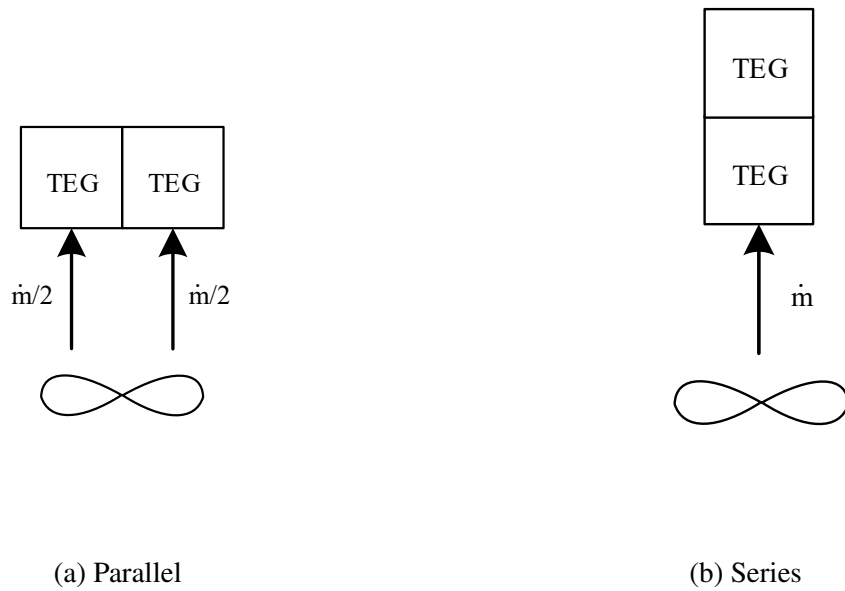


Figure 5.1: Diagrams for thermoelectric generators in series and in parallel with respect to air flow

### 5.2.2 TEG Arrangement

Further complexity is created when multiple TEG modules are considered. How the thermoelectric generators are installed will affect the amount of power they will produce. TEGs can be installed in parallel with respect to the air flow (i.e. air from fan blows through two or more TEGs at once) or in series (i.e. air from fan blows through TEGs sequentially). Illustrations of these two arrangements can be seen in Figure 5.1(a) and (b), respectively.

#### Parallel Arrangement

Installing the TEGs in parallel will split the mass flow rate from the fan between all TEGs in the system. Assuming incompressible fluid flow, this equates to halving the air speed delivered to the heat sink when 2 TEGs are placed in parallel. This also equates to  $1/3$  mass flow rate and  $1/4$  mass flow rate for 3 and 4 TEGs in parallel respectively. This creates an equal power output from each TEG in the system, at the expense of diminished cooling across the heat sinks due to

decreased velocity. The equation for total power output from an array of TEGs in parallel is simply,

$$P_{||} = N_{TEG}P_{ind,||} \quad (5.1)$$

where  $p_{ind,||}$  is the power produced an individual TEG calculated with the decreased air speed across the TEG.

### Series Arrangement

The problem of diminished air speed is partially overcome by installing the thermoelectric generators in series. While air speed is greater in this arrangement than the parallel arrangement, the air is heated as it goes through the heat sinks. Thermoelectric generators after the first TEG will see diminished conductance values due to the higher air temperatures.

This temperature increase can be modeled by considering a differential slice of air traveling through a heat sink. The energy balance for the differential slice of air is

$$\dot{m}c_p T_m(x) + \dot{q}_L(x) - \dot{m}C_p T_m(x + \Delta x) = 0 \quad (5.2)$$

Furthermore, because of the copper plate that is at the base of the heat sink, the base temperature of the heat sink can be considered to be isothermal where  $T_L$  is the base temperature. This means that the heat leaving the heat sink can be modeled as

$$\dot{q}_L = h(x) (T_L - T_m(x + \Delta x/2)) z_f \Delta x \quad (5.3)$$

where  $z_f$  is the width of the channel of the heat sink. Substituting Equation 5.3 into 5.2 and taking the limit as  $\Delta x$  goes to 0 yields:

$$\frac{dT_m(x)}{dx} = \frac{h(x)(T_L - T_m(x))z_f}{\dot{m}c_p} \quad (5.4)$$

Letting  $\theta = T_L - T_m(x)$  yields a differential equation:

$$\begin{aligned} \frac{d\theta}{dx} &= -\frac{h(x)\theta z_f}{\dot{m}c_p} \\ \int_{\theta(x=0)}^{\theta(x)} \frac{d\theta}{\theta} &= -\frac{z_f x}{\dot{m}c_p} \bar{h}_x \\ \ln\left(\frac{\theta}{\theta_o}\right) &= -\frac{z_f x}{\dot{m}c_p} \bar{h}_x \end{aligned} \quad (5.5)$$

This yields the solution for the temperature of the air along the channel as

$$\frac{T_L - T_m(x)}{T_L - T_a} = \exp\left(-\frac{z_f x}{\dot{m}c_p} \bar{h}_x\right) \quad (5.6)$$

Following this model, the temperature profile of the air within the heat sink is exponential in the  $x$  direction. Using the solution for  $\dot{q}_L$  along the heat sink (Equation 5.3), the heat rate through the thermoelectric generator decays in a similar manner with increasing mean air temperature. The heat rate through the TEG is directly related to the amount of power generated by the thermoelectric generator.

With this in mind, the diminished electricity generation by the TEG can be generalized by using an exponential decay formula on the power output from the TEG. The generalized approach has the benefit of not requiring significant iteration in order to solve for  $\bar{h}$ , since the average convection coefficient,  $\bar{h}$ , is a function of the final mean air temperature—also an unknown. The generalized solution also allows for conservative solutions so that any design will perform better than is predicted (see Appendix F). This approach yields the formula for the individual power output from any given TEG in a series:

$$P_{ind,series}(n) = \frac{P_1}{d} e^{\ln(d)n} \quad (5.7)$$

where  $n$  is index of TEG in system in order<sup>1</sup>,  $p_1$  is the power output from the first TEG, and  $d$  will be referred to as the reduction fraction. The reduction fraction is defined as the percent decrease

<sup>1</sup> $n = 1$  is first TEG in the series,  $n = 2$  is the second in the series, and so forth

Table 5.1: Individual power produced by TEGs as a fraction of the first TEG and the total power produced by a series of TEGs as a fraction of the first TEG

$n$	$\frac{P_{ind,series}(n)}{P_1}$	$\frac{P_{series}(n)}{P_1}$
1	1.00	1.00
2	0.80	1.80
3	0.64	2.44
4	0.51	2.95
5	0.41	3.36
6	0.33	3.69
7	0.26	3.95
8	0.21	4.16
9	0.17	4.33
10	0.13	4.46

from one TEG to the next TEG or:

$$d = \frac{P_{n+1}}{P_n} \quad (5.8)$$

This number will be between 0 and 1. In order to find the total output from an array of thermoelectric generators in series, the summation of the individual TEGs in the system is assumed:

$$P_{series}(N_{TEG}) = \sum_{n=1}^{N_{TEG}} \frac{P_1}{d} e^{\ln(d)n} \quad (5.9)$$

The series implementation will create a diminishing return for the addition of more TEGs to the system. This effect is illustrated in Table 5.1. With 10 TEGs in series, the 10th TEG only produces 13% of the power that the first one does. Furthermore, 7 TEGs only produce about 4 times the power of the first TEG. Without this diminishing return, the optimization algorithm would choose to add as many TEGs in series as possible in order to minimize the fraction of back work to the total gross power from the TEG.

The reduction fraction defined previously is determined experimentally in Appendix F.

### Both Series and Parallel Arrangement

A combination of both the series and parallel implementations can be done to balance the advantages and disadvantages of both methods. An example of this can be seen in Figure 5.2.

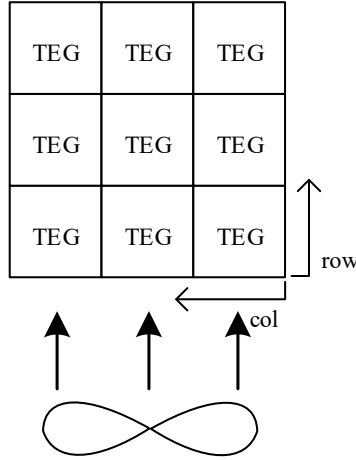


Figure 5.2: Array of TEGs in combination of parallel and series implementation

Calculating the power output from this method can be done by multiplying the total power output for TEGs in series (Equation 5.9) by the number of columns (TEGs in parallel). In Equation form, this can be seen in Equation 5.10 using nomenclature illustrated in Figure 5.2.

$$p(N_{row}, N_{col}) = \left( \sum_{n=1}^{N_{row}} \frac{p_1}{d} e^{\ln(d)n} \right) \cdot N_{col} \quad (5.10)$$

In this equation,  $p_1$  is the power output from a TEG in the first row. This can be calculated using the power model with the adjusted mass flow rate (diminished due to TEGs in parallel). This means that power output from an array of TEGs in this configuration can be characterized by the quantity of rows ( $N_{rows}$ ), columns ( $N_{cols}$ ) and, the power output ( $p$ ) from a TEG in the first row. This allows for optimization of the number of rows and columns in the optimization routine.

### 5.2.3 TEG Varieties and Cost

Further nonlinearity is added to the TEG optimization when bulk prices are considered. Some manufacturers offer lower prices per unit when a larger quantity of TEGs are purchased.



This will make it more advantageous to have more TEGs in the system. This is opposite of the diminishing return behavior shown by the series implementation.

Another factor accounted for in the optimization is variations in the variety of the TEG. High quality, high performing thermoelectric generators are available at higher cost. Additionally, lower performing TEGs are available at a lower cost. This adds another parameter that must be optimized (variety #1, variety #2, etc.) in order to find an optimal solution. Each one of these TEG varieties have a different specifications for  $R_{int}$ ,  $U_t$ ,  $\alpha_o$ , and TEG unit cost that will differentiate them from each other.

#### 5.2.4 Further Optimization Parameters

Further optimization could be done with changing to different types of fans, with their respective prices and fan speed correlation equations. This work will only consider a single fan model. Different fan geometry and motor designs will not adhere to the simple correlation (see Section 6.1.2). A more robust, all-encompassing model for air speed as a function of electrical power would be very involved and is outside of the scope of this work.

Similarly changing the heat sinks (either discrete different heat sink arrangements) or individual parameters could be further explored. The installed heat sink was based on a readily available heat sink. Varying the heat sink geometry may yield one that is more suited for this application. Doing so may be more expensive due to the need for a custom part. This will make the power harvesting system more expensive and, for this reason, a parametric heat sink model was not explored in this work.

### 5.3 Genetic Algorithm

Based on the discussion in the previous section, several integer system level parameters exist in the optimization problem—namely  $N_{col}$ ,  $N_{row}$ , and  $N_{TEG,type}$ . These must be an integer value due to the inability to have a partial TEG or the TEG must be one type or another. Because of this, the problem lends itself to a genetic optimization algorithm. Genetic algorithms are capable of handling integers because they create an initial population with several hundred possibilities and rank them against each other. These initial population values can be restricted to integer values and

other constraints as needed. Back work is another value that must be optimized to balance the trade off between  $U_L$  and  $p_{net}$ .

To summarize the optimization problem simply:

$$\begin{aligned} &\text{minimize: } \Gamma_{disc} \\ &\text{with respect to: } N_{col}, N_{row}, N_{TEG,type}, U_L(p_{back}) \end{aligned}$$

Where  $\Gamma_{disc}$  is the discounted payback period and is a function of the results of the TEG solving function (Appendix A.3). This TEG solving function is dependent on the heat sink function (Appendix A.4). Constraints can be imposed on the optimization such as limiting the number of TEG modules in a row or a column. A constraint is also placed on the range of the back work (e.g. minimum or maximum fan power) to avoid damaging the fan.

One downside of the genetic algorithm is that due to the probabilistic nature of genetic algorithms, the results are not repeatable 100% of the time. This is due to how they pseudorandomly come up with an initial population and then pseudorandomly generate a new population based on the previous ones. It does not find a solution continuously like gradient-based optimization techniques (such as MATLAB's *fsolve*). Additionally, the resulting solution can never be guaranteed to be the best solution, only one of the best solutions from the candidate set. This is not a significant issue with this analysis because there is a limited number of combinations for the number and type of thermoelectric generators. With a large enough initial population, these combinations can be exhausted so that the solver can quickly get to the ideal situation as well as ideal back work quantity. With this in mind, the solution yields a very similar answer every time it is run. With a larger catalog of TEG modules and the addition of a parametric heat sink model, the solution would rely more heavily on the probabilistic nature of the genetic algorithm. In order to be sure the solution is a valid solution, the model should be run more than once and the results compared to each other.

## 5.4 Optimization Overview

This section outlines high level pseudocode for the optimization approach. The list below begins with the main function (Code A.2) and steps through a high level sequence of code. The respective code snippets can be found in Appendix A.

1. Call parameter struct generation routine (To store and pass overall problem parameters between routines) (Appendix A.1)
  - (a) Generate parameter struct
  - (b) Return parameter struct
2. Run Genetic Algorithm optimization (MATLAB's *ga*) on payback solver
  - (a) Call payback solver routine, given  $N_{col}$ ,  $N_{row}$ ,  $N_{TEG,type}$ ,  $p_{back}$  and parameter struct (for penalty function) (Code A.3)
    - i. Call TEG function solver routine (solves of system of equations in Section 5.1 using parameter struct) (Code A.4)
      - A. Call fan correlation function (used to find air speed based on  $p_{backwork}$ ) which returns air speed (Code A.6)
      - B. Call heat sink function (using air speed) which returns  $U_L$  (Code A.7)
      - C. Use *fsolve* to solve TEG Functions with parameters specified in parameter struct (Code A.5)
      - D. Return results of solving system of equations
    - ii. Calculate net power from gross power and back work
    - iii. Iteratively calculate payback period using simple and discounted payback analysis
    - iv. Return payback period
  - (b) Return parameters for best payback period
3. Plot Payback Results
4. Output best case parameters

## CHAPTER 6. EXPERIMENTAL SETUP

Once the model was created to predict the power output from a source's surface temperature, two experiments were created to confirm the validity of the model (developed in Chapter 3). The first was to test the model and the effect of varying parameters on the power output of the TEG. The second was an installation on the air compressor as a proof of concept and to test the procedure.

### 6.1 Air Compressor Simulation Setup

As two of the objectives of this research is to identify locations for power harvesting and design a power harvesting system for air compressors, an air compressor in the lab was measured and surveyed for temperature using pyrometry. The readings from the pyrometer were confirmed using a thermocouple for reasons previously discussed in Chapter 2. A hot plate was used to simulate the conditions seen on the air compressor and remove some difficulties of working on an air compressor (such as irregular part fabrication and vibration).

The air compressor analyzed for this stage was a standard consumer grade air compressor model (Husky Model #C201H) capable of producing 150 PSI (approximately 1034 kPa). Over the top of the air compressor is a plastic barrier to shield the user from moving parts, such as fans, as well to shield from hot parts, such as the compressor block. Removing this shield exposes the large, metallic surface of the block, the compressor motor, and the cooling fan. This can be seen in Figure 6.1(a).

With the shield removed, the surface was imaged with an FLIR E50 infrared camera (a one color pyrometer) to get an idea of the warmest locations on the air compressor. Because the FLIR IR camera is proprietary, customizations for parameters (such as wavelength) is restricted. The pyrometer measures irradiation between the wavelengths of 7.5 to 13  $\mu\text{m}$  [21]. This is within the atmospheric window discussed in Chapter 2 which is beneficial for the pyrometer's readings. For

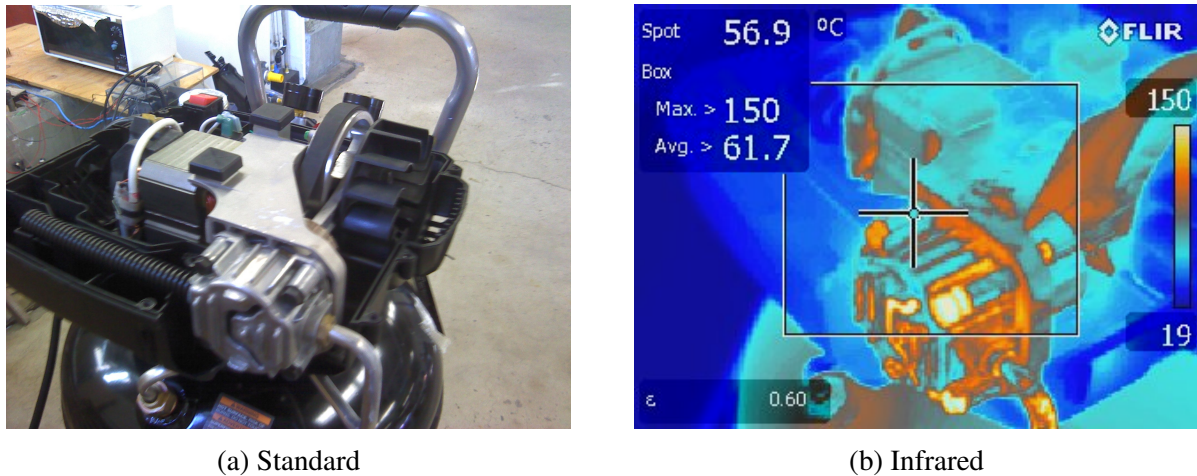


Figure 6.1: Standard and infrared images of air compressor with heat shield removed

one color pyrometers, an emissivity value must be selected to adjust for the discrepancy between apparent and actual surface temperatures. The emissivity value for the pyrometer was entered as 0.6 (a guess due to the cast aluminum surface [16]). This is likely to be incorrect as precisely knowing the emissivity of a surface is difficult.

With these limitations and approximations in mind, the image from this pyrometer can be seen in Figure 6.1(b). Based on this picture, the block exhibits wide temperature variations. The temperature of the surface was confirmed with a thermocouple due to the limitations of pyrometry discussed in Chapter 2. The thermocouple reading found that the temperature was more consistent than the pyrometer illustrated. The hot plate's temperature was set so that the surface the TEG would be mounted on was approximately the measured temperature of air compressor.

### 6.1.1 Thermal Measurements

Several temperature measurements were taken in the system. This system is composed of a variety of plates for temperature consistency. An aluminum heat spreader was placed onto the hot plate (SciLogex MS-H280 Pro) in order to spread the heat transfer evenly and minimize the potential hot spots on the hot plate (due to heating coils within the hot plate). Additionally, the aluminum heat spreader was polished smooth and flat so that heat transfer across the boundary was maximized.

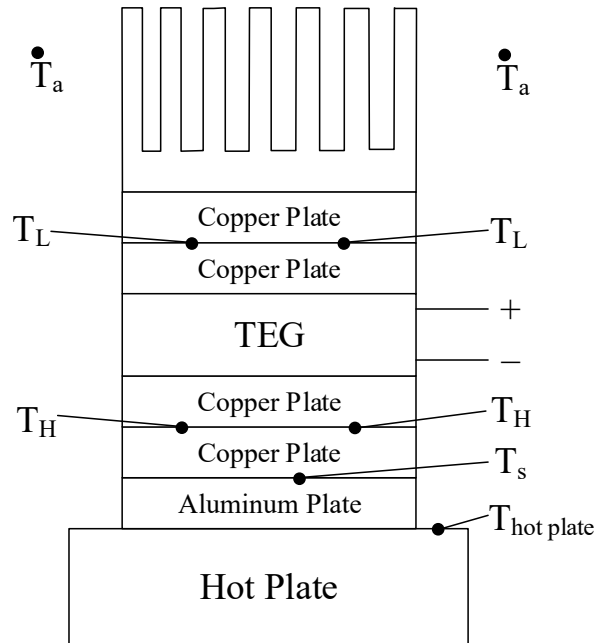


Figure 6.2: Diagram of experiment stack and temperature measurement locations (not to scale)

A set of copper plates were created in order to provide an isothermal surface for the TEG and provide for consistent temperature measurements. The plates were cut from 1/8 inch copper plate in dimensions 40 mm x 40 mm (the same dimensions of the TEGs which were used). Two plates were used for the each the top and the bottom of the thermoelectric generator. In one of the plates, a groove was machined into the copper plate with a 3/64 inch ball end mill in order to hold a thermocouple. When the two plates are placed together, the thermocouple is wedged within the groove. The groove was sufficiently deep so that complete contact between the upper and lower plates could occur while also allowing for good contact between the thermocouple bead and the copper pieces. These thermocouples (wedged within the copper plates) allowed for a reading of the hot side temperature of the TEG,  $T_H$ .

A thermoelectric generator was placed on top of copper plates. Additionally, another set of copper plates was placed on top of the thermoelectric generator in the same configuration as the bottom in order to monitor the temperature on top of the TEG,  $T_L$ . On top of the stack is a heat sink to dissipate the heat.

In between all of the pieces of the stack, a thin layer of silicon based zinc oxide thermal paste was placed before assembly to minimize contact resistance and aid in heat transfer. The assembly was clamped down with screws and an aluminum angle bar. This entire stack can be seen in Figure 6.3 as well as a diagram in Figure 6.2.

Because pyrometry can only measure surface temperatures, thermocouples were embedded to measure the internal temperatures throughout the experiment. In total, 8 thermocouples were used to measure temperatures of the system. Both  $T_L$  and  $T_H$  were measured in duplicate in order to confirm the isothermal assumption within the copper plates as previously stated. Ambient temperature was also measured from two locations due to inconsistent room temperatures within the lab. Using 2 locations near the experiment allowed for a better, more consistent average temperature to be calculated. These thermocouple locations (shown in Figure 6.2) are:

1. Hot Plate
2. Aluminum Heat Diffuser ( $T_s$ )
3. 2x Hot Side Copper Plate ( $T_H$ )
4. 2x Cold Side Copper Plate ( $T_L$ )
5. 2x Ambient Temperature ( $T_a$ )

These thermocouple measurements were taken using a NI cRIO 9074 chassis with a NI 9213 Thermocouple module. Thermocouples were made from J-type thermocouple wire. Thermocouple offsets were calibrated using the method outlined in Appendix B.

### 6.1.2 Air Speed Measurement

A blower fan was attached to the side of the heat sink using a 3D printed duct which clipped to the aluminum angle bar so that the air is blown across the heat sink. Also within the 3D printed duct, two access ports were added for installation of an anemometer probe for *in situ* air speed measurements. While two access ports for the anemometer were added for convenience, only one was used at a time while the other was plugged. This heat sink and air duct can be seen Figure 6.3 while a CAD image of the duct can be seen in Figure 6.4.



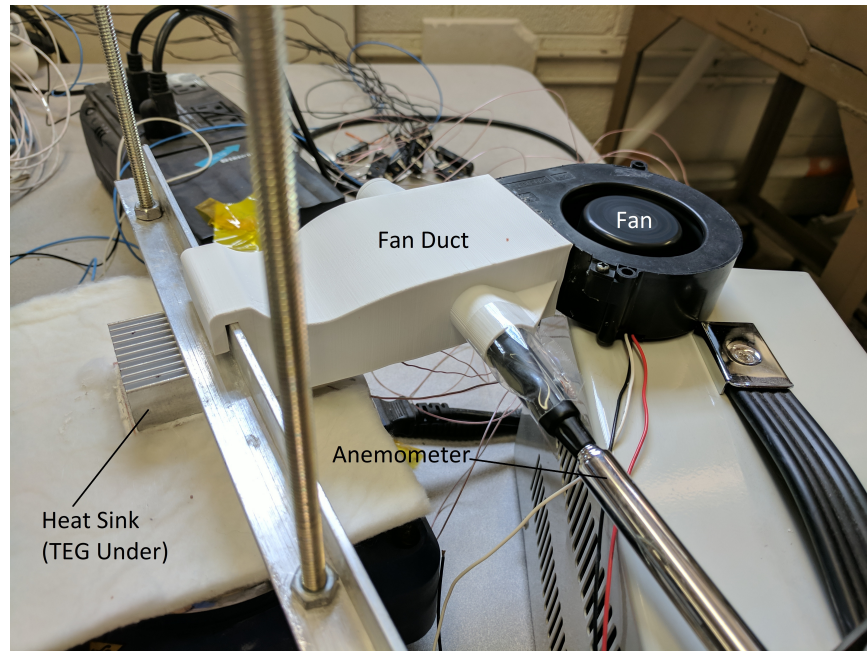


Figure 6.3: Experimental setup with rectangular fin array, blower fan, and anemometer

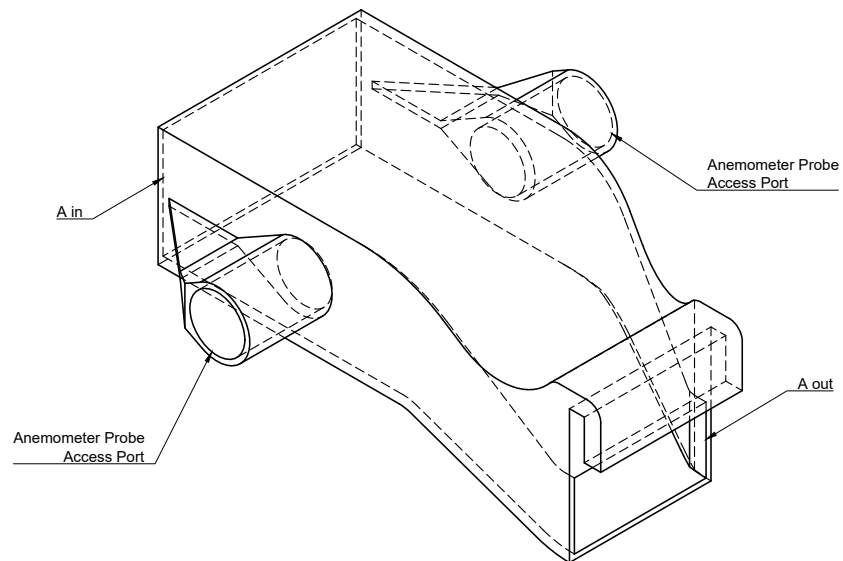


Figure 6.4: 3D model of fan duct used to change area of fan opening and install anemometer



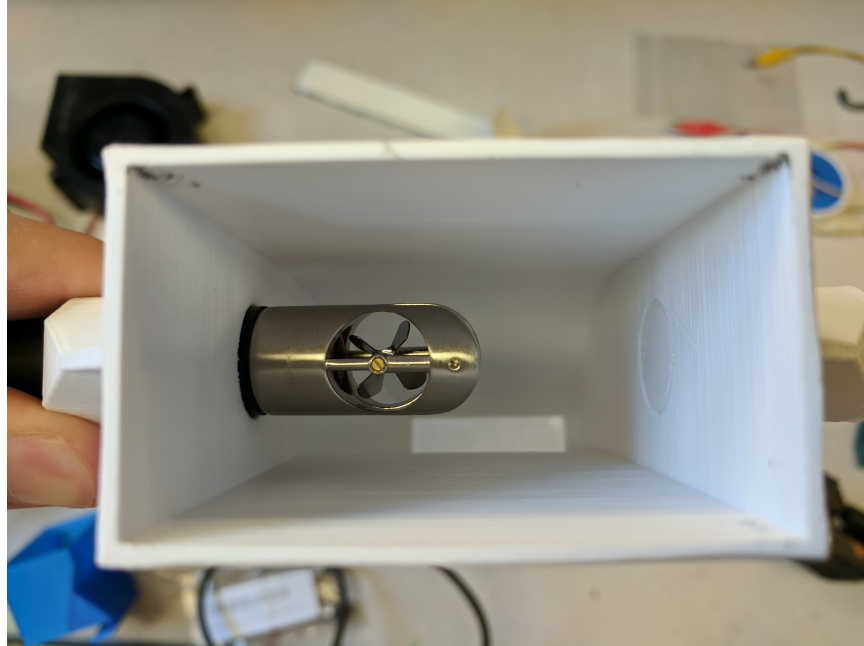


Figure 6.5: Anemometer installed in 3D printed duct attachment for blower fan speed measurement

Air speed across the heat sink varies with the power input to the fan. The air speed that is measured is at the inlet of the duct. Air speed is measured at the wider portion so that the anemometer restricts the flow less. Because of the reduction in the duct, the air speed as measured by the anemometer at the inlet will be slower than the air speed at the exit. The differences in air velocity can be calculated using the principle of conservation of mass. Because the air speed is low, the flow is considered incompressible and density remains the same at the inlet and the exit.

The equation for the relationship between entrance and exit air speeds is:

$$u_{out} = u_{in} \frac{A_{in}}{A_{out}} \quad (6.1)$$

Where  $A_{in}$  and  $u_{in}$  are the flow area and air speeds into the duct while  $A_{out}$  and  $u_{out}$  is the exit area and air speeds of the fan.

The air speed,  $u_{out}$ , is then used to calculate the convection coefficient needed in the analysis outlined in Section 3.3.2.

In order to easily calculate the air speed (and later convection coefficient and conductance values), a fan power-velocity correlation was created using empirical data. Using the plotted data,

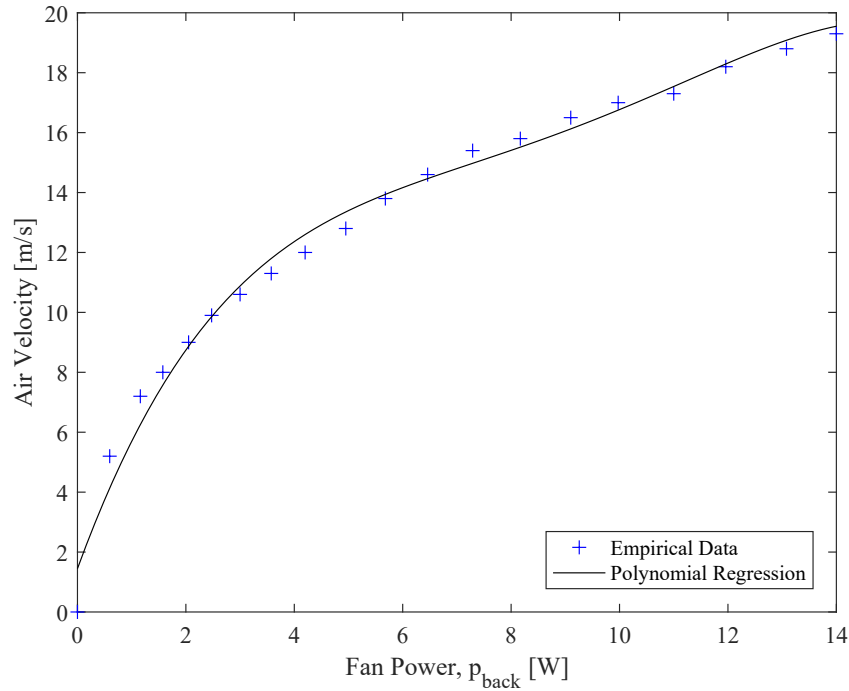


Figure 6.6: Fan correlation function created using a 4th order polynomial regression on empirical data in terms of back work ( $p_{back}$ )

a 4th order polynomial regression was generated to fit the data using MATLAB's *polyfit* function. The data and regression equation can be seen in Figure 6.6. The regression equation can be seen in Equation 6.2.

$$\begin{aligned}
 u_{out} = & -0.00155(p_{back})^4 + 0.05723(p_{back})^3 \\
 & - 0.75965(p_{back})^2 + 4.9506(p_{back}) + 1.44729
 \end{aligned} \tag{6.2}$$

### 6.1.3 Electrical Measurements

An electrical circuit (diagram seen in Figure 6.7) was constructed for making electrical measurements and connecting a resistive load to the thermoelectric generator. The thermoelectric generator is represented by the DC load in the diagram. Electrical measurements were taken with an NI 9209 voltage measurement module which was installed in the NI cRIO 9074 chassis. This module was used to take 2 analog voltage measurements: TEG voltage overall and voltage

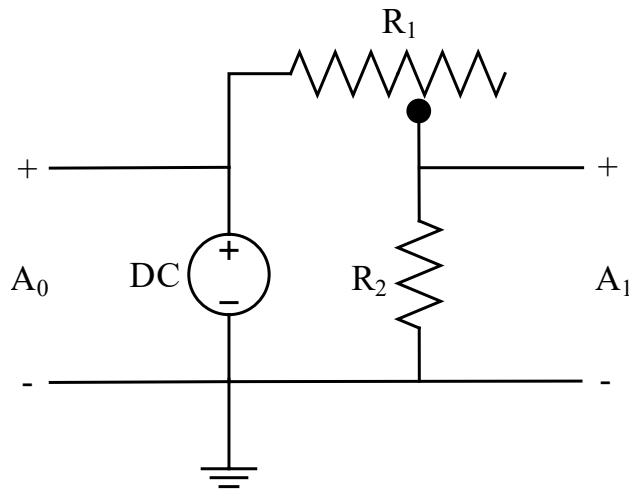


Figure 6.7: Wiring diagram for instrumentation measuring electrical power

drop across a current shunt. These measurements are represented in Figure 6.7 by  $A_0$  and  $A_1$ , respectively.

These voltage measurements are used to evaluate the performance of the TEG. The voltage generated across the thermoelectric generator can be used to calculate the power generated by the TEG. The current shunt is a piece of wire with a very small but documented resistance value. The shunt is rated at a 75 mV drop when 10 Amps are passed through it. Using Ohm's Law ( $V = IR$ ), finds that the electrical resistance through the shunt is  $0.0075\Omega$ . This shunt is represented in Figure 6.7 by resistor  $R_2$ . Using the measured voltage drop combined with the known resistance, current generated by the TEG can be calculated, using Ohm's Law:

$$I_{TEG} = \frac{V_{A2}}{R_2} \quad (6.3)$$

Furthermore, a resistive load ( $R_1$  in Figure 6.7) was added to dissipate the electric power from the thermoelectric generator. The specifics of this resistive load will be explained in the following section.

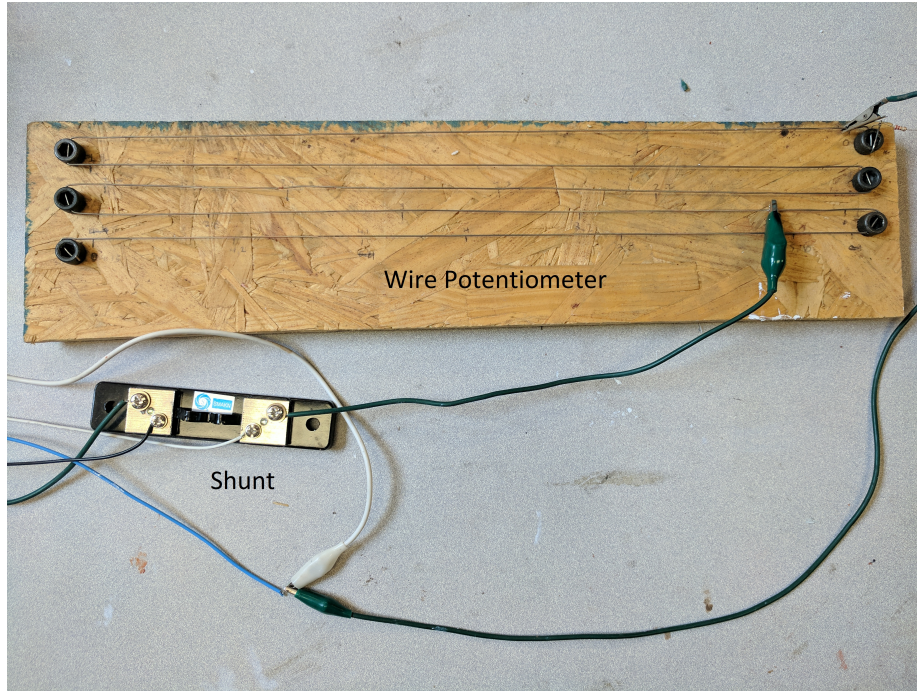


Figure 6.8: Resistive wire potentiometer (top) with current shunt (bottom) (for diagram, see Figure 6.7)

## 6.2 Matched Load Experiment

A matched load has been demonstrated by several sources as being the ideal case for power harvesting systems [9, 10, 15]. When the internal TEG electrical resistance is equivalent to the external resistive load through which the electric power is dissipated, the maximum amount of usable electrical power is produced. It is useful to confirm the validity of the model that was created by varying the resistive load and comparing the estimated power output to those measured experimentally.

Most potentiometers have fairly high resistances ( $100\Omega$  or more). Because thermoelectric generators have an internal resistance of less than  $10\Omega$ , a typical potentiometer is unable to provide these low resistive loads. A length of nickel-chromium resistance wire was bolted to a non-conductive surface (wood particle board) to create a custom potentiometer. With a resistance of approximately  $1\Omega/\text{ft}$ , about 8 feet of wire was used. An ohmmeter accurate for low resistances was used to calibrate the custom potentiometer and make markings for various resistance values. Alligator clips are used to make changes to the resistance of the circuit by clipping on to the middle of the resistive wire. This potentiometer can be seen in Figure 6.8.

In order to confirm the model that has been created, the resistive load was adjusted using the resistive wire potentiometer ( $R_1$  in Figure 6.7). This is done by moving the alligator clip along the wire to various locations where the electrical resistance is predetermined. When the potentiometer was adjusted, the system was allowed to come to thermal and electrical equilibrium before the data was collected. The results of this test can be seen in Section 7.5.

### 6.3 Thermal Pathways Experiment

Further validation of the model can be done by varying the conductance parameters of the power harvesting system. The easiest conductance parameter to vary is the conductance on the cold side of the thermoelectric generator,  $U_L$ . Because the hot-side conductance ( $U_H$ ) is through a highly conductive material and is fixed, it is not able to be easily changed without disassembly of the device. Additionally, changing  $U_L$  will have a large effect because it is small, relative to  $U_H$ . A change in  $U_L$  has the potential to significantly change  $T_L$ , while a change in  $U_H$  can not change as significantly because  $T_H$  and  $T_s$  are already very close in value (due to the high conductance of  $U_H$ ). More simply, the temperature drop across the cold side is much larger than that across the hot side.

Varying the conductance of the cold side is accomplished by changing the air speed blowing across the thermoelectric generator. This is done by changing the voltage into the blower fan which changes the fan's speed. This voltage-speed correlation was calculated using empirical data (see Section 6.1.2/Figure 6.6).

The results from this experiment and the matched load experiment will be discussed in Section 7.4

### 6.4 Installation on an Air Compressor

The goal of this work was to find high temperature regions and use the TEG power model to predict the power created if a power harvester were installed. In Chapter 1, air compressors were discussed as a large source of waste heat. In order to study air compressors as a heat source, the same air compressor as in Section 6.1 (Husky Model #C201H) was examined for high temperatures as well as accessibility of those high temperatures.

The air compressor was run for about 3 minutes. This was sufficient time for the temperatures to stabilize as well as for the air compressor tank to almost completely pressurize. The temperature measurements ceased to change after about 2 minutes.

The highest temperature (measured with a thermocouple) was found on top of the cylinder block, with temperature of between 190-210°C . While this area had a high temperature, there were several moving parts, as well as high vibrations in the vicinity. Those factors, combined with difficulty in securing the power harvesting apparatus, led to the conclusion that this area was too difficult to safely install a TEG without extensive modification of the cylinder block.

At the expense of a lower temperature, a different site was selected on the aluminum pipe containing the compressed air. The pipe connects the cylinder block to the tank on the air compressor. This pipe heats up due to the hot, compressed air leaving the cylinder block at up to 150 PSI (1034 kPa). This pipe reaches 150-165°C . This area is more accessible than the cylinder block and allows for more secure attachment of the power harvesting device. The pipe also offers the unforeseen benefit of dampening some of the vibrations from the air compressor motor and compressor.

Temperatures of these measured surfaces were consistent with the expected temperatures of the system. When analyzed with a polytropic process as discussed in Chapter 1, air compressed quickly to 1000 kPa is expected to reach about 225°C (see Figure 1.1). The compressor surface temperature will not be the same as the temperature of the hot air because heat flow requires a temperature difference. Because the air compressor is transferring heat to the surroundings, the temperature of the surface must be lower than the internal temperature of the air. This means the measured surface temperature is reasonable when compared with the air temperature predicted by a polytropic process.

Assembly of the system was very similar to the hot plate air compressor simulation experiment outlined in Section 6.1. Two mating pieces, each with a semi circular channel in them, were clamped around the circular tube. The tubing is 3/8-in, so the hole was reamed so that optimum contact and surface finish could be achieved. On top of this, a polished copper plate (40 mm x 40 mm x 1/8 in, same as used previously) was placed to act as a heat spreader. Next, the TEG and another copper plate was placed. Finally, the heat sink was placed onto the top of the stack (on the copper plate) and the entire stack was clamped down. Silicon zinc oxide thermal paste was spread



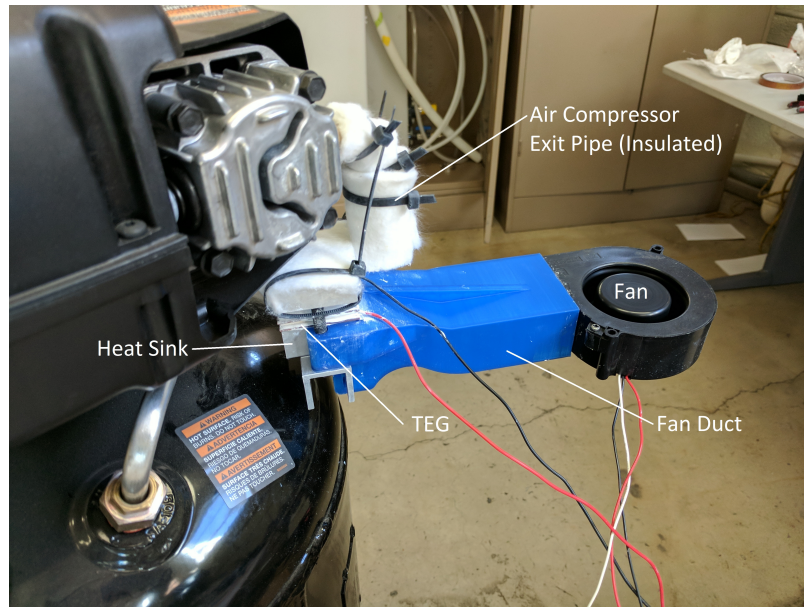


Figure 6.9: Power harvester installed on air compressor

thinly between all surfaces to aid in reducing contact resistance between parts. The CAD assembly can be seen in Figure 6.10, and a picture of the installed assembly can be seen in Figure 6.9. Additionally, an exploded assembly drawing can be seen in Figure D.1. Technical drawings for fabricated parts of this device along with an exploded assembly drawing are included in Appendix D.

Because 40 mm x 40 mm thermoelectric generators were used, a straight, 40 mm length of aluminum tubing was required for good surface contact. The only portion meeting this requirement was underneath the compressor unit. This left a length of tubing where heat was lost from the air within the tubing. In order to mitigate this heat loss, insulation was applied to the tubing. A Spaceloft blanket insulation manufactured by Aspen Aerogel was selected due to its low thermal conductivity (15 mW/m-K) [22]. Additionally, this installation location required that the heat sink be inverted, meaning a fan was required in order to achieve significant convection (e.g. no free convection). The effectiveness of this insulation can be seen with Figure 6.11.

The same power measurements were taken from the TEG as with previous experiments using the National Instruments data acquisition system. Because the goal of this experiment was to validate the model's effectiveness in a more realistic setting, no means of internal temperature measurements were implemented.

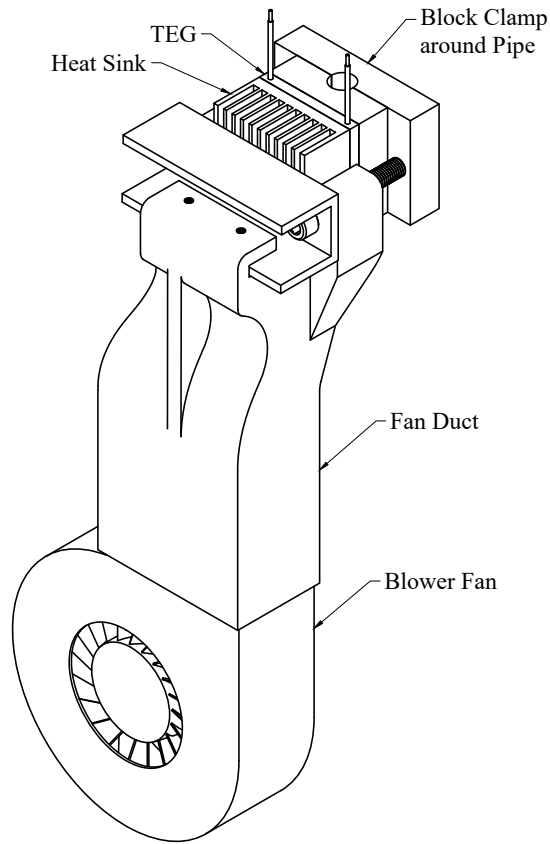


Figure 6.10: Isometric CAD drawing of power harvester design for air compressor experiment setup

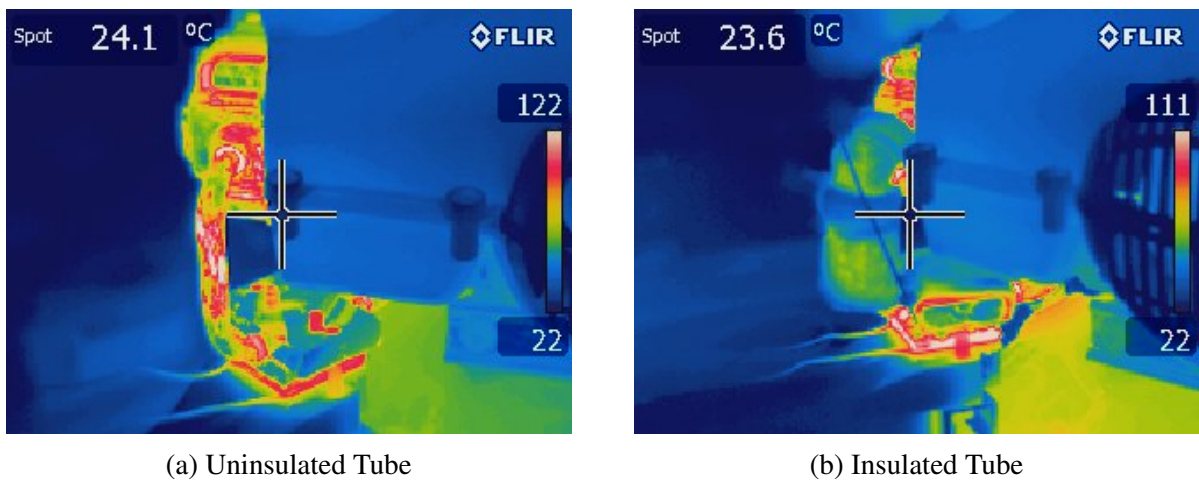


Figure 6.11: Infrared images of heat loss from of aluminum tubing leaving compressor for uninsulated (a) vs. insulated installations (b)



The results of this experiment can be seen in Section 7.4.1.

## CHAPTER 7. MODEL APPLICATION AND RESULTS

With experimental validation of the model, the model can be used to evaluate the validity of a power harvester design and also discover the optimum design of a power harvester under specific circumstances. This chapter will take measured and calculated parameters and apply them to the model which was developed in the previous chapters.

### 7.1 Propagation of Uncertainty

Measured values have an effect on both the model and the calculated measured values. Uncertainty is propagated for temperature, voltage, and resistance measurements.

#### 7.1.1 Model Uncertainty

In order to estimate the accuracy of the model, uncertainty of the measurements must be considered. Parameters for which the model is most sensitive as well as parameters which vary most significantly will affect the model's output. It was observed that several parameters had significant effects on the output of the model. The model was highly sensitive to the internal electrical resistance of the TEG ( $R_{int}$ ) as well as the overall Seebeck coefficient ( $\alpha_o$ ).

Several parameters did not seem to have a significant effect on the model. While matched loads are important overall, the model was not sensitive to small changes in resistive loads in the region around the ideal matched load. This is likely due to the global maximum of the power versus internal resistance plot. In this area around the matched load, the slope changes gradually which causes the power to not vary significantly with respect to internal resistance (see Figure 7.3). Temperature measurements (such as  $T_s$  and  $T_a$ ) do not vary the model perceptibly when varied within the measurement device capabilities.

In order to use the model, measured values for electrical and temperature values were used to calculate TEG characteristics. Specifically, TEG internal resistance, voltage and temperature were measured.

Electrical measurements of the TEG were taken using a multimeter with a digit display resolution to  $0.1\Omega$ . Realistically, this yields an uncertainty for internal electrical resistances of  $\pm 0.05\Omega$ .

Estimation of the Seebeck coefficient requires consideration of the errors associated with the temperature and voltage measurements. The procedure for measuring the Seebeck coefficient is outlined in Appendix C. Temperature measurements taken using the data acquisition system were sampled at  $\sim 4\text{Hz}$ . The standard deviation was calculated for about 10 minutes worth of data taken for measurements of  $T_L$  and  $T_H$  taken at steady state. The Seebeck coefficient requires  $\Delta T$  in order to calculate. The  $\Delta T$  is a difference  $T_L$  and  $T_H$  so propagation of error for addition and subtraction yields:

$$\sigma_{\Delta T} = \sqrt{\sigma_{T_H}^2 + \sigma_{T_L}^2} \quad (7.1)$$

Where  $\sigma_{T_L}$  and  $\sigma_{T_H}$  are the standard deviations of  $T_L$  and  $T_H$ , respectively.

The standard deviation for voltages was estimated in the same manner as the temperatures. Finding the propagated error for the Seebeck coefficient requires dividing the voltage by the temperature. Using multiplication/division rules for error propagation yields:

$$\frac{\sigma_{\alpha}}{|\alpha|} = \sqrt{\left(\frac{\sigma_{\Delta T}}{|\Delta T|}\right)^2 + \left(\frac{\sigma_{V_{OC}}}{|V_{OC}|}\right)^2} \quad (7.2)$$

$$\sigma_{\alpha} = |\alpha| \sqrt{\left(\frac{\sigma_{\Delta T}}{|\Delta T|}\right)^2 + \left(\frac{\sigma_{V_{OC}}}{|V_{OC}|}\right)^2} \quad (7.3)$$

The data taken was assumed to be a representative sample of all data taken for the installed system on the data acquisition system. The standard deviations of  $T_H$ ,  $T_L$  and  $V$  were found to be 0.85, 0.36 and 0.0765 respectively. Evaluating the standard deviation of the data using Equations 7.1 and 7.3 (with  $\Delta T = 140$  and  $V = 5.4$ ) yields  $\sigma_{\Delta T} = 0.92$  and  $\sigma_{\alpha} = 0.00062$ .

Using these uncertainties (temperatures, voltage, and seebeck coefficient) in the model will vary the results of the model. The power predicted by the model will increase or decrease

depending on whether the parameter is on the upper or lower end of its range. The same trends will occur with the collected data (e.g. actual Seebeck coefficient is higher, the power produced will be higher). Based on model trends, the largest that the power predicted by the model is when the Seebeck coefficient is on the upper end of its uncertainty while the internal electrical resistance is on the lower end its uncertainty. Similarly, the opposite is true with smallest power predicted. This technique is used to find the upper and lower range of the model. These ranges will be shown with a dashed line on all relevant plots.

### 7.1.2 Experimental Uncertainty

In a similar manner to the model uncertainty, the experimental data is subject to uncertainty. For propagation of error for measured data, power is calculated using voltage and current using  $P = VI$ . This error is propagated using:

$$\sigma_P = |P| \sqrt{\left(\frac{\sigma_V}{|V|}\right)^2 + \left(\frac{\sigma_I}{|I|}\right)^2} \quad (7.4)$$

The voltage and current of the device are both measured quantities. This formula is used to propagate the uncertainty in the voltage and current measurements to the power calculations and place error bars on the measured quantities.

## 7.2 Thermoelectric Generator Varieties

For the most optimal solution to be found, a variety of TEGs should be considered. Thermoelectric generators vary widely in cost as well as characteristics, and the optimal variety of TEG may not be immediately apparent. Three TEGs (seen in Figure 7.1) were selected for purposes of this research in order show the process of TEG selection. The properties for the 3 thermoelectric generators can be seen in Table 7.1.

This process could easily be scaled to many more TEGs, provided that their cost, Seebeck coefficients, internal thermal conductivities, and internal electrical resistance are known or can be calculated.

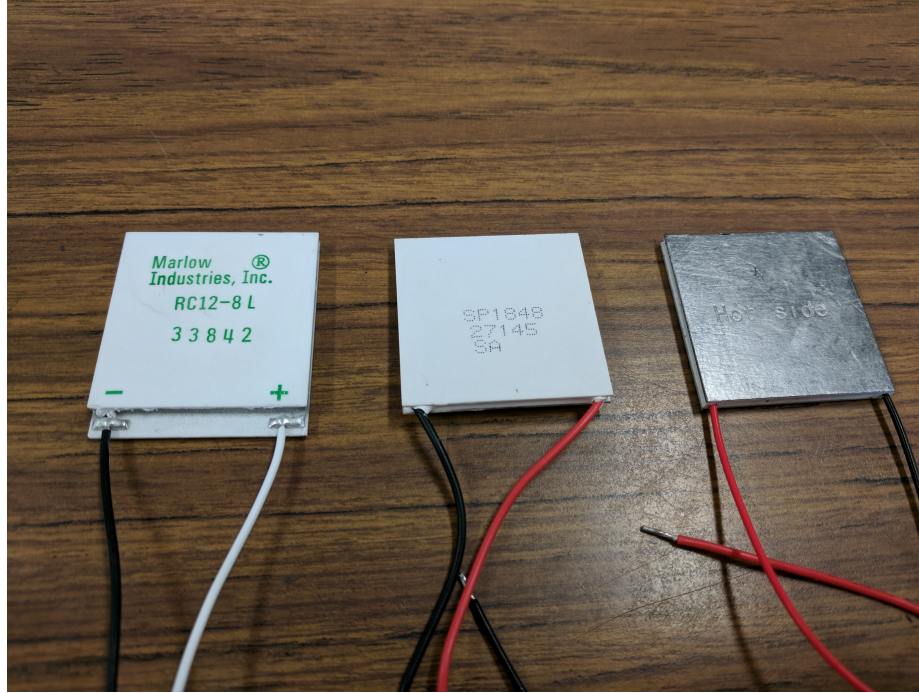


Figure 7.1: TEG varieties considered for power harvester optimization (Left to Right: Marlow RC12-8L, Generic SP1848, Custom Thermoelectric 1261G-731-04CQ)

Table 7.1: TEG varieties with respective properties

	Unit Price for 1	Unit Price for 5	Unit Price for 10	$\alpha_o$ [V/K]	$U_t$ [W/m <sup>2</sup> K]	$R_{int}$ [ $\Omega$ ]
Marlow <i>RC12-8L</i>	\$38.10	\$35.72	\$34.84	0.04	0.633	3.3
Generic <i>SP1848</i>	\$6.99	\$6.99	\$6.99	0.04	0.633	3.3
Custom Thermoelectric <i>1261G-731-04CQ</i>	\$41.00	\$38.00	\$35.00	0.04	0.512	1.7

### 7.3 Bypass Conductance

To estimate the significance of the bypass conductance, the model created in Section 3.3.4 was used. The parameters used in this model are listed in Table 7.2.

The results of this model are listed in Table 7.3. Based on these values, it is reasonable to assume that the bypass resistances are both 0, especially compared to the high conductances of  $U_H$  (see Table 7.4).

Table 7.2: Parameters used for bypass conductance estimates

Parameter	Value	
$A_L^*$	0.032	$m^2$
$A_H$	0.002	$m^2$
$T_H^\ddagger$	510	K
$T_L^\ddagger$	330	K
$\epsilon_H$ [15]	$\sim 0.7$	
$\epsilon_L$ [23]	$< 0.1$	
$L$	0.02 m	
$\nu$ [15]	$15.89 \cdot 10^{-6}$	$m^2/s$
$\alpha$ [15]	$22.5 \cdot 10^{-6}$	$m^2/s$
$Pr$ [15]	0.707	
$k$ [15]	$26.3 \cdot 10^{-3}$	W/m-K
$F_{H \rightarrow L}^\S$	0.3	

\*Based on sides of the heat sink

‡ Used only for conductance estimation (from previous iterations of algorithm)

§ Calculated using Monte Carlo ray tracing program

Table 7.3: Calculated estimates of bypass conductance parameters

	Value (W/m <sup>2</sup> -K)
$U_{bp,rad,1}$	0.0189
$U_{bp,conv,1}$	0.0382
$U_{bp,1}$	0.0572
$U_{bp,rad,2}$	0.0081
$U_{bp,conv,2}$	0.0215
$U_{bp,2}$	0.0296

#### 7.4 Model Validation

This section will outline the results of two tests which were run to validate the model while changing attached electrical resistance and the air speed (cold side conductance). These tests are detailed in Sections 6.2 and 6.3. Measurements were taken in order to determine the parameters required by the model and the uncertainty of the measurements was calculated to determine the limits of the measurement. These can be seen in Table 7.4. The measured parameters for the heat sink are tabulated in Table 7.5. These variables correspond to the generic dimensions shown in Figure 7.2

Table 7.4: Measured parameters from air compressor simulation setup

Parameter	Value		Uncertainty
$T_s$	483	K	$\pm 1$ K
$T_a$	295	K	$\pm 1$ K
$U_H$	100	W/m <sup>2</sup> K	
$U_t$ †	0.6329	W/m <sup>2</sup> K	
$U_{bp,1}$ §	$\sim 0$	W/m <sup>2</sup> K	
$U_{bp,2}$ §	$\sim 0$	W/m <sup>2</sup> K	
Seebeck Coefficient, $\alpha_o$ †	0.04	W/K	$\pm 0.0065$ W/K
$R_{int}$ †	3.3	$\Omega$	$\pm 0.05\Omega$
$R_{load}$	3.3	$\Omega$	$\pm 0.05\Omega$

† Properties for DooCooler thermoelectric generator (SP1848)

§ See Section 7.3

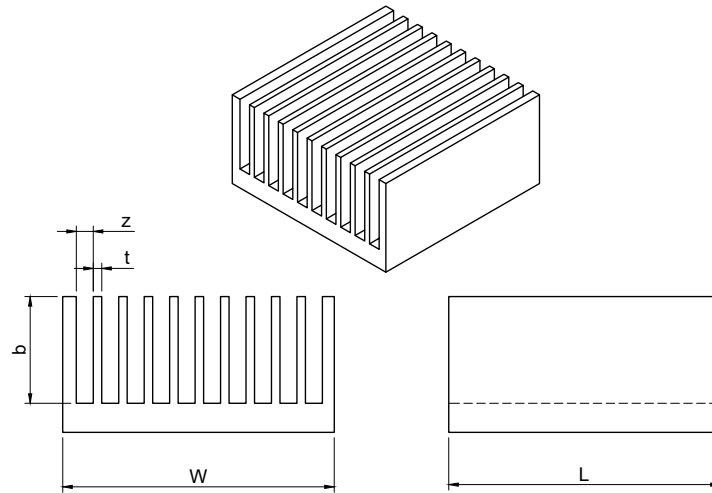


Figure 7.2: Heat sink drawing with generic dimensions

Table 7.5: Parameters for heat sink in air compressor simulation setup

Parameter	Value	
$t$	1.25	mm
$b$	15.72	mm
$L$	40	mm
$z$	2.5	mm
$n$	11	fins

Table 7.6: Air properties used in air compressor simulation setup [5]

Parameter	Value
Thermal Conductivity, $k$	0.0292 W/mK
Kinetic Viscosity, $\nu$	$19.2 \cdot 10^{-6}$ m <sup>2</sup> /s
Prandtl Number, $Pr$	0.707

Table 7.7: Fin material properties used in air compressor simulation [15]

Parameter	Value
Thermal Conductivity, $k$	0.0292 W/mK
Density, $\rho$	2702 kg/m <sup>3</sup>

Using the data represented in Tables 7.4-7.7, the optimization routine (Appendix A.3) was run to calculate the expected power output from the TEG. Two methods were used to evaluate the model: the matched load experiment and the thermal pathways experiment. These were outlined in Sections 6.2 and 6.3. The results of the matched load experiment can be seen in Figure 7.3 while the thermal pathways experiment can be seen in Figure 7.4 and Figure 7.5. In either case, the empirical data measured by the data acquisition system closely follows what the the model predicts.

It should be noted that the case represented in Figure 7.4 is actually a power consuming device for most of the plot range (fan power  $\gtrsim 1.5W$ ) because the back work is greater than the power output. This experiment's goal was not to create a good power harvesting system but to evaluate the effectiveness of the model which will be used to design and optimize a different power harvesting system. This chart illustrates that when varying the fan back work values (and therefore  $U_L$ ), the model solution routine is valid. Figure 7.5 shows the temperatures,  $T_L$  and  $T_H$ , as a function of the fan power for the thermal pathways experiment. While these do not match the model precisely, they follow the trends very well, such that the  $\Delta T$  between the model  $T_L$  and  $T_H$  is virtually identical to that of the measured data.

#### 7.4.1 Air Compressor Installation

To show the usefulness of the model and solution method, a power harvester system was designed and validated for a situation. The problem parameters for this experiment were the same



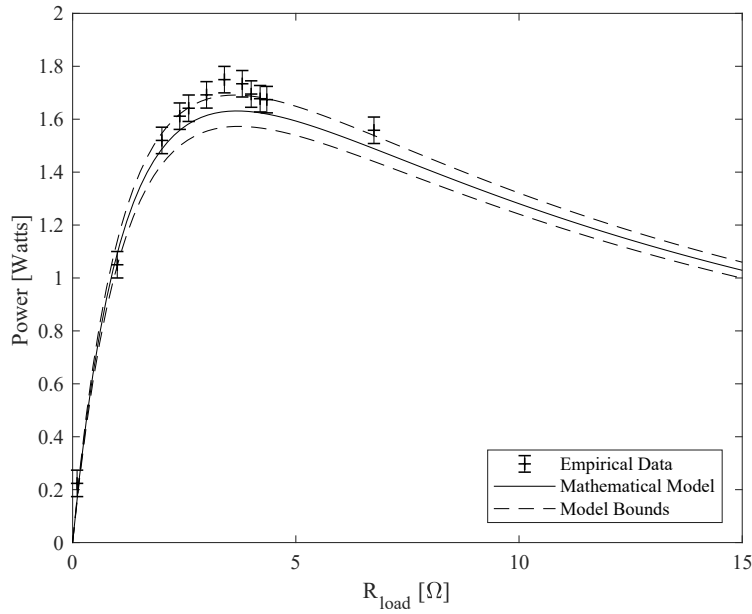


Figure 7.3: Comparison of gross power produced by TEG as predicted by model and measured with empirical data for varying the resistive load with error presented as a standard deviation

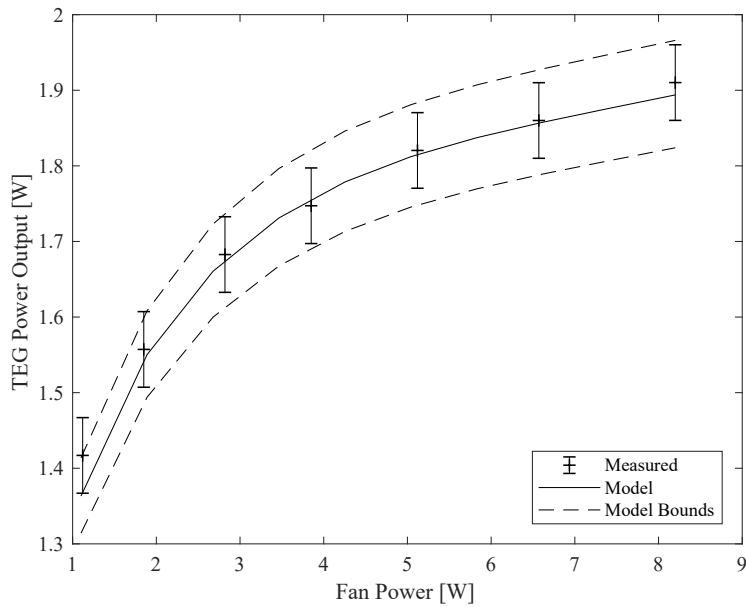


Figure 7.4: Comparison of TEG power produced by TEG as predicted by model and measured for varying fan power (of which  $U_L$  is dependent) with error presented as a standard deviation

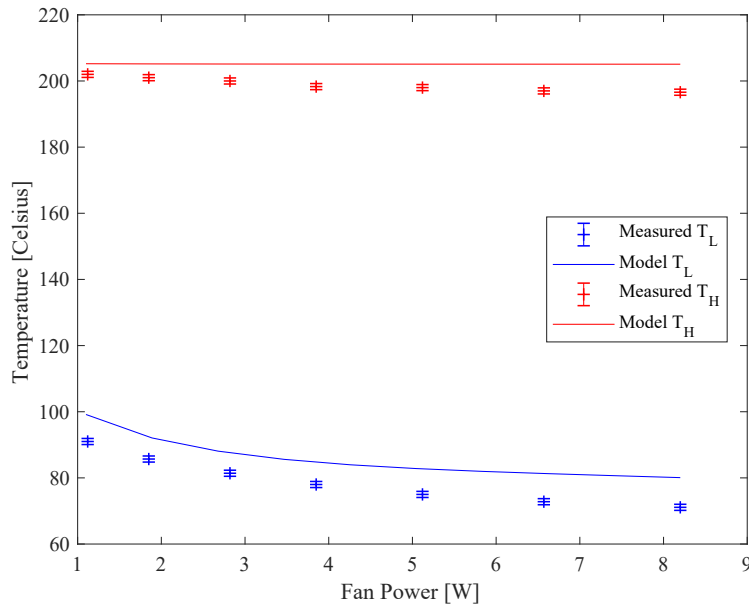


Figure 7.5: Comparison of TEG surface temperatures as predicted by model and measured with empirical data for varying backwork (of which air  $U_L$  is dependent) with error presented as a standard deviation

as were previously used (Tables 7.4-7.7), except  $T_s$  was  $159^\circ\text{C}$ . This was due to reasons previously discussed in Section 6.4. The air compressor was run for about three minutes to allow sufficient time for the temperatures to stabilize, as well as for the air compressor tank to almost completely pressurize. This time was determined because the measured temperature on the surface of the air compressor ceased to change after about two minutes. Figure 7.6 shows a close up of the power harvesting system installed on the air compressor in both standard and infrared images. Figure 7.6(b) shows that the copper diffusers help to maintain a consistent temperature on either side of the TEG as seen by the consistent, red zone on either side of the TEG. The measured temperature parameters were loaded into the TEG power model routine in order to validate the expected power output. Electrical power and current were measured using the data acquisition system. The TEG power model and the measured data are compared in Table 7.8, which shows that model calculations and measurements are within the uncertainty ranges on both the power and current calculations.

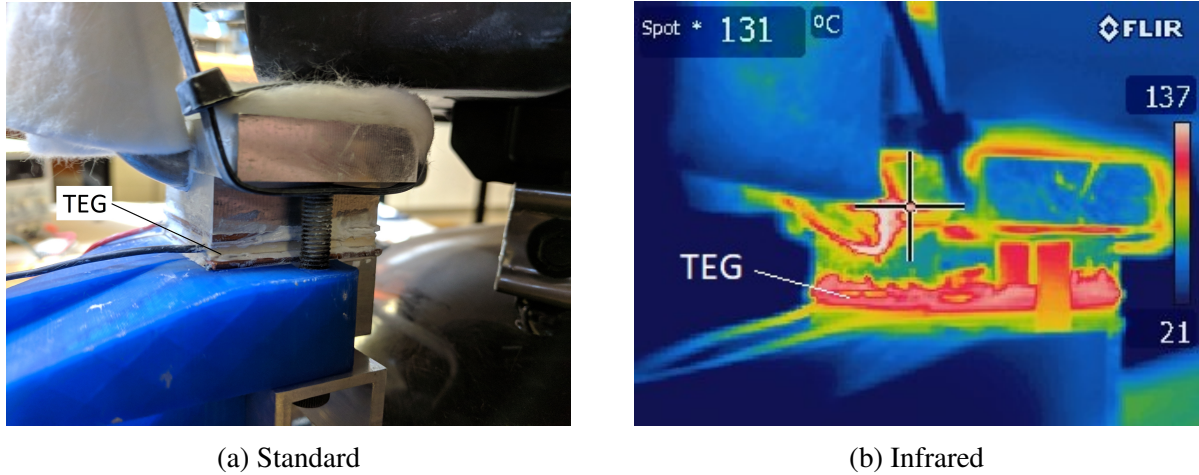


Figure 7.6: Standard and infrared images of air compressor power harvester unit

Table 7.8: TEG power model and measured results for air compressor power harvesting system

	TEG Power	Electric Current
Model	$0.940 \pm 0.0355$ W	$0.534 \pm 0.010$ A
Measurements	$0.930 \pm 0.087$ W	$0.590 \pm 0.02$ A

## 7.5 Air-cooled Case Study

This section will take parameters for the experiment outlined in Section 6.1, enter them into the TEG power model, and compare the measured results to the model's output. Additionally, the results of the TEG power model will be used in the economic model to get a payback period. The parameters required for this case study were the same as those used in Section 7.4. Specifically, Table 7.4 includes measured values for the power harvesting scenario, as well as the respective uncertainties calculated in Section 7.1. The cold side conductance is not included in Table 7.4 because it is to be solved for in the model using an extended surface analysis. Instead, the parameters and back work of the heat sink are included in Table 7.5.

### 7.5.1 Economic Analysis

Because the model was shown to be valid when parameters are varied, it can be used in the economic model optimization routine.

Table 7.9: Economic analysis parameters with intervals in months for air compressor simulation

Parameter	Value
Base Price	\$25
Unit Price†	Varies
Maintenance Cost*	\$25
Maintenance Interval	60 months
Electricity Cost [24]	\$ 0.15 per kW-h
Monthly Discount Rate, $i$ ‡	0.11/12

† Based on TEG variety and quantity

\* Assuming replacement of moving parts after 5 years

‡ Estimated using average return of S&P 500 index fund [25]

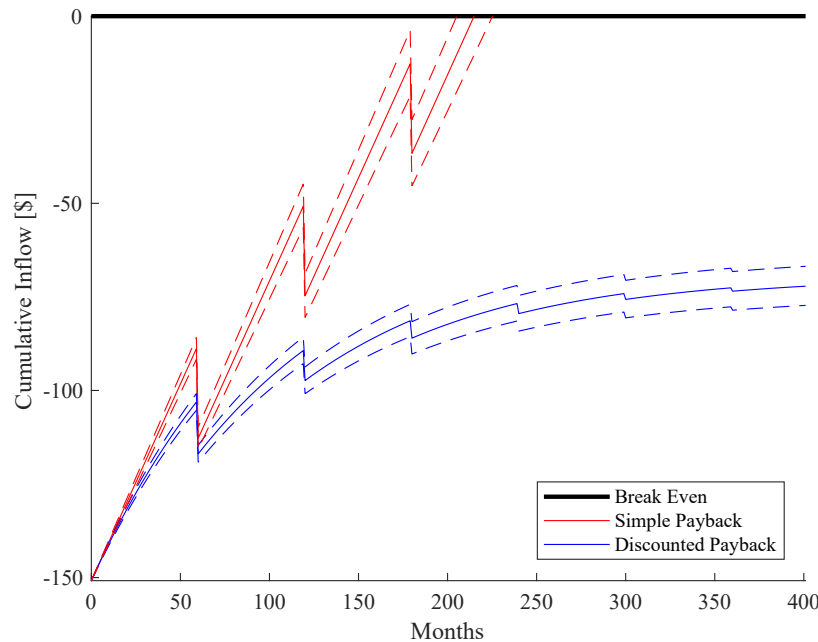


Figure 7.7: Plot of cumulative inflow as a function of months since installation with error presented as one standard deviation for parameters in Tables 7.3-7.7

The data listed in Table 7.9 is entered into the optimization routine. This case assumes a base price of \$25 and maintenance cost of \$25 every 5 years. Additionally, an electricity cost of \$0.15 per kW-hr was assumed based on a nationwide average [24]. These values can vary on a case-by-case basis and can greatly affect the payback period for the device. The optimization routine was allowed to select up to 10 rows, 6 columns, and 13 watts for fan speed.

The iterative results of the payback optimization routine can be seen in Figure 7.7, where the cumulative inflow is plotted as a function of the months since installation. With this arrangement, the simple payback analysis says the system will payoff in almost 215 months, while the more accurate discounted payback analysis shows that the arrangement will never be viable. Also notice in Figure 7.7, the sharp decreases in cumulative inflow whenever a maintenance cost is assessed (every 60 months). For this implementation, the best solution that the genetic algorithm could create was 6 rows by 3 columns of Docoooler TEGs with a fan power of around 2.9 W. Because even the best arrangement created by the optimization routine will never be economically feasible, further exploration will be done into what circumstances will make the power harvesting system viable.

### 7.5.2 Payback Period versus Source Temperature

When faced with a system that will not pay off, it is natural to ask, “at what point will it be viable?” This section will address at what source temperature will the power harvesting become viable. As the difference between source temperature and the ambient temperature increases, the potential for useful power (and therefore power harvesting) increases.

To determine the effect that source temperature has on the payback period, the optimization code was run repeatedly with the same parameters but changing the source temperature. The chart shows results of the optimization routine in the form of the best possible discounted payback period with the given source temperature. These individual results are not necessarily the same configuration (TEG types, quantities, and back work/fan power) as the optimization routine determines the ideal setup each time. A trend that is obvious is, as the difference in temperature increases, the payback period greatly decreases. Table 7.10 shows the  $\Delta T$  (defined as  $T_s - T_a$ ) for the air compressor ( $\Delta T \approx 200K$ ) and its respective payback time of over 170 years. Furthermore, if the temperature difference can be increased by only 50 degrees, the payback period decreases from over a century to just over a decade. An even greater  $\Delta T$  will further decrease the payback period of the power harvesting system.

While the air compressor used in this paper is not capable of creating this temperature difference, commercial air compressors are often used at pressures which would result in higher temperatures. This is corroborated by Figure 1.1, which shows the temperatures during compres-

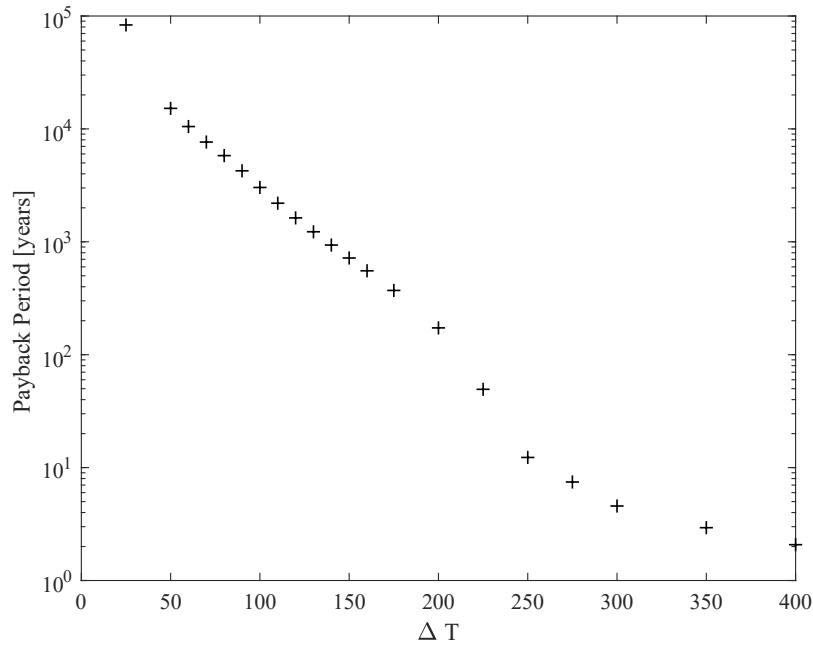


Figure 7.8: Payback period as a function of the source temperature seen by the TEG for parameters in Tables 7.3-7.7

Table 7.10: Comparison of  $\Delta T$  values around and slightly greater than those found on an Air Compressor and their respective payback periods

$\Delta T$	200	225	250	275	300
Payback (Years)	172.8	49.4	12.3	7.5	4.6

sion processes as a function of the pressure. These compressors offer potential temperatures in excess<sup>1</sup> of those seen on a standard consumer grade air compressor.

### 7.5.3 Payback Period versus Electric Cost

In a similar fashion to Section 7.5.2, this section aims to determine at what price per kilowatt-hour of electricity would this technology become viable. It is obvious that cheaper electric costs will make a power harvesting system less feasible due to longer payback periods. As was previously demonstrated in Section 7.5, the system will be unable to be paid off due to the discount

<sup>1</sup>Based on a polytropic process in this  $\Delta T$  can be as much as 50-100 deg C greater (see Figure 1.1)

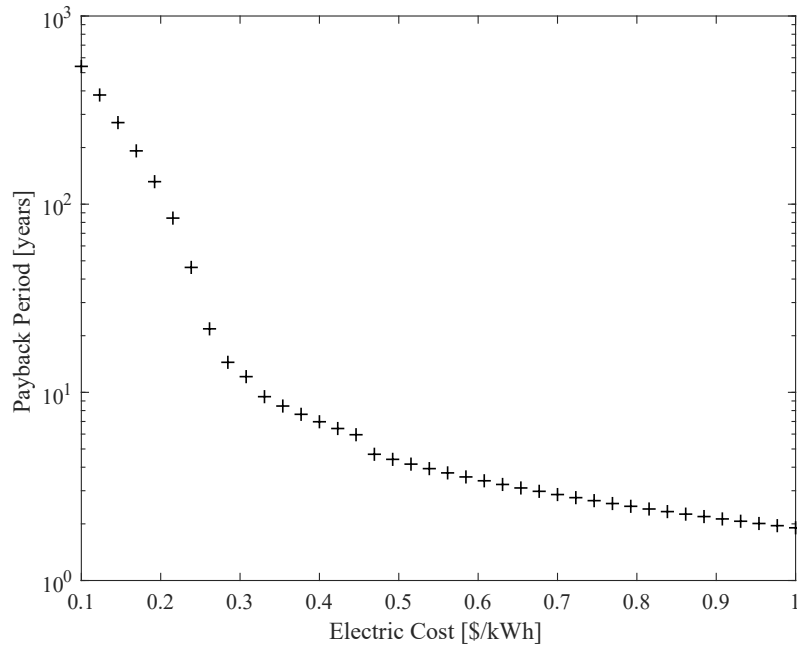


Figure 7.9: Payback period as a function of the cost of electricity per kWh for parameters in Tables 7.3-7.7

Table 7.11: Comparison payback periods as a function of \$/kWh for prices ranging from average electric prices in the United States to slightly more

\$/kWh	0.10	0.15	0.21	0.28	0.33	0.38
Payback (Years)	538.5	270.4	83.71	14.38	9.45	7.62

rate of the analysis if the electric price is too low. Conversely, a larger cost for electricity would make the power harvesters more feasible.

To visualize the effect that the electric price has on payback period, the optimization code was run repeatedly with the same parameters but changing the electric price per kW-hr. This can be seen plotted in Figure 7.9. Table 7.11 numerically illustrates the effect that increasing the price per kilowatt-hour of electricity has on the payback period. The state of Utah has relatively low cost of energy at \$0.10 per kilowatt-hour, making a power harvesting device infeasible. Nationally, the price of electricity is around \$0.09-\$0.16 per kilowatt-hour. This is still infeasible for power harvesting systems. Assuming that a system is feasible if it can pay off in 10 years, these power

harvesting systems do not become feasible in this configuration until electric prices reach around \$0.30 per kilowatt-hour.

While this is not feasible for the mainland United States, electric prices in remote locations may be much higher as electricity from the grid may not be available. In these situations, electricity may be generated on site using fossil fuels. In these cases, the cost of electricity may be higher due to the extra effort required to transport and maintain diesel generators [26]. For similar reasons, some remote countries and territories have high electric costs (e.g. U.S. Virgin Islands at 38 ¢/kWh [27]). Additionally, several countries have high prices due to regulatory fees and taxes (Germany, Denmark, Ireland, Italy, and Cyprus all have electric prices of greater than 30 ¢<sup>2</sup>/kWh [28]). With these increased electric costs, implementing a power harvesting system becomes more feasible because the time to “earn back” the initial investment decreases.

## 7.6 Water Cooled Case Study

In the previous case study, a heat sink with fan was required to remove heat from the TEG, keeping the cool side of the TEG at a cool temperature. Air, while easily accessible, is not as effective at cooling as a liquid. If air were replaced with liquid, the cold side conductance of the power harvesting system could be increased. This section will outline how the model was adapted to fit this modification in the system. The model can be adapted for a variety of situations using this procedure.

### 7.6.1 Model Adaptation

A new model will be developed for the cold side using water as the fluid instead of air. In this case, the heat sink model was replaced with a heat exchanger model. To begin, the heat rate from the cold side of the TEG (or TEGs) is set to be the amount of heat that must be absorbed by the water:

$$q_{L_{TEG}} = \dot{m}c(T_{w,2} - T_{w,1}) \quad (7.5)$$

---

<sup>2</sup>Euro converted to US Dollar (1.328 Euros/USD)



In this equation,  $N_{TEG}$  represents the number of thermoelectric generators in the system. In addition to Equation 7.5, a relationship must be created between the cold side heat rate and the temperature difference between the cold side of the heat sink and the temperature of the water. The water has an initial temperature ( $T_{w,1}$ ) and an unknown final temperature ( $T_{w,2}$ ). The temperature of the water will be assumed to be the average between the inlet and the exit temperatures. This relationship is:

$$\begin{aligned} q_L N_{TEG} &= U_L \Delta T \\ &= U_L \left( T_L - \left[ \frac{T_{w,1} + T_{w,2}}{2} \right] \right) \end{aligned} \quad (7.6)$$

Equations 7.5 and 7.6 are used in place of the Equation 3.1 in the system of equations presented in the mathematical model section (summarized in section 5.1).

These equations to be solved are listed below:

$$\begin{aligned} q_H &= U_H(T_s - T_H) - U_{bp}(T_H - T_a) \\ p &= I^2 R_{load} \\ q_H &= U_t(T_H - T_L) + I\alpha_o T_H - \frac{1}{2} I^2 R_{int} \\ q_L &= U_t(T_H - T_L) + I\alpha_o T_L + \frac{1}{2} I^2 R_{int} \\ p &= I\alpha_o(T_H - T_L) - I^2 R_{int} \\ q_L N_{TEG} &= U_L \left( T_L - \left[ \frac{T_{w,1} + T_{w,2}}{2} \right] \right) \\ q_L N_{TEG} &= \dot{m}c(T_{w,2} - T_{w,1}) \end{aligned}$$

The unknowns in this set of equations are:  $q_H$ ,  $q_L$ ,  $T_H$ ,  $T_L$ ,  $p$ ,  $I$ , and  $T_{w,2}$ . These equations can be solved and used in the same manner as the previous set. The rest of the routine works in the same manner except the means of calculating the cold side conductance. This will be done with a heat exchanger approach.

## Cold Side Conductance

The cold side conductance is generically defined as:

$$U_L = \frac{1}{\frac{1}{h} + \frac{1}{U_{solid}}} \quad (7.7)$$

It is likely that  $U_{solid}$  is similar to that of the hot side conductance as it is conducting through a solid surface. The convection coefficient,  $h$ , is the unknown that must be solved to get  $U_L$ . Even though there are an infinite number of possible configurations, a simple circular pipe was decided to be the configuration for this case study. It was reasoned that a circular pipe was similar to what would be installed in a building and mimicking this approach would minimize the pressure losses seen in the entire system. More simply, if the system is of the same dimensions as the plumbing in a building, then it will likely be unnoticeable as far as pressure losses in the system. Additionally, such a system would be less expensive than complicated, custom solutions. Correlations will be used to get values for interior flow within circular tubing [15]. The Reynolds number,  $Re$ , for internal flow within a circular tube is:

$$Re = \frac{4\dot{m}}{\pi D\mu} \quad (7.8)$$

The critical laminar-turbulent transition point is  $Re_c \approx 2300$ . For Reynold's numbers of less than  $Re_c$ , laminar flow must be considered. For values greater than  $Re_c$ , a correlation for turbulent flow must be considered. For laminar, the Nusselt number correlation is a constant:

$$Nu_D = 4.36 \quad (7.9)$$

while the Nusselt number correlation for turbulent flow is:

$$Nu_D = 0.023Re^{4/5}Pr^{0.4} \quad (7.10)$$

The convection coefficient can easily be acquired by evaluating the definition of the Nusselt number:

$$Nu_D \equiv \frac{hD}{k} \quad (7.11)$$

$$h = \frac{Nu_D k}{D} \quad (7.12)$$

### TEG Scaling

To optimize the system for payback, it may be advantageous to include more than one thermoelectric generator. In a similar manner to what was discussed in Section 5.2.2, the TEGs can be arranged in series or parallel to the water flow. Placing TEGs in series will subject TEGs to a larger water temperature rise throughout (and raise the  $T_L$  seen by the TEGs). Placing the TEGs in parallel will cause them to experience a drop in mass flow rate of the water. Both of these are accounted for in the model and can be changed by the optimization routine. To account for the division in mass flow rate and change in areas, the cross sectional area of the pipe is divided by the number of pipes and the new respective diameter of the pipes is found. Equation 7.13 shows this relationship and was made by rearranging the equation for an area of a circle.

$$\begin{aligned} D_{new} &= \sqrt{\frac{4A_{pipe} \left(\frac{1}{N_{col}}\right)}{\pi}} \\ &= \sqrt{\frac{4 \left(\frac{\pi D_{pipe}^2}{4}\right) \left(\frac{1}{N_{col}}\right)}{\pi}} \end{aligned} \quad (7.13)$$

This new diameter,  $D_{new}$ , is used to calculate the convection coefficient, as this will change with a different diameter pipe.

### Back Work

This case study does not include back work as a necessary parameter. The reasoning behind this decision is the water could be used from the cold water line in a home or business. This water

Table 7.12: Additional parameters for water cool case study

Parameter	Value
Initial Water Temperature, $T_{w,1}$	288 K
Water Mass Flow Rate, $\dot{m}$	0.166 kg/s
Specific Heat of Water, $c$	‡ J/kg-K
Dynamic Viscosity of Water, $\mu_w$	‡ N-s/m <sup>2</sup>
Thermal Conductivity of Water, $k_w$	‡ W/m-K
Prandtl Number, $Pr$	‡
Pipe Diameter, $D$	1 inch

‡ Calculated using interpolation from data [15]

comes from the municipality pressurized so this work is not done at the expense of the end user. Because no pumps are required by the user to pressurize the water, the back work cost to the end user is eliminated which further decreases the payback period of the device.

## 7.6.2 Evaluation

The same parameters were used for this case study where applicable. The new parameters for this case study can be seen in Table 7.12. For the moment, it was assumed that the cost would be the same as the air cooled case study.

Because the pipe size was set to be 1 inch, the number of columns was restricted to be 2 so that resulting pipe size would remain of reasonable diameter. Smaller diameter pipes would add significant friction to the pipe due to the shear caused by the no-slip condition, which is not accounted for in this model. With these parameters entered into the optimization program, an ideal system would be one with 2 columns and 6 rows. This system will payback in 26.5 months or about 2.2 years. A plot of the cumulative inflow can be seen Figure 7.10. This system will create about 42.4 W of electricity.

## 7.7 Discussion

This system pays back significantly faster than the air-cooled model. This is likely due to the fact that this water cooled power harvester system does not require back work as the water comes pre-pressurized from the city or town. Additionally, water has a better heat capacity than air which allows for less of a temperature rise through the system.

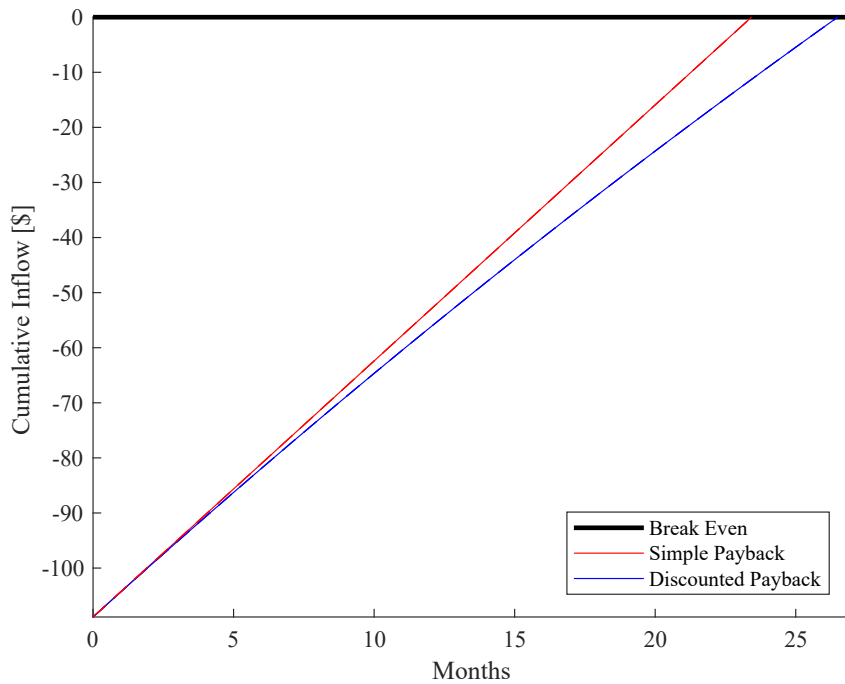


Figure 7.10: Cumulative inflow as a function of months of installation for a water-cooled TEG power harvesting system

Table 7.13: Water cooled case study results with changing base cost

Base Cost	Payback Period	Initial Investment	TEG Array
\$25	2.5 years	\$108.88	6 row x 2 col
\$150	4.65 years	\$289.80	10 row x 2 col
\$500	23.3 years	\$639.80	10 row x 2 col
\$1500	502 years	\$1639.80	10 row x 2 col

Even though the cost of the system was assumed to be the same as the air-cooled system, it is likely to be more than the air-cooled system. This is because modifying the plumbing of a building can be expensive—even if the plumbing is already in the needed location. If the air compressor is installed in the vicinity of the main plumbing inlet, this cost will be significantly lower than if the air compressor must be moved or the water inlet must be rerouted. If either must be relocated, the cost could increase to the point of infeasibility. The effect of increasing the base cost can be seen in Table 7.13.

This chapter illustrates the process through which the model can be adapted for a variety of circumstances. Any desired form factor for heating and cooling the power harvesting system can be adapted in a similar manner as above so that the ideal design for the specific situation can be obtained.

## CHAPTER 8. CONCLUSIONS AND RECOMMENDATIONS

### 8.1 Summary

Air compressors generate a significant amount of waste heat, as much 13 GW [6]. With some single stage air compression systems capable of running at about 1500 kPa, the generated air temperature difference can be as high as 250 degrees Celsius above ambient. Therefore, there is a potential to harvest a significant amount of power from the waste heat transferred from air compression systems to ambient air. Even though this waste heat is common and being generated in abundance, it is (as shown in this research), difficult to recover in a financially viable manner. Even though reducing energy consumption through improving energy efficiency would reduce fossil fuel consumption and dependency, Americans tend to be more financially motivated [29]. Inefficiencies in the TEGs, high unit price for power harvesting components, and inexpensive electricity makes power harvesters difficult to justify financially for the average consumer and small industrial applications. Unless a solution is financially viable, it is likely that the adoption rates will be low. With this in mind, there are some circumstances that would help the feasibility of the thermoelectric generator power harvesters.

The air compressor that was used in this work operates at a relatively low pressure ( $\sim 1000$  kPa). Commercial air compressors are sometimes used in pressures in excess of 3500 kPa. This larger pressure offers greater temperature difference as was explained in this work. In addition to offering a greater  $\Delta T$ , larger air compressors are also oil cooled [4]. The hot oil is cooled in a radiator and fed back into the air compressor to keep the block cool for extended operation. This hot oil offers another location of waste heat that is usually lost. Furthermore, these commercial compressors are sometimes two stage compressors with an intercooler [4]. This offers the benefit of a cooling stage in the middle to cool the hot, compressed air that can be used a potential site for power harvesters.

Because the cooling stages for both the inter-cooling and oil cooling is already removing heat from the system, it is reasonable to assume that a specialized inter-cooling and/or oil cooling stage could be created to harness the power of thermoelectric generator technology in addition to cooling the compressed air and oil. These commercial compressed air systems are often pieced together from individual parts (e.g. tank, compressor, intercooler) as opposed to an all-in-one system like the one used for this research. Because the individual parts are plumbed and wired together, it further increases the serviceability and ease of installation of a power harvesting system. Installation of a power harvester in a commercial setting would have fewer limitations of space than an installation on a consumer grade portable compressor would have, further reducing the cost of a power harvesting system. These systems could be designed from the beginning for optimum benefits as opposed to retrofitting an existing system and making some concessions in the design process.

Additionally, locations where the system is financially feasible was found to be where energy prices are high. Electric prices in the United States are about 10¢/kWh for a vast majority of states [24]. Outlier states pay 15-20¢/kWh and are situated on the east and west coast. Hawaii pays the most out of any state at around 25¢/kWh. In this research, it was found that even at Hawaii's price for electricity, an air cooled power harvesting system is not financially feasible. As was previously discussed, there are other areas or locales where this system could potentially be feasible. Higher electric costs in remote work sites, island nations, as well as countries with high tax rates could cause a thermoelectric generator power harvesting system to be economically feasible.

Ideally, a power harvesting system would be implemented in a location where direct current (DC) power is needed. Because electrical inverters can lose as much as 15% of power in the DC-AC conversion process, keeping the electrical energy as DC power reduces losses within the power harvester [30]. Therefore, if DC power were needed in the vicinity of the power harvesting system to run sensors, small computers, lighting, and other systems, the source of electric losses will be minimized so that more wattage can be retained.

While power harvesting systems for air compressors may not be economically feasible in all cases, there are many factors that could make them feasible. These factors include the  $\Delta T$  which is obtained by the air compressor, the design of the power harvester, and price of electrical



power. This project attempts to outline the process by which someone could design an optimal power harvesting system for an air compressor system.

The following conclusions and recommendations are based on the results of this study.

1. The usage of one and two color pyrometers was explored with respect to the limitations of the technology. Even though a one color pyrometer was used in this work, it was found that two color pyrometers are advantageous over one color pyrometers in terms of accuracy. Additionally, lower wavelengths improve accuracy for both varieties. For a two color pyrometer, a balance must be found between the difference between wavelength as well as the emissivity ratio for the sampled wavelengths. An atmospheric window should be selected so that the atmosphere does not alter the irradiation as seen by the pyrometer. Additionally, a pyrometer measurement should ideally be confirmed with a contact thermometer for certainty in the measurement.
2. A power model was created for the internal and external heat transfer effects on a thermoelectric generator based power harvesting system. When solved, this power model returns the power, current, and heat flow rates, as well as surface temperatures of the TEG. The model was expressed in terms of overall thermoelectric generator properties and also the conductances that are external to the TEG. This model was a non-linear system of equations that could be solved.
3. An experiment was developed under controlled circumstances to show the validity of the created power model. Electric resistive loads on the TEG, as well as the conductance on the cold side of the TEG, were varied to observe how the model's output changed with the dependent variables. The model was able to successfully predict the power output from the TEG power harvester.
4. The external conductances for a variety of scenarios were estimated to test the model. While these conductances are specific to the experiments performed, they can be adapted to a specific situation and substituted into the equations.

5. An economic model was developed so that the payback period of the power harvesting system could be determined. This model may be used to determine whether a power harvesting system should be implemented.
6. The power model was used in an exercise to design a power harvester. A power harvesting unit was designed for an air compressor and the model was used to successfully predict the power output.
7. A method of scaling the number of TEGs in a system independent of the input fan work constant was developed. This method can be used to make systems economically viable by layering TEGs in series and parallel to take advantage of balancing a decrease in air/water mass flow rate with the increase in  $\Delta T$  in the fluid stream through a heat sink.
8. A genetic algorithm was developed to select various combinations of TEG varieties, back work values, and quantities of TEG in the system. The genetic algorithm is ideal for discrete quantities which yield discontinuous functions, but the results are not guaranteed to be repeatable. This type of analysis should be run several times to be sure results are consistent.
9. The power and economic models were used to explore changing the parameters of electric cost and  $\Delta T$  on the economic feasibility of a TEG power harvesting system. Because a power harvesting device is economically infeasible with current electric prices combined with the  $\Delta T$  available from consumer air compressors, these parameters were varied to explore the limits of feasibility. Areas with higher electric costs (such as remote islands, remote job sites, and countries with high taxes) or systems with larger temperature differences such as commercial grade air compressors are found to be better applications for power harvesters.
10. A case study was done on a water-cooled power harvesting system so that water was the working fluid instead of air. The more effective cooling, combined with the absence of back work, yielded an economically feasible design under current electric prices and air compressor temperature availability, provided that the initial costs were low enough.

## 8.2 Limitations

As with all engineering analyses, this work is not without limitations:

1. Only one type of heat sink was considered. Changing dimensions on the heat sink would add custom heat sink costs. Changing entirely different heat sinks would add more discrete variables
2. A fan correlation for a single fan was created. Parameterizing and/or modeling the fan would be difficult. Different fans would need to be either modeled or a different correlation developed.
3. Contact resistance was neglected as it was found to be insignificant. If it were found significant, it would need to be added to the analysis.
4. The transient nature of air compressors was neglected. Air compressors often do not operate constantly all the time [6]. If the powered off time were significantly longer than the powered on time, this would need to be modeled.
5. Air compressor was assumed to be an inexhaustible temperature source.

### 8.3 Recommendations

With these in mind, the scope of this research is not limited to air compressors. From internal combustion engines to computer systems, waste heat can be found in a variety of everyday processes. The process outlined in this work can be applied anywhere there is waste heat:

1. Survey locations for power harvesting systems
2. Design a basic heat transfer solution (air-cooled, water-cooled), determining the conductances for the situation
3. Simultaneously optimize the quantity, type of TEGs and the back work (if applicable) with respect to the payback period

Furthermore, with a large database of heat sink/heat exchanger geometries, fan/pump to back work relationships, and TEGs, step 2 can be further automated so that much of the design work is selected by the genetic algorithm optimization routine. Of these parameters, a database of heat sink and heat exchanger geometries can be easily be obtained with some calipers. The

thermoelectric generator specifications can be obtained from the data sheets and/or the simple experiment outlined in Appendix C. Robust fan/pump back work relationships are very difficult to obtain (aside from correlations) as there are many factors that must be considered such as friction and internal fan geometry. With a proper catalog of these values, many different parameters can be varied and a truly optimum power harvester can be designed.

With more exploration into power harvesting systems, energy conversion processes can become more efficient by implementing power harvesting systems. Using the measured temperature data, an economically viable power harvesting system can be developed to turn this otherwise unused waste heat into usable energy. Turning waste heat into useful electrical energy will help create a more efficient process by wasting less input energy. This, in part, fulfills the National Academy of Engineering's challenge to create new sources of power by creating power from waste heat. While this will not completely eliminate the world's dependence on fossil fuels, it can help in part and keep the world moving toward a cleaner and more sustainable future.

## REFERENCES

- [1] U.S. Energy Information Administration, 2014, “International Energy Statistics.”, from <http://www.eia.gov/beta/international/data/browser/>. 1
- [2] National Academy of Engineering, 2008. *Grand Challenges for Engineering*. Washington, DC. 1
- [3] Humphreys, P., 2012, “Compressed Air - The Fourth Utility.”, from <http://www.thecompressedairblog.com/compressed-air-fourth-utility/>. 1, 3
- [4] U.S. Department of Energy, 2003. “Improving Compressed Air System Performance”. *Compressed Air Challenge*, pp. 3–69. 1, 3, 95
- [5] Cengel, Y., and Boles, M., 2010. *Thermodynamics: An Engineering Approach*, 7th ed. McGraw Hill. 2, 3, 5, 80
- [6] Cerci, Y., Cengel, Y. A., and Turner, R. H., 1995. “Reducing the Cost of Compressed Air in Industrial Facilities”. *Thermodynamics and the design, analysis, and the improvement of energy systems*, **35**, pp. 175–186. 3, 5, 95, 99
- [7] Talbott, E. M., 1993. *Compressed Air Systems: A Guidebook on Energy and Cost Savings*, 2nd ed. Fairmont Press, Inc., Lilburn, GA. 3
- [8] Fluid Power Journal, 2014, “Your Air Tool is Inefficient - Here’s Why.”, from <http://fluidpowerjournal.com/2014/04/air-tool-is-inefficient/>. 5
- [9] Rowe, D., 1995. *CRC Handbook of Thermoelectrics*. CRC Press. 6, 34, 68
- [10] Lee, H., 2010. *Thermal Design*. John Wiley & Sons, Inc. 6, 7, 27, 32, 34, 68, 137
- [11] Moore, T. J., Jones, M. R., Tree, D. R., Daniel Maynes, R., and Baxter, L. L., 2011. “An experimental method for making spectral emittance and surface temperature measurements of opaque surfaces”. *Journal of Quantitative Spectroscopy and Radiative Transfer*, **112**(7), pp. 1191–1196. 11
- [12] Moore, T. J., Cundick, D. P., Jones, M. R., Tree, D. R., Maynes, R. D., and Baxter, L. L., 2011. “In situ measurements of the spectral emittance of coal ash deposits”. *Journal of Quantitative Spectroscopy and Radiative Transfer*, **112**(12), pp. 1978–1986. 11
- [13] Cundick, D., Maynes, D., Moore, T., Tree, D. R., Jones, M. R., and Baxter, L. L., 2012. “In Situ Characterization of Ash Thermal Conductivity for Three Coal Types Formed Under Oxidizing and Reducing Conditions in a Laboratory Furnace”. *Journal of Thermal Science and Engineering Applications*, **4**(4), p. 041002. 11

- [14] Modest, M. F., 2013. *Radiative Heat Transfer*, 3rd ed. Academic Press. 12, 19, 21, 140
- [15] Bergman, T. L., Lavine, A. S., Incropera, F. P., and Dewitt, D. P., 2011. *Fundamentals of Heat and Mass Transfer*. John Wiley & Sons, Inc. 13, 34, 37, 38, 40, 42, 68, 78, 80, 90, 92, 133, 137
- [16] Howell, J. R., Menguc, M. P., and Siegel, R., 2011. *Thermal Radiation Heat Transfer*, 5th ed. CRC Press. 21, 61
- [17] Cepheiden, from [https://commons.wikimedia.org/wiki/File:Atmospheric\\_window\\_EN.svg](https://commons.wikimedia.org/wiki/File:Atmospheric_window_EN.svg). 22
- [18] Taylor, S. H., 2011. “Analytical Modeling and Optimization of a Thermoelectric Heat Conversion System Operating Between Fluid Streams”. Master’s thesis, Brigham Young University. 34
- [19] Kim, D., Kim, S. J., and Ortega, A., 2004. “Compact Modeling of Fluid Flow and Heat Transfer in Pin Fin Heat Sinks”. *Journal of Electronic Packaging*, **126**(3), pp. 342–350. 36
- [20] Wirtz, R. A., Sohal, R., and Wang, H., 1997. “Thermal Performance of Pin-Fin Fan-Sink Assemblies”. *Journal of Electronic Packaging*, **119**(1), pp. 26–31. 36
- [21] Inc., F. S., 2017, “FLIR E50 Datasheet.”, from [http://www.flir.com/uploadedFiles/Thermography\\_USA/Products/Product\\_Literature/flir-e-series-datasheet.pdf](http://www.flir.com/uploadedFiles/Thermography_USA/Products/Product_Literature/flir-e-series-datasheet.pdf). 60
- [22] Aspen Aerogel, 2017, “Spaceloft European Datasheet.”, from [http://www.aerogel.com/\\_resources/common/userfiles/file/Data%20Sheets/Spaceloft-European-Datasheet-EN.pdf](http://www.aerogel.com/_resources/common/userfiles/file/Data%20Sheets/Spaceloft-European-Datasheet-EN.pdf). 71
- [23] Omega, 2017, “Table of Total Emissivity.”, from <https://www.omega.com/temperature/Z/pdf/z088-089.pdf>. 78
- [24] U.S. Energy Information Administration, 2016, “Electricity Data Browser.”, from <http://www.eia.gov/electricity/monthly/>. 84, 96
- [25] The Vanguard Group, Inc., “Vanguard 500 Index Fund Investor Shares (VFINX).”, from <https://personal.vanguard.com/us/funds/snapshot?FundIntExt=INT&FundId=0540>. 84
- [26] IT Power, 2013. Data Collection of Diesel Generators in South Australia. Tech. Rep. September. 88
- [27] US Virgin Islands Water and Power Authority, 2017, “Electric Rates Infographic.”, from [http://www.viwapa.vi/Libraries/PDFs/Electric\\_Rates\\_Infographic.sflb.ashx](http://www.viwapa.vi/Libraries/PDFs/Electric_Rates_Infographic.sflb.ashx). 88
- [28] Energy Information Administration, 2014, “European residential electricity prices increasing faster than prices in United States.”, from <https://www.eia.gov/todayinenergy/detail.php?id=18851>. 88

- [29] Penrod, E., 2015. “Envision Utah Survey: Utahns prefer green energy–until it gets expensive”. 95
- [30] Loba, T. H., Wood, D. H., and Nowicki, E. P., 2015. “Improving Inverter Efficiency at Low Power Using a Reduced Switching Frequency”. In IEEE 28th Canadian Conference on Electrical and Computer Engineering. 96
- [31] Hahn, D. W., and Özişik, M. N., 2012. *Heat Conduction*, 3rd ed. John Wiley & Sons, Inc. 137

## APPENDIX A. OPTIMIZATION ROUTINE CODE

Enclosed in this section is the code used for the power harvester design and optimization. This code was written in MATLAB 2015b and requires the Global Optimization Toolbox in order to use the genetic algorithm function, *ga()*. The functions are listed in roughly the order of usage.

### A.1 Parameters File Code

This function (Code A.1) was called in the beginning of the scripts to create a MATLAB structure array that contains all variables necessary for the calculations. These parameters include external parameters such as temperatures, conductances, TEG characteristics, heat sink dimensions, material properties. Additionally, economic variables are included. Diagnostic and program parameters are also included so that common settings are in one place. This parameter structure could then be passed from to each routine to communicate problem data and centralize parameter storage.

```
1 % Parameters Function for MATLAB R2015b
2 % Creates and returns param struct
3 % Use to edit parameters for analysis
4 % (C) 2017 Zachary Sadler
5
6
7
8 function [param] = Parameters( )
9
10 % Overall System Parameters
11
12     param.Ts = 210+273;      % Source Temperature (K)
13     param.Ta = 22+273;      % Ambient Temperature (K)
14     param.Uh = 100;          % Hot Side Conductance (W/m^2 K)
15     param.Ubp1 = 0.04;      % Bypass Conductance (W/m^2 K)
16     param.Ubp2 = 0.04;      % Bypass Conductance (W/m^2 K)
```



```

param.R_load = 3.3;    % TEG Electrical Load (ohm)
15 param.SolveFor = 'actual'; % Can choose 'actual', 'upper' or 'lower'
param.DimReturnFrac = 0.8; % Rate at which the TEG decays when in series
17 param.TEGScalingType = 'exponential'; % Choose 'exponential' or 'linear'

19 % TEG Parameters
param.TEGchoices = 3;

21 % Marlow
    param.TEG.Name{1} = 'Marlow';
23    param.TEG.Ut(1) = 1/1.58;    % TEG Internal Conductance (W/m^2 K)
    param.TEG.alpha(1) = 0.04;
25    param.TEG.alphaU(2) = 0.0005;
    param.TEG.R_int(1) = 3.3;
27    param.TEG.R_intU(2) = 0.05;
    param.TEG.Price(1, :) =
[38.1,38.1,38.1,38.1,35.72,35.72,35.72,35.72,35.72,34.85];

29 % Docooler
    param.TEG.Name{2} = 'Docooler';
31    param.TEG.Ut(2) = 1/1.58;    % TEG Internal Conductance (W/m^2 K)
    param.TEG.alpha(2) = 0.04;
33    param.TEG.alphaU(2) = 0.0005;
    param.TEG.R_int(2) = 3.3;
35    param.TEG.R_intU(2) = 0.05;
    param.TEG.Price(2, :) = ones(1,10)'*6.99;

37 % Custom Thermoelectric
    param.TEG.Name{3} = 'Custom Thermoelectric';
39    param.TEG.Ut(3) = 0.512;
    param.TEG.alpha(3) = 0.04;
41    param.TEG.alphaU(3) = 0.0005;
    param.TEG.R_int(3) = 1.7;
43    param.TEG.R_intU(3) = 0.05;
    param.TEG.Price(3, :) = [41,41,41,41,38,38,38,38,38,35];

45
47 % Heat Sink Parameters
    param.hs.t = 1.25/1000; % Fin Thickness (m)
    param.hs.b = 15.72/1000;% Fin Length (m)

```

```

49 param.hs.L = 40/1000; % Fin Base Length (m)
param.hs.z = 2.5/1000; % Fin Spacing (m)
51 param.hs.n = 11; % Number of Fins

53 % Fin Material Properties
param.fin.k = 177; % Thermal Conductivity (W/m K)
55 param.fin.rho = 2702; % Density (kg/m^3)

57 % Air Properties
param.air.k = 0.0292; % Thermal Conductivity (W/m K)
59 param.air.nu = 19.2e-6; % Kinetic Viscosity (m^2/s)
param.air.Pr= 0.707; % Prandtl Number

61 % Water Cooling Properties
63 param.water.Ti = 15+273; % Initial Water Temperature (K)
param.water.MassFlowRate = 1/60; % Water Mass Flow Rate (kg/s)
65

% Payback Parameters (intervals in months)
67 param.pb.BasePrice = 25; % Base Price ($)
param.pb.UnitPrice = 0; % Unit Price - TEG price ($)
69 param.pb.MaintCost = 25; % Maintenance Cost ($)
param.pb.MaintInt = 5*12; % Maintenance Interval (months)
71 param.pb.ElecCost = 0.15; % Cost of Electricity ($/kWh)
param.pb.DiscountRate = 0.11/12;% Discount Rate (%)
73 param.bp.MaxIntervals = 400; % Max Intervals (after which payback
analysis terminates)

75 % Configuration Parameters
% Default is Heat Sink when none is selected
77 param.config.UseWaterCool = false;
param.config.PipeDiameter = 0.0254; % meters

79

% Optimization Parameters
81 % setting false uses simple payback in optimization
param.opt.UseDiscountedPayback = true;
83

```

```

% Miscellaneous Diagnostic Parameters
85   param.diag.PrintLaTeX = false;           % Output LaTeX results for report
      param.diag.PrintLaTeXInterval = 1;
87   param.diag.UseBackwork = true;          % Set false to ignore Backwork (for
      diagnostics only)
      param.diag.PlotOptimizationProgress = true; % Set false for speed increase
89   param.diag.PlotPayback = true;          % Plot Payback
      param.diag.SolveBounds = false;        % false will not compute error bars
      (quicker)
91 end

```

Code A.1: Code for param struct creation

## A.2 Economic Model Optimization

### A.2.1 Genetic Algorithm Optimization Code

```

% Main Script for Genetic Algorithm Optimization
2 %   of a Thermoelectric Generator Unit
      %   for MATLAB R2015b
4 %   Requires MATLAB Global Optimization Toolbox
      % (c) 2017 Zachary Sadler
6
clear all;
8 close all;
clc
10
tic
12
% Create the param struct
14 param = Parameters();
      param.SolveFor = 'actual';
16
      %%
18 % Set Lower and Upper Bounds depending on setup
      % [row, col, TEG type, backwork]

```

```

20 if param.config.UseWaterCool == true
    LB = [1,1,1,0];
22    UB = [10,2,param.TEGchoices,0];
else
24    LB = [1,1,1,0];
    UB = [10,6,param.TEGchoices,13];
26 %    UB = [1,1,param.TEGchoices,13];
end
28
% Set Genetic Algorithm options
30 gaopt = gaoptimset('Display','iter',...
    'Generations',25,...
32    'PopulationSize',100,...
    'EliteCount',5,...
34    'StallGenLimit',5,...
    'UseParallel',true);
36
% Turn on or off optimization plot
38 if param.diag.PlotOptimizationProgress
    gaopt.PlotFcns = @gaplotbestf;
40 end
42 % Make PaybackSolver.m accesible for ga()
PaybackSolverGA = @(x) PaybackSolver(x,param);
44 % Run Genetic Optimization
result = ga(PaybackSolverGA,4,[],[],[],[],LB,UB,[],[1 2 3],gaopt);
46 [payback, results] = PaybackSolver(result, param)
48 % Run error bounds if desired
if param.diag.SolveBounds
50    param.SolveFor = 'lower';
    PaybackSolverGA = @(x) PaybackSolver(x,param);
52    result_lower = ga(PaybackSolverGA,4,[],[],[],[],LB,UB,[],[1 2 3],gaopt);
    [payback_lower, results_lower] = PaybackSolver(result_lower,param);
54
    param.SolveFor = 'upper';

```

```

56 PaybackSolverGA = @(x) PaybackSolver(x,param);
    result_upper = ga(PaybackSolverGA,4,[],[],[],[],LB,UB,[],[1 2 3],gaopt);
58 [payback_upper, results_upper] = PaybackSolver(result_upper,param);
end
60
%% Plot the Payback Parameters
62 if param.diag.PlotPayback
    figure;
64 hold on
    if param.diag.SolveBounds
66         plot(results_lower.pb.disc.PeriodIndex,linspace(0,0,length(
results_lower.pb.disc.PeriodIndex)),'linewidth',2,'color','black')
    else
68         plot(results.pb.disc.PeriodIndex,linspace(0,0,length(results.pb.disc.
PeriodIndex)),'linewidth',2,'color','black')
    end
70
    plot(results.pb.simp.PeriodIndex,results.pb.simp.CumulativeInflow,'r');
72 plot(results.pb.disc.PeriodIndex,results.pb.disc.CumulativeInflow,'b');
    if param.diag.SolveBounds
74         plot(results_upper.pb.disc.PeriodIndex,results_upper.pb.disc.
CumulativeInflow,'b--');
            plot(results_lower.pb.disc.PeriodIndex,results_lower.pb.disc.
CumulativeInflow,'b--');
76         plot(results_lower.pb.simp.PeriodIndex,results_lower.pb.simp.
CumulativeInflow,'r--');
            plot(results_upper.pb.simp.PeriodIndex,results_upper.pb.simp.
CumulativeInflow,'r--');
78     end
80     legend_data = {'Break Even','Simple Payback','Discounted Payback'};
    legend(legend_data,'location','southeast');
82 xlabel('Months');
    ylabel('Cumulative Inflow ($)');
84
    if param.diag.SolveBounds

```

```

86         axis ([0,max(results_lower.pb.disc.PeriodIndex),min(results_upper.pb.
disc.CumulativeInflow),0])
else
88         axis ([0,max(results.pb.disc.PeriodIndex),min(results.pb.disc.
CumulativeInflow),0])
end
90 hold off
end
92
%% Print LaTeX Parameters
94 if param.diag.PrintLaTeX

% Simple
96 disp('-----SIMPLE BEGIN-----')
98 disp('Month & Net Inflow & Cumulative Inflow \\')

100 disp(strcat(num2str(results.pb.simp.PeriodIndex(1)), ' & ', ...
num2str(results.pb.simp.Inflow(1)), ' & ', ...
102 num2str(results.pb.simp.CumulativeInflow(1)), '\\'))

104 for i=2:length(results.pb.simp.PeriodIndex)-1
if mod(i-1,param.diag.PrintLaTeXInterval)==0
106 disp(strcat(num2str(results.pb.simp.PeriodIndex(i)), ' & ', ...
num2str(results.pb.simp.Inflow(i)), ' & ', ...
108 num2str(results.pb.simp.CumulativeInflow(i)), '\\'))

end
110 end
len = length(results.pb.simp.PeriodIndex);
112 disp(strcat(num2str(results.pb.simp.PeriodIndex(len)), ' & ', ...
num2str(results.pb.simp.Inflow(len)), ' & ', ...
114 num2str(results.pb.simp.CumulativeInflow(len)), '\\'))
disp('-----SIMPLE END-----')
116
% Discounted
118 disp('-----DISCOUNTED BEGIN-----')

```

```

120 disp('Month & Net Inflow & Discounted Inflow & Cumulative Discounted
Inflow \\')

122 disp(strcat(num2str(results.pb.disc.PeriodIndex(1)), ' & ', ...
num2str(results.pb.disc.Inflow(1)), ' & ', ...
num2str(results.pb.disc.AdjInflow(1)), ' & ', ...
124 num2str(results.pb.disc.CumulativeInflow(1)), '\\'))

126 for i=2:length(results.pb.disc.PeriodIndex)-1
if mod(i-1,param.diag.PrintLaTeXInterval)==0
128 disp(strcat(num2str(results.pb.disc.PeriodIndex(i)), ' & ', ...
num2str(results.pb.disc.Inflow(i)), ' & ', ...
130 num2str(results.pb.disc.AdjInflow(i)), ' & ', ...
num2str(results.pb.disc.CumulativeInflow(i)), '\\'))
132 end
end
134

len = length(results.pb.disc.PeriodIndex);
136 disp(strcat(num2str(results.pb.disc.PeriodIndex(len)), ' & ', ...
num2str(results.pb.disc.Inflow(len)), ' & ', ...
138 num2str(results.pb.disc.AdjInflow(len)), ' & ', ...
num2str(results.pb.disc.CumulativeInflow(len)), '\\'))
140 disp('-----DISCOUNTED END-----')
end
142 %%
disp(['Use ', num2str(result(1)), 'row x', num2str(result(2)), 'col ', num2str(
param.TEG.Name{result(3)}), ' TEGs with fan backwork of ', num2str(result
(4)), ' W' ] )
144 disp(['Payback: ', num2str(payback), ' months or ', num2str(payback/12) ' years
'])
%%
146 RunTime = toc

```

Code A.2: Main function which calls optimization

## A.2.2 Economic Model Function Code

```
% Payback Solver Function for MATLAB R2015b
2 % -Returns either double of simple or discounted analysis and
%   a struct of previous results
4 %   given a param struct and optimization parameters (pbparam)
% (c) 2017 Zachary Sadler
6
function [payback, results] = PaybackSolver(pbparams, param)
8
% Save optimization parameters in more accessible form
10 row = pbparams(1);
12 col = pbparams(2);
14 TEG = pbparams(3);
16 backwork = pbparams(4);
18
% Get air speed from backwork and save in param file
19 param.hs.u_air = FanCorrelation(backwork);
20
% Run solver to get TEG operating conditions
21 [ TEGFuncAns, ~ ] = TEGFuncSolver(param, pbparams);
22
% Store results in results file
23 results.TL = TEGFuncAns(1);
24 results.TH = TEGFuncAns(2);
25 results.QL = TEGFuncAns(3);
26 results.QH = TEGFuncAns(4);
27 results.I = TEGFuncAns(5);
28 results.p_unit = TEGFuncAns(6);
29 results.backwork = backwork;
30 results.NumUnits = row*col;
31
if param.config.UseWaterCool
32     results.T_water1 = param.water.Ti;
33     results.T_water2 = TEGFuncAns(7);
34     param.TEGScalingType = 'linear';
```



```

36     end
38     % Solve for net power
39
40     if strcmp(param.TEGScalingType, 'linear')
41         p = row*col*TEGFuncAns(6);
42     elseif param.config.UseWaterCool
43         p = TEGFuncAns(6)*row*col;
44     else
45         p = 0;
46         for i = 1:row
47             p = p + ((TEGFuncAns(6)/param.DimReturnFrac)*exp(log(param.
DimReturnFrac)*i));
48         end
49         p = p*col;
50     end
51
52     if param.diag.UseBackwork
53         p_net = p-backwork;
54     else
55         p_net = p;
56     end
57
58     results.pnet = p_net;
59
60     % Calculate Net Inflow
61     kWhPerMonth = (p_net*8760/12)/1000;
62     BaseNetInflow = param.pb.ElecCost*kWhPerMonth;
63
64     % Calculate Initial Investment
65     if row*col<10
66         InitialInvestment = row*col*param.TEG.Price(TEG,row*col)+ row*col*
param.pb.UnitPrice + param.pb.BasePrice;
67     else
68         InitialInvestment = row*col*param.TEG.Price(TEG,10)+ row*col*param.pb.
UnitPrice + param.pb.BasePrice;

```

```

68  end
    %% Simple Payback
70  n = 0;

72  results.pb.simp.PeriodIndex(n+1) = n;
    results.pb.simp.Inflow(n+1) = -(InitialInvestment);
74  results.pb.simp.CumulativeInflow(n+1) = -(InitialInvestment);

76  while 1
    n = n + 1;
78
    results.pb.simp.PeriodIndex(n+1) = n;
80  if mod(n,param.pb.MaintInt) ==0 % add maintenance cost if needed
        results.pb.simp.Inflow(n+1) = (BaseNetInflow-param.pb.MaintCost);
82  else
        results.pb.simp.Inflow(n+1) = (BaseNetInflow);
84  end

86  results.pb.simp.CumulativeInflow(n+1) = results.pb.simp.
CumulativeInflow(n)+results.pb.simp.Inflow(n+1);

88  % Break if Cumulative Inflow is positive (paid back)
    if results.pb.simp.CumulativeInflow(n+1) > 0
90      break
    end
92
    % Break if over user specified number of intervals
94  if n >param.bp.MaxIntervals
        break
96  end

98
    end

100  % Discounted Payback
102  n = 0;

```

```

104 results.pb.disc.PeriodIndex(n+1) = n;
results.pb.disc.Inflow(n+1) = -(InitialInvestment);
106 results.pb.disc.CumulativeInflow(n+1) = -(InitialInvestment);
results.pb.disc.AdjInflow(n+1) = -(InitialInvestment);
108
while 1
110     n = n + 1;

112     results.pb.disc.PeriodIndex(n+1) = n;
if mod(n,param.pb.MaintInt) ==0 % add maintenance cost if needed
114         PreadjustedInflow = BaseNetInflow - param.pb.MaintCost;
results.pb.disc.Inflow(n+1) = PreadjustedInflow;
116
AdjustedInflow = PreadjustedInflow/((1+param.pb.DiscountRate)^n);
118     results.pb.disc.AdjInflow(n+1) = AdjustedInflow;
else
120     PreadjustedInflow = BaseNetInflow;
results.pb.disc.Inflow(n+1) = PreadjustedInflow;
122
AdjustedInflow = PreadjustedInflow/((1+param.pb.DiscountRate)^n);
124     results.pb.disc.AdjInflow(n+1) = AdjustedInflow;
end
126
results.pb.disc.CumulativeInflow(n+1) = results.pb.disc.
CumulativeInflow(n)+results.pb.disc.AdjInflow(n+1);
128
% Break if Cumulative Inflow is positive (paid back)
130 if results.pb.disc.CumulativeInflow(n+1) > 0
break
132 end

134 % Break if over user specified number of intervals
if n > param.bp.MaxIntervals
136     break
end

```

```

138
140
142
144
146
148
150
152
154
156
158
160
162
164
end

% Store payback periods to results file
results.payback.simple = results.pb.simp.PeriodIndex(length(results.pb.
simp.PeriodIndex)-1) + ...
    abs(results.pb.simp.CumulativeInflow(length(results.pb.simp.
PeriodIndex)-1))/...
    results.pb.simp.Inflow(length(results.pb.simp.PeriodIndex));

results.payback.discounted = results.pb.disc.PeriodIndex(length(results.pb
.disc.PeriodIndex)-1) + ...
    abs(results.pb.disc.CumulativeInflow(length(results.pb.disc.
PeriodIndex)-1))/...
    results.pb.disc.AdjInflow(length(results.pb.disc.PeriodIndex));

% Select if discounted or simple is used for genetic algorithm
if param.opt.UseDiscountedPayback
    payback = results.payback.discounted;
else
    payback = results.payback.simple;
end

% Apply penalty if net power is less than 0
% or if payback time is negative
if p_net <0 || payback <0
    payback = 1e6;
end

results.price = InitialInvestment;
end

```

Code A.3: Economic model optimization function

### A.3 Thermoelectric Generator Equation Solver

Code A.4 solves for interdependent TEG parameters using MATLAB's *fsolve* equation solver. The function to be solved is Code A.5 which is written in residual format. Additionally, the heat sink function for conductance (see Appendix A.4) is called. Code A.5 is called for heat sink analysis. If the water cooled analysis is stipulated in the parameter file, then the code outlined in Appendix A.5 is used instead.

#### A.3.1 Solver

```
1 % TEGFuncSolver for MATLAB R2015b
2 % -Returns TL,TH,QL,QH,I,p (in an array) when given
3 %   a param struct file and number of units.
4 % -Also returns function values of solver functions for reference
5 % (c) 2017 Zachary Sadler
6
7 function [ answers,fval ] = TEGFuncSolver(param, pbparams)
8
9     row = pbparams(1);
10    col = pbparams(2);
11    TEG = pbparams(3);
12    backwork = pbparams(4);
13
14    param.hs.u_air = FanCorrelation(backwork)/col;
15
16    % Initial starting values for fsolve
17    % "Guesses"
18    TL = 70+273;
19    TH = 203+273;
20    QL = 200;
21    QH = 200;
22    I = 10;
23    p = 10;
24
25    % Store guesses in x array to pass into solver
26    x(1) = TL;
```

```

27 x(2) = TH;
x(3) = QL;
29 x(4) = QH;
x(5) = I;
31 x(6) = p;

33 % Set fsolve options and solve
options = optimoptions('fsolve',...
35         'Algorithm','trust-region-dogleg',...
         'Display','off',...
37         'FinDiffType','central',...
         'TolFun',1e-12,...
39         'TolX',1e-12,...
         'ScaleProblem','Jacobian');

41
43 % Select proper function for Water Cool if needed
% and make accessible to fsolve
if param.config.UseWaterCool
45     % Additional Parameter (initial water temp) for Water Cool
     x(7) = param.water.Ti;
47     TEGFuncfsolve = @(x) TEGFuncWC(x,param, pbparams);
else
49     TEGFuncfsolve = @(x) TEGFunc(x,param, pbparams);
end

51
53 % Run solver on function
[answers,fval] = fsolve(TEGFuncfsolve,x,options);

55 end

```

Code A.4: Solver using Code A.5 and MATLAB's fsolve function

### A.3.2 Function

```
% TEG Func for MATLAB R2015b
2 % -Evaluates TEG functions for fsolve
% -Equations are written in residual format
4 % (C) 2017 Zachary Sadler

6 function [ F ] = TEGFunc( x ,param, pbparams)

8     row = pbparams(1);
     col = pbparams(2);
10    TEG = pbparams(3);
     backwork = pbparams(4);

12
     TL = x(1);
14    TH = x(2);
     QL = x(3);
16    QH = x(4);
     I = x(5);
18    p = x(6);

20    if strcmp(param.SolveFor, 'upper')
         alpha = param.TEG.alpha(TEG)+param.TEG.alphaU(TEG);
22         R_int = param.TEG.R_int(TEG)-param.TEG.R_intU(TEG);
     elseif strcmp(param.SolveFor, 'lower')
24         alpha = param.TEG.alpha(TEG)-param.TEG.alphaU(TEG);
         R_int = param.TEG.R_int(TEG)+param.TEG.R_intU(TEG);
26     else
         alpha = param.TEG.alpha(TEG);
28         R_int = param.TEG.R_int(TEG);
     end

30
% Calculate Conductance Value using HeatSinkFunc
32    Ul = HeatSinkFunc(param.hs.u_air, param);

34 % Evaluate equations
```

```

36 F(1) = param.TEG.Ut(TEG)*(TH-TL)+I*alpha*TH-0.5*(I^2)*R_int-QH;
F(2) = param.TEG.Ut(TEG)*(TH-TL)+I*alpha*TL+0.5*(I^2)*R_int-QL;
38 F(3) = I*alpha*(TH-TL)-(I^2)*R_int-p;
F(4) = U1*(TL-param.Ta)-QL;
F(5) = param.Uh*(param.Ts-TH)-param.Ubp1*(TH-param.Ta)-param.Ubp2*(TH-TL)-
QH;
40 F(6) = (I^2)*param.R_load - p;
42 end

```

Code A.5: 6 equations in function format for MATLAB



## A.4 Heat Sink Solver Code

Code A.6 is used to correlate fan input power (back work) to air speed into the heat sink. This code was called in the heat sink solver (Code A.7) in order to solve for the cold side conductance of the thermoelectric generator.

### A.4.1 Fan Correlation

```
1 % Fan Correlation Function for MATLAB R2015b
2 % -Returns air speed given the input power
3 %   to the fan
4 % -Based on empirical data measured using a power supply
5 %   and an anemometer
6 % (c) 2017 Zachary Sadler
7
8 function [ u_air ] = FanCorrelation( Power )
9     % This was pre calculated from data in another routine to avoid
10    % calculation on each function call
11    poly = [-0.00154515106413047  0.0572323249350450  -0.759649186069322
12           4.95059759575879  1.44729128383527];
13    u_air_before = polyval(poly,Power);
14    u_air = u_air_before*2;
15 end
```

Code A.6: Fan correlation made with empirical data

## A.4.2 Heat Sink Conductance Solver

```
1 % Heat Sink Function for MATLAB R2015b
2 % -Returns Conductance for a heat sink
3 %   given an air speed and parameters struct
4 % (c) 2017 Zachary Sadler
5
6 function [ U1] = HeatSinkFunc(u_air, param)
7     % Reynolds Number
8     Re_L = u_air*param.hs.L/param.air.nu;
9
10    % Convection Coefficient
11    h = (param.air.k/param.hs.L)*0.664*Re_L^(1/2)*param.air.Pr^(1/3);
12
13    % Area Calculations
14    At = param.hs.n*(2*(param.hs.L+param.hs.t)*param.hs.b+param.hs.L*param.hs.
15    z);
16    Af = 2*(param.hs.L+param.hs.t)*param.hs.b;
17
18    bc = param.hs.b+param.hs.t/2;
19    m = (2*h/(param.fin.k*param.hs.t))^(1/2);
20
21    % Fin Efficiencies
22    eta_f = tanh(m*bc)/(m*bc);
23    eta_o = 1 - param.hs.n*(Af/At)*(1-eta_f);
24
25    % Thermal Resistances and Conductances through Heat Sink
26    Rto = 1/(eta_o*h*At);
27    U1 = 1/Rto;
28 end
```

Code A.7: Code used for Heat Sink Conductance Calculation

## A.5 Water Cool Case Study Code

See Appendix A.3 for usage of this code.

```
% TEG FuncWC for MATLAB R2015b
2 % For Water Cooled Scenario
% -Evaluates TEG functions for fsolve
4 % -Equations are written in residual format
% (C) 2017 Zachary Sadler
6
function [ F ] = TEGFuncWC( x ,param, pbparams)
8
    row = pbparams(1);
10    col = pbparams(2);
    TEG = pbparams(3);
12    backwork = pbparams(4);
14
    num = row*col;
16
    TL = x(1);
    TH = x(2);
18    QL = x(3);
    QH = x(4);
20    I = x(5);
    p = x(6);
22    Tw2 = x(7);
% Initial Water Temperature
24    Tw1 = param.water.Ti;
26
    PipeArea = (pi*param.config.PipeDiameter^2)/4;
    intD = sqrt(4*(PipeArea/col)/pi);
28    Tav = (Tw2+Tw1)/2;
    k = WaterProp(Tav, 'k');
30
    Re = 4*param.water.MassFlowRate/(pi*intD*WaterProp(Tav, 'mu'));
32    if Re<2300
        h = 4.36*k/intD;
```

```

34     UL = 1 / ((1/h) + (1/param.Uh));
    else
36     Nu = 0.023*Re^(4/5)*WaterProp(Tav, 'Pr')^0.4;
        h = Nu*k/intD;
38     UL = 1 / ((1/h) + (1/param.Uh));
    end
40
% Evaluate equations
42     F(1) = param.TEG.Ut(TEG)*(TH-TL)+I*param.TEG.alpha(TEG)*TH-0.5*(I^2)*param
        .TEG.R_int(TEG)-QH;
        F(2) = param.TEG.Ut(TEG)*(TH-TL)+I*param.TEG.alpha(TEG)*TL+0.5*(I^2)*param
        .TEG.R_int(TEG)-QL;
44     F(3) = I*param.TEG.alpha(TEG)*(TH-TL)-(I^2)*param.TEG.R_int(TEG)-p;
        F(4) = (param.water.MassFlowRate*WaterProp(Tav, 'cp')/col)*(Tw2-Tw1) - QL*
        row;
46     F(5) = param.Uh*(param.Ts-TH)-param.Ubp*(TH-param.Ta)-QH;
        F(6) = (I^2)*param.R_load - p;
48     F(7) = (TL-Tav)*UL-QL*row;
end

```

Code A.8: Function required for water cool case study

## APPENDIX B. THERMOCOUPLE CALIBRATION PROCEDURE

Before calibration all thermocouples had readings within 0.5°C of the actual temperature. Thermocouples were calibrated using a boiling water procedure.

Atmospheric pressure was measured using Eyring Science Center weather data (<https://marvin.byu.edu/Weather/cgi-bin/textsi>) and confirmed using a barometric pressure sensor on an LG Nexus 5X smartphone. This data was used to find the boiling point temperature for the barometric pressure conditions.

Using the known boiling point temperature, offsets were adjusted to make them more accurate. These offsets were confirmed at room temperature with an alcohol thermometer.

For reference, pressure in Provo, Utah at time of calibration was 864.85 hPa where water boils at 95.87°C .

## APPENDIX C. OVERALL SEEBECK COEFFICIENT MEASUREMENT PROCEDURE

As stated in Section 1.4, the seebeck coefficient can be estimated as a ratio of a voltage differential per temperature differential, or:

$$\alpha = \frac{\Delta V}{\Delta T} \quad (\text{C.1})$$

Even though both the n- and p-type thermocouples each have their own seebeck coefficients, when the entire TEG is considered, the overall seebeck coefficient can be found.

In order to measure the overall Seebeck coefficient,  $\alpha_o$ , the TEG is placed in the experimental setup outlined in Section 6.1. This setup allows for precise temperature measurements on the surfaces of the TEG. Within this setup, the variable resistor and the shunt are disconnected in order to open the circuit. Allowing for an open circuit eliminates current flow through the TEG, removing the effects of the Thomson and Peltier effects. This circuit can be seen in Figure C.1.

Using this setup, the open circuit voltage is measured as the voltage potential across the TEG. Additionally, the temperatures on the hot and cold sides ( $T_H$  and  $T_L$ ) are measured. This temperature difference is used in the Seebeck coefficient. Using these parameters, Equation C.1 for the overall Seebeck coefficient can be further rewritten:

$$\alpha_o = \frac{V_{OC}}{T_H - T_L} \quad (\text{C.2})$$

When the experiment is run, the source temperature is not important because the hot and cold side temperatures are measured. Even though the Seebeck coefficient does not vary significantly with temperature, for precision, the source temperature was chosen to be similar to that of the air compressor. Furthermore, the temperature and voltage measurements are only taken after the system has been allowed to reach thermal and electrical equilibrium. While this may occur after 2-3 minutes, the data was collected after at least 5 minutes in order to be sure.

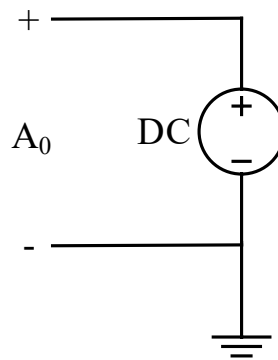


Figure C.1: Wiring diagram for overall seebeck coefficient measurement

## **APPENDIX D. AIR COMPRESSOR EXPERIMENT DESIGN DOCUMENTS**

This section contains the drawings used for fabrication of the air compressor power harvester. Drawings for individual parts are included for parts which must be machined. Because the blower fan duct (item 8 in Figure D.1) was 3D printed from the CAD model, a drawing is not included. The heat sink is a purchased, off-the-shelf component.



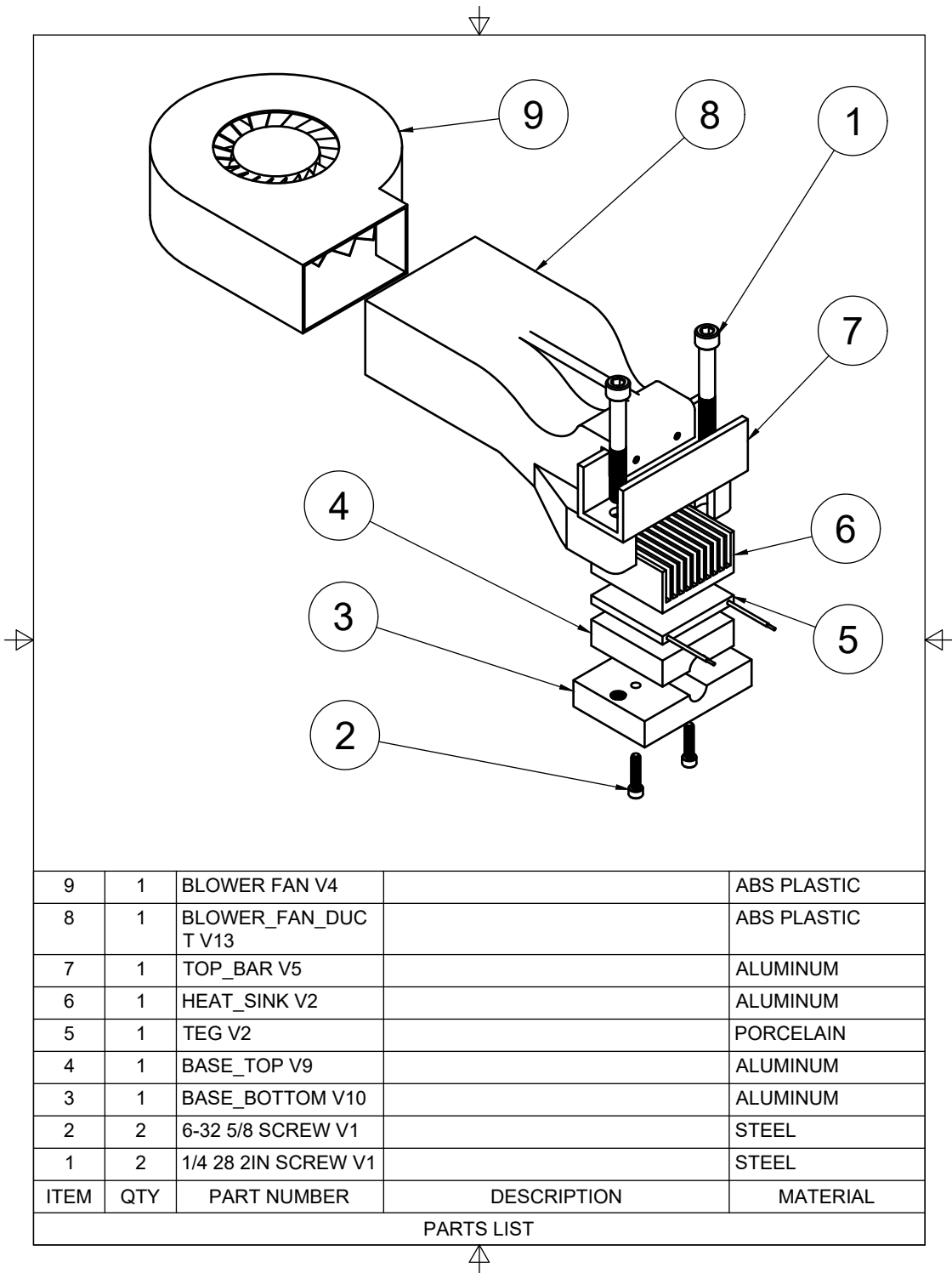


Figure D.1: Air Compressor TEG Installation Drawing: Exploded Assembly

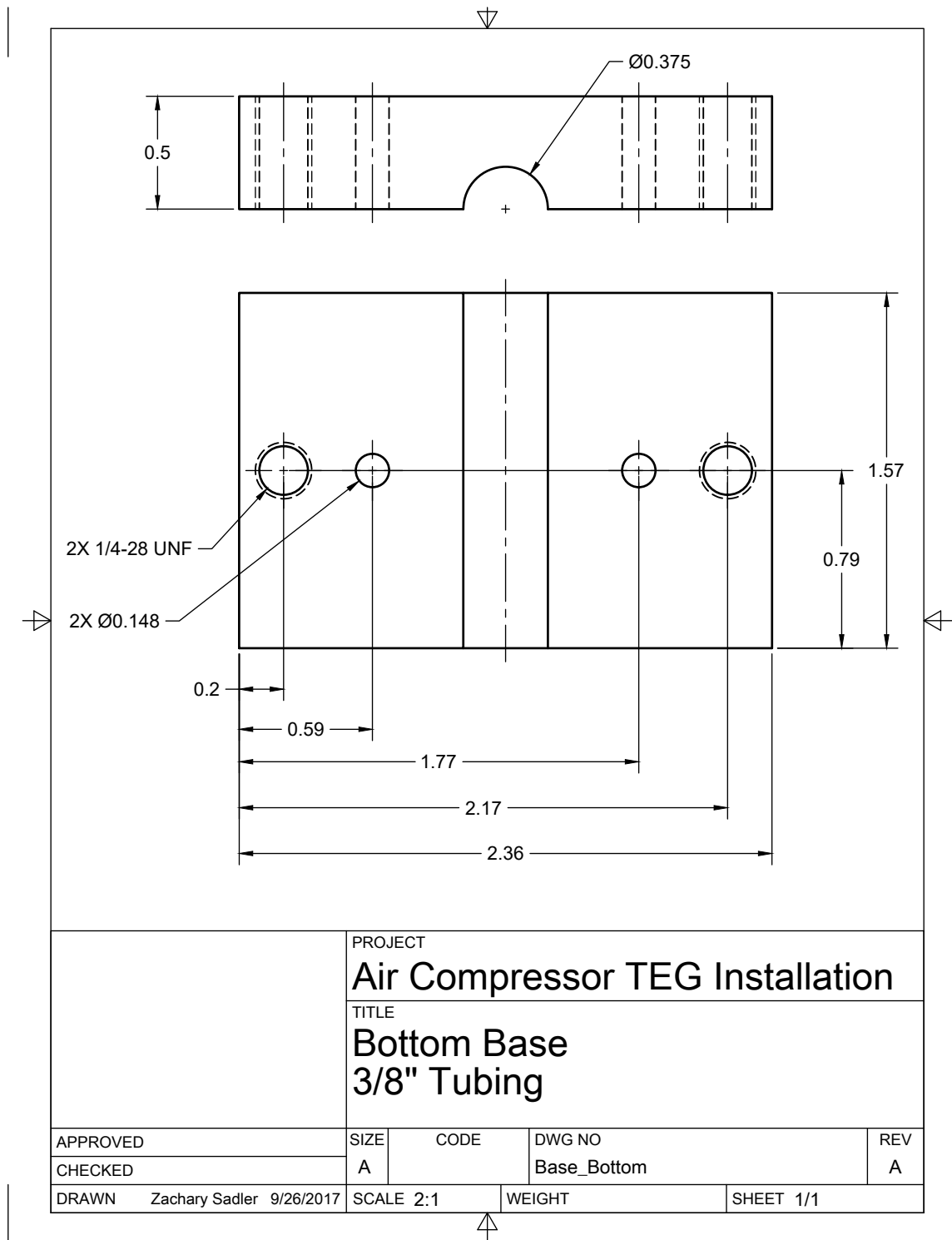


Figure D.2: Air Compressor TEG Installation Drawing: Base Bottom Drawing

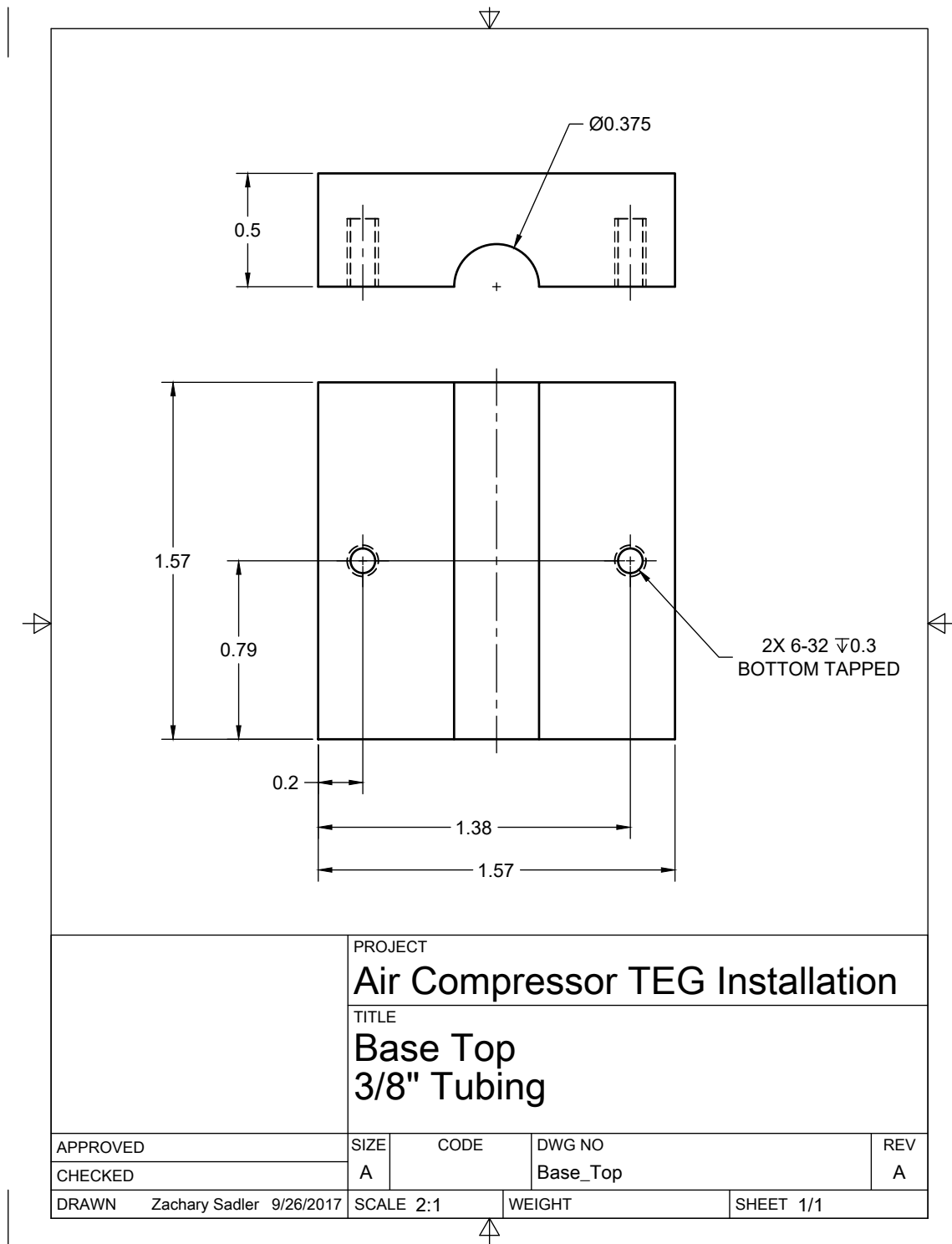


Figure D.3: Air Compressor TEG Installation Drawing: Base Top Drawing

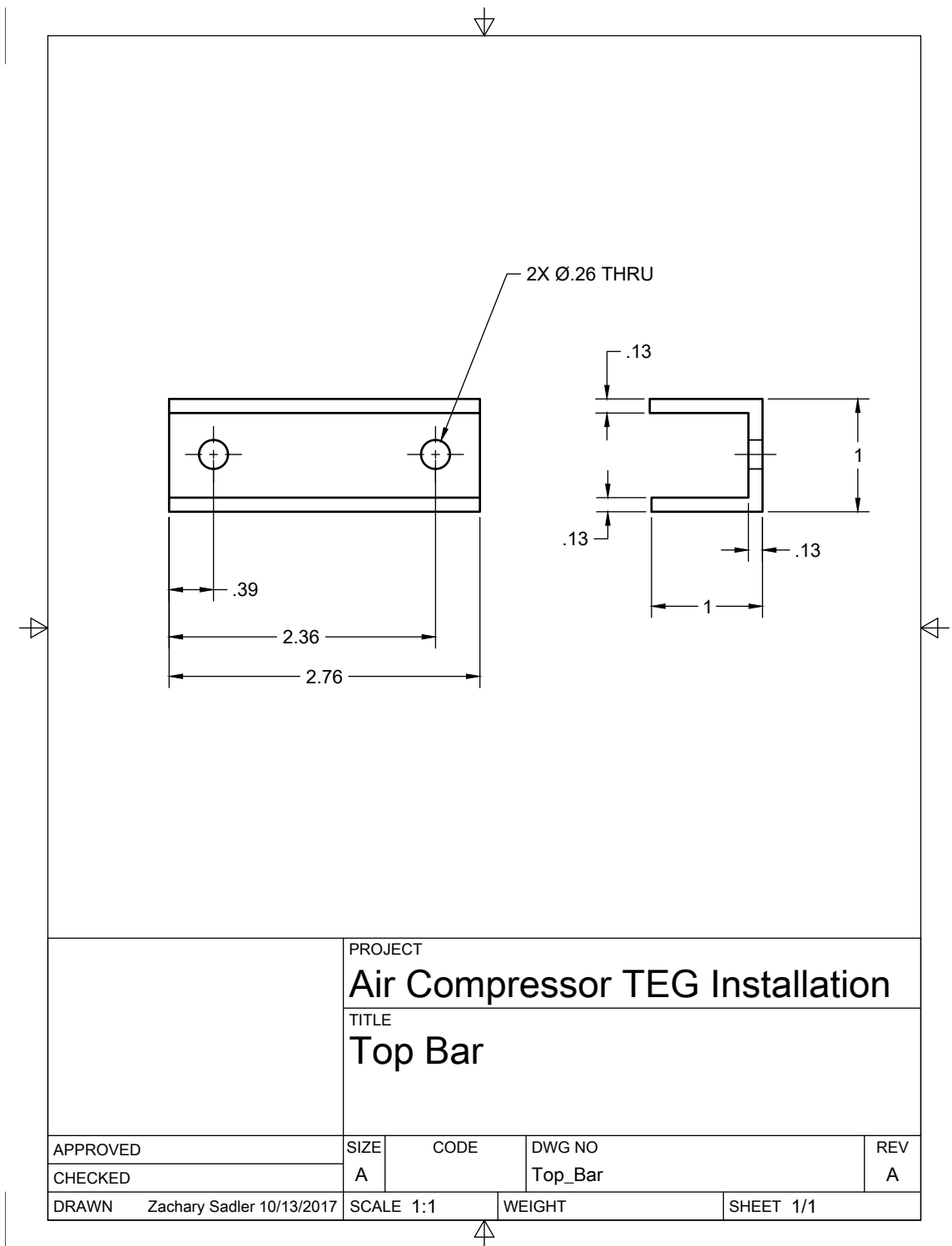


Figure D.4: Air Compressor TEG Installation Drawing: Top Bar Drawing

## APPENDIX E. THERMODYNAMIC PROPERTIES OF WATER

This section lists the values used for interpolation for the water cooled case study (Section 7.6) as well as the code used for interpolation. Data in Table E.1 is from *Fundamentals of Heat and Mass Transfer* [15].

Table E.1: Thermodynamic properties of water

Temp.	Viscosity $\mu \cdot 10^6$	Pr	Thermal Conductivity $k \cdot 10^3$	Specific Heat
<i>K</i>	<i>N · s/m</i>		<i>W/m · K</i>	<i>J/kg · K</i>
280	1422	10.26	582	4198
285	1225	8.81	590	4189
290	1080	7.56	598	4184
295	959	6.62	606	4181
300	855	5.83	613	4179
305	769	5.2	620	4178
310	695	4.62	628	4178
315	631	4.16	634	4179
320	577	3.77	640	4180
325	528	3.42	645	4182
330	489	3.15	650	4184
335	453	2.88	656	4186
340	420	2.66	660	4188
345	389	2.45	664	4191
350	365	2.29	668	4195
355	343	2.14	671	4199
360	324	2.02	674	4203
365	306	1.91	677	4209
370	289	1.8	679	4214

```

1 function [answer] = WaterProp(T,type)
   Temps = linspace(280,370,19);
3   mu = [1422, 1225, 1080, 959, 855, 769, 695, 631, 577, 528, 489, 453, 420,
   389, 365, 343, 324, 306, 289]*10^-6;
   Pr = [10.26, 8.81, 7.56, 6.62, 5.83, 5.20, 4.62, 4.16, 3.77, 3.42, 3.15,
   2.88, 2.66, 2.45, 2.29, 2.14, 2.02, 1.91, 1.80];
5   k = [582, 590, 598, 606, 613, 620, 628, 634, 640, 645, 650, 656, 660, 664,
   668, 671, 674, 677, 679]*10^-3;
   cp = [4.198, 4.189, 4.184, 4.181, 4.179, 4.178, 4.178, 4.179, 4.180,
   4.182, 4.184, 4.186, 4.188, 4.191, 4.195, 4.199, 4.203, 4.209,
   4.214]*1000;
7   if strcmp(type, 'Pr')
       gen = Pr;
9   elseif strcmp(type, 'mu')
       gen = mu;
11  elseif strcmp(type, 'cp')
       gen = cp;
13  else
       gen = k;
15  end
   for i = 1:length(Temps)-1
17     if T<Temps(i)
           answer = gen(1);
19     elseif T<=Temps(i+1) && T>=Temps(i)
           mult = (T-Temps(i))/(Temps(i+1)-Temps(i));
           answer = mult*(gen(i+1)-gen(i))+gen(i);
21     break
23     elseif T>Temps(length(Temps))
           answer = gen(length(Temps));
25     end
   end
27 end

```

Code E.1: Interpolation routine for evaluating viscosity, Pr, thermal conductivity and specific heat for water at various temperatures

## APPENDIX F. VALIDATION OF POWER OUTPUT OF TEGS IN SERIES

To confirm the behavior of series arrangement mentioned in Section 5.2.2, three TEG's were placed on a hot plate with three heat sinks such that the air would blow through the channel and cool each TEG in series. The first TEG received cooler air than the last TEG.

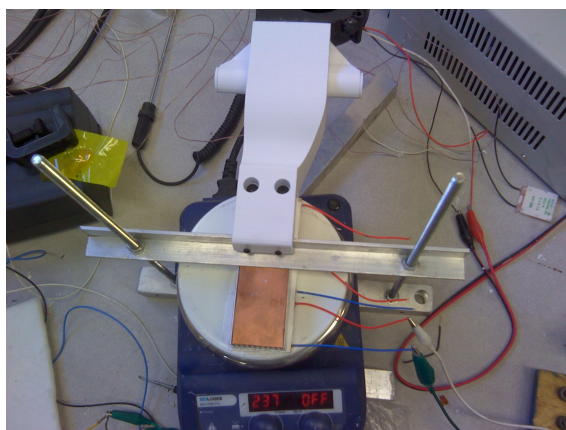
Images of this experiment can be seen in Figure F.1(a). It was found that the hot plate was not isothermal to yield uniform results but the given results were not useless. An infrared image of the hot plate can be seen in Figure F.1(b) which shows a bright "hot spot" in the middle with the edges being cooler.

This yields interesting results with the power output from the TEGs. Of the several cases which were tried (seen in Table F.1), both the first and second TEGs had approximately the same power output. The third TEG almost always had somewhere between 65-75% of the power of the first and second TEG. Because of the difference in hot plate temperatures in the center versus the outside, it is assumed that that the hot plate has similar temperatures underneath the first and the third TEGs. With the power reduction fraction,  $d$ , which was proposed in Section 5.2.2, this amounts to about a 85% drop between TEGs.

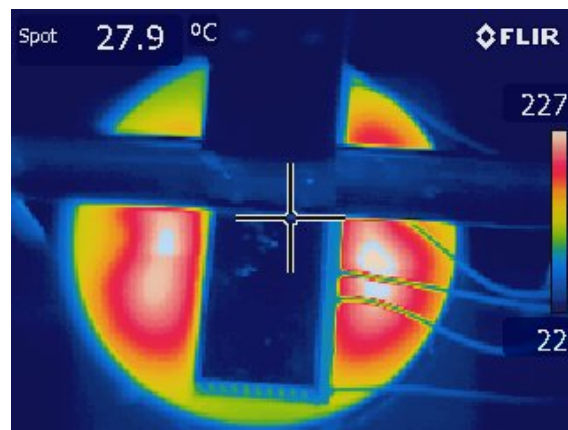
With this data in mind, the author recommends using a power reduction fraction of  $d = 0.8$  in order to be conservative in the analysis.

Table F.1: Data from TEGs in series with respect to heat sink for varying conditions

$T_s$ (K)	$P_{back}$ (W)	$P_1$ (W)	$P_2$ (W)	$P_3$ (W)
200	0.48	0.70	0.72	0.51
240	0.48	1.02	1.00	0.70
280	0.48	1.30	1.25	0.84
240	0.35	0.77	0.70	0.48
280	0.35	1.00	0.89	0.59



(a) Standard



(b) Infrared

Figure F.1: Standard and infrared images of a hot plate to show non-isothermal behavior



## APPENDIX G. HEAT SINK DERIVATION

This analysis is performed below for reference. For further information, the reader is referred to a standard heat transfer text such as *Fundamentals of Heat and Mass Transfer* by Bergman [15], *Thermal Design* by Lee [10], or *Heat Conduction* by Hahn [31].

Considering a single fin to be the system and performing an energy balance on a differential slice of a single fin yields an energy balance between conducted heat into and out of the slice as well as the convected heat transfer:

$$\begin{aligned}q_x - \left(q_x + \frac{dq_x}{dx} dx\right) - dq_{conv} &= 0 \\ \frac{dq_x}{dx} dx - dq_{conv} &= 0\end{aligned}\tag{G.1}$$

where,

$$\begin{aligned}q_x &= -kA \frac{dT}{dx} \\ q_{conv} &= hP dx (T_s - T_a)\end{aligned}$$

Substitution yields:

$$-\frac{d}{dx} \left( -A_c k \frac{dT}{dx} \right) dx - hP dx (T - T_a) = 0\tag{G.2}$$

$$\frac{d^2 T}{dx^2} - \frac{hP}{kA_c} (T - T_a) = 0\tag{G.3}$$

With boundary conditions (constant base temperature and convective tip):

$$BC1 : \quad T(0) = T_b\tag{G.4}$$

$$BC2 : \quad A_c h_o (T(L) - T_a) = -kA_c \frac{dT(L)}{dx}\tag{G.5}$$

Putting the Equation G.3 in the standard form with  $\theta = T - T_a$  yields,

$$\frac{d^2\theta}{dx^2} - m^2\theta = 0 \quad (\text{G.6})$$

where,

$$m = \sqrt{\frac{hP}{kA_c}} \quad (\text{G.7})$$

and boundary conditions are now:

$$BC1: \quad \theta(0) = \theta_b \quad (\text{G.8})$$

$$BC2: \quad h_o\theta(L) = -k\frac{d\theta(L)}{dx} \quad (\text{G.9})$$

The general solution to this differential equation (Equation G.6) is:

$$\theta(x) = C_1e^{mx} + C_2e^{-mx} \quad (\text{G.10})$$

or

$$\theta(x) = C_1 \sinh(mx) + C_2 \cosh(mx) \quad (\text{G.11})$$

Applying parameters for a rectangular fin with constant thickness to Equation G.7 and assuming that thickness of the fin ( $t$ ) is much smaller than the length ( $L$ ) yields:

$$\begin{aligned} m &= \sqrt{\frac{h(2L + 2t)}{kLt}} \\ &= \sqrt{\frac{2h}{kt} \left(1 + \frac{t}{L}\right)} \\ m &\approx \sqrt{\frac{2h}{kt}} \end{aligned} \quad (\text{G.12})$$

Using the boundary condition yields the solution:

$$\begin{aligned}\frac{\theta}{\theta_b} &= \frac{\cosh(m(L-x)) + \frac{h}{mk} \sinh(m(L-x))}{\cosh(mL) + \frac{h}{mk} \sinh(mL)} \\ \theta &= \theta_b \frac{\cosh(m(L-x)) + \frac{h}{mk} \sinh(m(L-x))}{\cosh(mL) + \frac{h}{mk} \sinh(mL)}\end{aligned}\quad (\text{G.13})$$

The heat leaving the fin is determined by the heat conduction through the base of the fin:

$$\begin{aligned}q_f &= -kA_c \frac{dT(0)}{dx} \\ &= -kA_c \frac{d\theta(0)}{dx}\end{aligned}\quad (\text{G.14})$$

Taking the derivative of Equation G.13, evaluating at  $x = 0$ , and substituting Equation G.12 yields,

$$\begin{aligned}q_f &= kA_c m \theta_b \frac{\sinh(mb) + \frac{h_o}{mk} \cosh(mb)}{\cosh(mb) + \frac{h_o}{mk} \sinh(mb)} \\ &= \sqrt{hPkA_c} \theta_b \frac{\sinh(mb) + \frac{h_o}{mk} \cosh(mb)}{\cosh(mb) + \frac{h_o}{mk} \sinh(mb)}\end{aligned}\quad (\text{G.15})$$

Assuming an adiabatic tip condition means that  $h_o = 0$  and turns Equation G.15 to:

$$q_f = \theta_b \sqrt{hPkA_c} \tanh(mb)\quad (\text{G.16})$$

## APPENDIX H. VIEW FACTOR PROGRAM PSEUDOCODE

This chapter will outline the pseudocode approach for the routine created by the author to determine shape/view factors of 3 dimensional objects relative to each other. The program was made using C++, OpenGL and the QT Framework. It accepts two STL files to define 3D shapes and allows for spatial manipulation of the shapes relative to each other. The author referenced Modest's book *Radiative Heat Transfer* [14] for several formulae relating to Monte Carlo ray tracing simulations for view factor calculation.

Below is a simple pseudocode of the program process for the Monte Carlo ray tracing simulation. Some irrelevant detail pertaining to user interface, graphics and file storage and loading is left out due to simplicity.

1. Repeat n times
  - (a) Obtain triangle data from STL files (emitter and targets)
  - (b) Get random triangle from the emitter (triangles are weighted according to relative size so that large triangles are more likely to be selected)
  - (c) Get random point on the triangle surface
    - i. Get triangle's vertices (3 vectors:  $A$ ,  $B$ , and  $C$ )
    - ii. Get 3 random numbers ( $r_a$ ,  $r_b$ , &  $r_c$ ) from 0 to 1
    - iii. Random Point (P) (a vector):  $P = \frac{r_a A + r_b B + r_c C}{r_a + r_b + r_c}$
  - (d) Get random azimuthal and polar angle for ray direction
    - i.  $azi = 2\pi * rand(0, 1)$
    - ii.  $pol = \arcsin(\sqrt{rand(0, 1)})$
  - (e) Cycle through triangles on the emitter until a collision is found or all triangles are exhausted (search for a self collision) and store collision distances

- (f) Cycle through triangles on the target until a collision is found or all triangles are exhausted (searching for a target collision) and store collision distances
  - (g) Check vector lengths for all collisions as the shortest will be the first collision
  - (h) Count collisions as a hit for either the target or the emitter
  - (i) If no collision occurs, count as a miss
2. Divide total collisions on emitter by  $n$  to get emitter to emitter view factor
  3. Divide total collisions on target by  $n$  to get emitter to target view factor
  4. Divide total misses by  $n$  to get emitter to surrounding view factor